

國立臺灣大學工學院材料科學與工程學研究所

碩士論文

Department of Materials Science and Engineering

College of Engineering

National Taiwan University

Master Thesis

奈米碳材於高分子太陽能電池上之應用

Nanocarbon Based Polymer Solar Cells



杜昆樺

Kun-Hua Tu

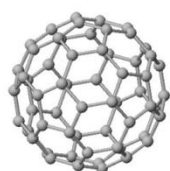
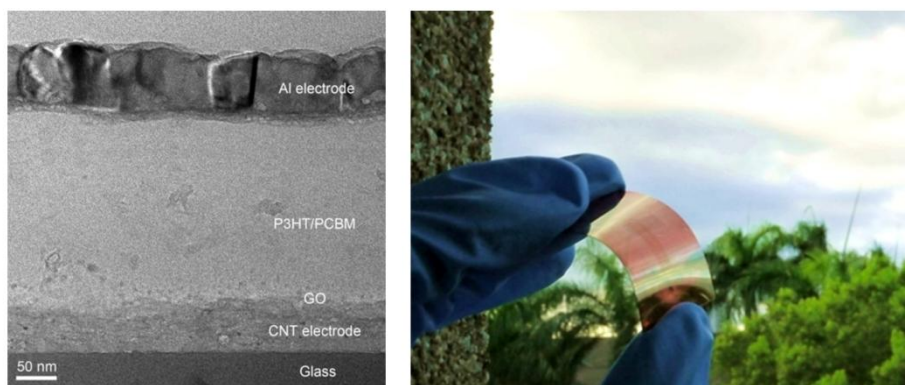
指導教授：陳俊維 博士

Advisor: Chun-Wei Chen, Ph.D.

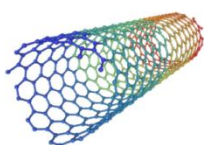
中華民國 100 年 6 月

June, 2011

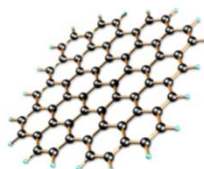
## *Nanocarbon based polymer solar cells*



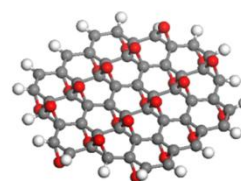
Fullerene



CNT



Graphene



Graphene  
oxide

杜昆樺 碩士 民國 100 年 6 月

# 國立臺灣大學碩士學位論文 口試委員會審定書

論文中文題目：奈米碳材於高分子太陽能電池上之應用

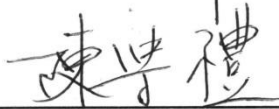
論文英文題目：Nanocarbon based polymer solar cells

本論文係杜昆樺(R98527030)在國立臺灣大學材料科學與工程學系、所完成之碩士學位論文，於民國 100 年 6 月 23 日承下列考試委員審查通過及口試及格，特此證明

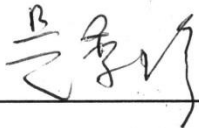
口試委員：陳俊維  
(指導教授)



陳學禮

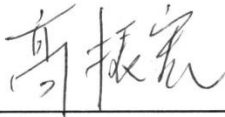


吳季珍



系主任、所長

高振宏



(簽名)

## Acknowledgements

時光匆匆，回想當初剛進實驗室時還是個懵懵懂懂的大三專題生，到現在已經碩士畢業，也看到自己的努力有了成果，心中不由得充滿了深深的感動。這段時光以來，從吸收知識與學習操作，到最後設計實驗和投入研究，所增進的不只是知識上的深度，更是許多未來生活做事的方法與宏觀角度，而這些，都要感謝一路上許多人的支持與幫助。

首先要感謝我的指導教授陳俊維老師。老師對研究的熱誠與嚴謹，深深影響我在做人做事上的態度。感謝老師對於學生想法的尊重以及寶貴的意見指導與相互討論，並提供了優良的研究環境，讓我能順利自由地進行研究，培養獨立思考的能力，且透過討論讓思考更加全面、完整。另外也感謝老師提供了難得的機會讓我能出國參加國際研討會，讓我從兩次的會議中獲得許多寶貴經驗，更進一步擴展自己的視野。此外，更感謝老師在生活上的幫助與經驗分享，帶給我不少啟發，讓我能跳脫框架去追求自己的夢想。

接著感謝口試委員陳學禮教授、吳季珍教授，在我口試時不吝嗇的給予指導與討論，提供許多寶貴的意見，讓這本論文能更臻完備。

感謝實驗室的學長與學弟妹們，以及所有在各方面給予我協助的人。感謝李紹先學長不厭其煩地提供量測及經驗上的協助，並不時的與我討論及給予建議。感謝林雲躍學長、林志誠學長、王迪彥學長提供的珍貴意見及協助，也感謝黃炯源學長在石墨烯成長上不吝嗇的指導與幫忙。除此之外，感謝葉雲傑學長、朱叢鴻學長、莊家豪學長、曾云亨學長、謝孟翔學長以及王瑜、何柏勳、楊雅婷、邵騰緯、鍾怡萱等學弟妹們，給我的協助與鼓勵，以及在實驗室事務上各種大小事的幫忙。更感謝李昱瑩在一路上的陪伴，幫助我度過許多研究上及生活上各種瓶頸。非常高興能和這群夥伴們一起相處，分享實驗及生活，讓我在碩士的研究路上，充滿了許許多多的歡笑與美好回憶。

最後，我要感謝我的父母親，從小到大總是在背後默默支持的我、鼓勵我，不辭辛勞只為提供我良好的讀書環境，並讓我自由選擇自己的路，這份愛與恩情，雖然無法報答，但永遠銘記在我心中。如今我順利地拿到了碩士學位，謹將這份成果與榮耀，獻給我最愛的父母親。



## 摘要

有機高分子太陽能電池具有低成本、可撓曲且能大面積製造的優勢，因而吸引大家廣泛的興趣。然而，目前高分子太陽能電池在應用上還有一些不利的因素，其陽極材料氧化銻錫透明電極不易撓曲且價格日益升高，電洞傳輸層 PEDOT:PSS 有吸濕性且容易在紫外光下衰退，陰極的低功函數金屬則是在大氣中容易氧化不穩定。因此，此研究的目的是利用奈米碳材穩定的化學性質以及其良好的導電和可撓曲特性，藉以取代原本高分子太陽能電池中陰陽極和電洞傳輸層的材料，發展出以奈米碳材為基材的高分子太陽能電池。其一是以一維奈米碳管為透明導電電極，二維氧化態石墨烯為電洞傳輸層，兩者結合做為高分子太陽能電池的陽極平台，此元件表現出與一般元件接近的光電轉換效率，且具有可撓曲、可水溶液製程且大面積製造的優點。另外則是分別以 n 型及 p 型摻雜後的石墨烯做為太陽能電池中的陰陽極，發展出可以用 roll-to-roll 連續卷軸生產方式的元件，加上其半透明且可撓曲的優點，更有利於未來低成本製造和多元的應用。這兩種以奈米碳材為基材的高分子太陽能電池，成功結合了奈米碳材與高分子太陽能電池的優點，充分展現了其未來在生產及實際應用上的潛力。

## Abstract

Polymer solar cells have attracted a great interest for fabricating low-cost large-area mechanically flexible photovoltaic devices compared to the conventional inorganic counterparts. But the conventionally used ITO anode, PEDOT:PSS, and the low work function metal cathode all have its own shortcomings, hindering the devices from practical application. In this research, we would like to demonstrate new architectures of polymer solar cells based on allotropes of carbon nanomaterials, by utilizing p-type doped graphene or single walled carbon nanotube (SWNT) thin film as the anode, graphene oxide (GO) as the hole transport layer, n-type doping graphene as the cathode, and fullerene derivative PCBM/P3HT bulk heterojunctions as the photoactive layer. The photovoltaic device based on the solution processed SWNT/GO platform has exhibited good power conversion efficiency of 3.1% as compared to the conventional device (PCE=3.57%). And the new innovation of polymer solar cell based on all-graphene electrodes provides a potential route to develop a flexible, semitransparent photovoltaic device which can be fully integrated with the low-cost, roll-to-roll fabrication process. By overcoming the drawbacks of polymer solar cells, these two approaches have shown the potential of serving the long-term solutions for the future energy supply.

# Contents

口試委員會審定書 .....	I
Acknowledgements .....	II
摘要 .....	IV
Abstract .....	V
Contents.....	VI
List of Figures .....	IX
List of Tables .....	XIII
List of Publications .....	XIV
<b>Chapter 1 Introduction .....</b>	<b>1</b>
<b>1.1. The demand for alternative energy .....</b>	<b>2</b>
<b>1.2. Conventional inorganic solar cell .....</b>	<b>3</b>
<b>1.3. Organic/polymer photovoltaics.....</b>	<b>5</b>
<b>1.4. Carbon based nanomaterials .....</b>	<b>10</b>
1.4.1. Fullerene and fullerene derivatives .....	10
1.4.2. Single walled carbon nanotube .....	11
1.4.3. Graphene .....	15
<b>1.5. Research motivation .....</b>	<b>17</b>
<b>1.6. Reference.....</b>	<b>18</b>
<b>Chapter 2 Experimental setup.....</b>	<b>21</b>
<b>2.1. Solar cell characterization.....</b>	<b>22</b>
2.1.1. Air mass 1.5 solar spectrum .....	22
2.1.2. External quantum efficiency .....	23



2.1.3. Transient photovoltage (TPV).....	24
<b>2.2. Transparent conducting electrode characterization .....</b>	<b>26</b>
2.2.1. UV-visible spectroscopy.....	26
2.2.2. Sheet resistance measurement.....	26
<b>2.3. Raman spectroscopy .....</b>	<b>28</b>
<b>2.4. Surface morphology and surface potential measurement.....</b>	<b>30</b>
2.4.1. Atomic force microscopy (AFM).....	30
2.4.2. Kelvin probe force microscopy (KPFM) .....	32
<b>2.5. Hall effect measurement .....</b>	<b>34</b>
<b>Chapter 3 Solution processable nanocarbon platform for polymer solar cells.....</b>	<b>35</b>
<b>3.1. Introduction.....</b>	<b>35</b>
<b>3.2. SWNT conducting thin film as transparent electrode .....</b>	<b>37</b>
3.2.1. The preparation of SWNT electrode .....	37
3.2.2. Characterization of SWNT electrode .....	39
<b>3.3. Graphene oxide as hole transport layer in OPVs.....</b>	<b>42</b>
3.3.1. The preparation of graphene oxide .....	43
3.3.2. Characterization of graphene oxide .....	45
<b>3.4. P3HT:PCBM polymer solar cell on the SWNT/GO nanocarbon platform</b>	
.....	<b>49</b>
3.4.1. Experimental details.....	49
3.4.2. Characterization of SWNT/GO platform .....	51
3.4.3. Solar cell device characteristics .....	53
<b>3.5. Conclusion .....</b>	<b>61</b>
<b>3.6. Reference.....</b>	<b>62</b>

<b>Chapter 4 Polymer solar cells based on all-graphene electrodes .....</b>	<b>67</b>
<b>4.1. Introduction.....</b>	<b>67</b>
<b>4.2. Graphene as transparent conducting electrode .....</b>	<b>70</b>
4.2.1. The synthesis of graphene on copper foil .....	70
4.2.2. The preparation of graphene electrode.....	71
<b>4.3. Work function engineering of graphene electrodes by using     layer-by-layer doping technique.....</b>	<b>73</b>
4.3.1. The preparation of p-type doping graphene electrode .....	74
4.3.2. The preparation of n-type doping graphene electrode .....	75
4.3.3. Characterization of LbL doped graphene electrode .....	76
<b>4.4. P3HT:PCBM polymer solar cells with n- and p-type doped graphene     electrodes .....</b>	<b>88</b>
4.4.1. Experimental details.....	88
4.4.2. Device with p-type doped graphene as the anode .....	89
4.4.3. Device with n-type doped graphene as the cathode .....	91
4.4.4. Device with all-graphene electrodes .....	93
<b>4.5. Conclusion .....</b>	<b>96</b>
<b>4.6. Reference.....</b>	<b>97</b>
 <b>Chapter 5 Conclusion .....</b>	 <b>102</b>
<b>5.1. Conclusions.....</b>	<b>102</b>
<b>5.2. Suggestions for future investigations .....</b>	<b>103</b>

## List of Figures

<b>Figure 1.1</b> Operation mechanism of inorganic solar cells .....	4
<b>Figure 1.2</b> Crystalline Si solar cell modules .....	4
<b>Figure 1.3</b> Roll-to-roll manufacturing process of polymer photovoltaics [3] .....	5
<b>Figure 1.4</b> Schematic working mechanisms of OPVs. (a) Absorption of a photon leading to generation of an exciton. (b) Exciton diffuse to the interface of donor and acceptor. (c) Charge separation through exciton dissociation at the donor/acceptor interface. (d) Electron and hole transport to the anode and cathode respectively. ....	7
<b>Figure 1.5</b> The structure evolution of organic/polymer solar cell. (a) Single layer structure (b) bi-layer structure (c) Bulk heterojunction structure .....	8
<b>Figure 1.6</b> (a) C60 buckyball (b) PCBM .....	11
<b>Figure 1.7</b> Schematic of three configurations of single walled carbon nanotubes. ....	12
<b>Figure 1.8</b> Relation between the hexagonal carbon lattice and the chirality of single walled carbon nanotubes.....	12
<b>Figure 1.9</b> (a) 3-D illustration of the dispersion relation for graphene including the allowed states for the (3,3) SWNT. The periodic boundary conditions along the circumference of the tube result in a discrete set of allowed $k_y$ values. (b) Projection of the allowed states onto the first Brillouin zone of graphene. Obviously, the K-points are allowed states for CNTs of this chirality. (c) 2-D illustration of the dispersion $W(k_x)$ . The states at the Fermi level indicate the metallic behavior of this tube. The periodicity volume in the k-space is given by the interval from $-\pi/P$ to $+\pi/P$ . [22] .....	14
<b>Figure 1.10</b> (a) 3-D illustration of the dispersion relation for graphene including the allowed states for the (4,2) SWNT. The periodic boundary conditions along the circumference of the tube result in a discrete set of allowed k values. (b) Projection of the allowed states onto the first Brillouin zone of graphene. Obviously, the K points are no allowed states for CNTs of this chirality. (c) 2-D illustration of the dispersion $W(k)$ . the conduction band and the valence band are separated by a bandgap. [22].....	14
<b>Figure 1.11</b> (a) Schematic of graphene sheet (b) 3D illustration band structure of graphene. (www.sciencefriday.com/ news/030107/graphene.jpg) .....	15
<b>Figure 2.1</b> Schematic of the path length difference of the solar irradiation through the Earth's atmosphere in units of air mass (AM). ....	22
<b>Figure 2.2</b> External quantum efficiency (EQE) system setup. ....	23
<b>Figure 2.3</b> Schematic of a band diagram in transient photovoltage setup .....	25

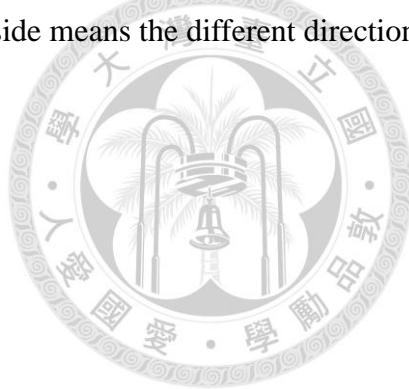
<b>Figure 2.4</b>	A typical transient photovoltage decay curve.....	25
<b>Figure 2.5</b>	Geometry for defining resistivity (left) and sheet resistance (right). .....	27
<b>Figure 2.6</b>	Schematic of energy level diagram related to Raman scattering. ....	29
<b>Figure 2.7</b>	The schematic of basic components in AFM system. ....	31
<b>Figure 2.8</b>	Schematic of Kelvin probe force microscopy. ....	32
<b>Figure 2.9</b>	Schematic of the sample we prepared for Hall effect measurement. ....	34
<b>Figure 3.1</b>	Raman spectra of raw and purified SWNTs.....	38
<b>Figure 3.2</b>	The schematic of fabricating the SWNT thin film electrode. ....	39
<b>Figure 3.3</b>	The transmission spectra of SWNT thin film with different filtration volume. (Inset) The photograph of transferred SWNT thin film on the glass substrate. .....	40
<b>Figure 3.4</b>	The transmittance@550nm versus sheet resistance of SWNT electrode. ....	40
<b>Figure 3.5</b>	(a) Large-area SWNT thin film on glass substrate. (b) Flexible SWNT thin film on PET substrate. (c) The planar view of SWNT thin film under scanning electron microscopy (SEM). (d) The SEM cross section of SWNT thin film, which shows the extremely high flexibility of SWNT thin film. ....	41
<b>Figure 3.6</b>	(a) Schematic device structure of using GO as hole transport layer in conventional P3HT:PCBM polymer solar cell. (b) Current-voltage characteristics of photovoltaic devices with no hole transport layer (labeled with ITO), with 30nm PEDOT:PSS and with 1 layer GO as hole transport layer.....	42
<b>Figure 3.7</b>	The flow chart of synthesizing GO and making GO solution. The long circle means the action we taken and the rectangle means the substances we used or obtained. ....	44
<b>Figure 3.8</b>	(a) TEM image of as-prepared GO sheet on a lacey carbon support. (b) SAED pattern; the diffraction spots are labeled with MillerBravais indices. (c) Relative intensity profile obtained from the diffraction pattern in (b)... ..	46
<b>Figure 3.9</b>	The AFM height image of a GO sheet on Si substrate and the corresponding height profile.....	46
<b>Figure 3.10</b>	The Tauc plot measurement obtained from the absorption spectrum of GO. .....	48
<b>Figure 3.11</b>	The HOMO level of GO determined by Riken Keiki AC-2 photoionization measurement. ....	48
<b>Figure 3.12</b>	(a) 1 layer, (b) 3 layers, (c) 6 layers GO thin films deposited on flat silicon substrates.....	50
<b>Figure 3.13</b>	Dependence of the GO thin film thickness as a function of different number of layers. ....	50
<b>Figure 3.14</b>	SEM planar view of SWNT electrode with (a) none, (b) 1 layer and (c) 3	

layers GO thin film. (d)–(f) The corresponding SEM cross section images. .....	51
<b>Figure 3.15</b> AFM height image of SWNT electrode with (a) none, (b) 1 layer and (c) 3 layers GO thin film. (d)–(f) The corresponding KPFM images. ....	52
<b>Figure 3.16</b> The cross sectional TEM image of the nanocarbon based polymer solar cell of SWNT/GO/P3HT:PCBM/Al. ....	53
<b>Figure 3.17</b> The relevant energetics of the polymer solar cell based on the SWNT/GO/P3HT:PCBM/Al device structure. ....	53
<b>Figure 3.18</b> The current-voltage characteristics of the SWNT/GO/P3HT:PCBM/Al solar cells with different thicknesses of GO layers. (under A.M.1.5, 100 mW/cm <sup>2</sup> illumination) GO1, GO3 and GO6 correspond to one, three and six layers of GO. ....	55
<b>Figure 3.19</b> The photovoltaic performances of SWNT/r-GO/P3HT:PCBM/Al devices consisting of one layer of GO thin films reduced with different hydrazine exposure time. ....	56
<b>Figure 3.20</b> (a) Photovoltage transient decay curves of SWNT/GO (or no GO) /P3HT:PCBM/Al solar cell device. (b) Power dependent recombination rates of the two devices in (a). ....	58
<b>Figure 3.21</b> Conductive-AFM current-voltage characteristics of the devices consisting of one, three and six layers of GO thin films onto the SWNT electrodes. ...	60
<b>Figure 3.22</b> The transient photovoltage decay curves of the SWNT/GO/P3HT:PCBM/Al solar cell devices. ....	60
<b>Figure 4.1</b> Schematic device structure of all-graphene polymer solar cell. ....	69
<b>Figure 4.2</b> (a) Schematic of graphene growth by CVD. (b) Illustration of the graphene growth process. ....	70
<b>Figure 4.3</b> Schematic of the roll-to-roll production of graphene films grown on Cu foil. ....	71
<b>Figure 4.4</b> The photograph of different layers graphene on same glass substrate. ....	72
<b>Figure 4.5</b> SEM planar view image of four layer graphene films. The white line areas were the wrinkles of graphene films. ....	72
<b>Figure 4.6</b> AFM height image of four layers graphene films. The wrinkles of graphene films were clearly visible. ....	72
<b>Figure 4.7</b> Schematics of Fermi level changes in graphene band structure after n- and p-type doping process. ....	73
<b>Figure 4.8</b> The process of fabricating layer-by-layer p-type doped graphene electrode. ....	74
<b>Figure 4.9</b> The chemical structure of poly(ethyleneimide) (PEI). ....	76
<b>Figure 4.10</b> The process of fabricating layer-by-layer n-type doped graphene electrode.	

.....	76
<b>Figure 4.11</b> The XPS (a) C1s and (b) N1s spectra of pristine and doped graphene films.	76
.....	77
<b>Figure 4.12</b> Raman spectra of pristine and doped single layer graphene.	78
<b>Figure 4.13</b> The G-band peaks of pristine and doped graphene.	80
<b>Figure 4.14</b> $I_d-V_G$ characteristics of pristine and doped single layer graphene FETs....	82
<b>Figure 4.15</b> The sheet resistance of pristine and doped graphene with different layers.	83
<b>Figure 4.16</b> The carrier densities dependent on different layers of graphene.....	83
<b>Figure 4.17</b> (a) Transmission spectra of pristine graphene films with different layers. (b) Transmission spectra of pristine and doped graphene films with 4 layers. .	84
<b>Figure 4.18</b> The transmittance at 550 nm of graphene films as a function of their resistance before and doping process. ....	85
<b>Figure 4.19</b> (a) Surface morphology and (b) workfunction mapping of 4 layers pristine graphene films. ....	86
<b>Figure 4.20</b> (a) Surface morphology and (b) workfunction mapping of 4 layers $HNO_3$ doped graphene films.....	86
<b>Figure 4.21</b> (a) Surface morphology and (b) workfunction mapping of 4 layers PEI doped graphene films.....	86
<b>Figure 4.22</b> The graphene workfunctions depend on different layers of graphene films. ....	87
<b>Figure 4.23</b> (a) Schematic of the device structure with p-type graphene as anode. (b) The corresponding energy band diagram of the device in figure (a).....	90
<b>Figure 4.24</b> The current-voltage characteristics of the p-type graphene /GO/P3HT:PCBM/Al polymer solar cell.....	90
<b>Figure 4.25</b> (a) Schematic of the device structure with n-type graphene as cathode. (b) The corresponding energy band diagram of the device in figure (a).....	92
<b>Figure 4.26</b> The current-voltage characteristics of the ITO/GO/P3HT:PCBM/n-type graphene polymer solar cell.....	92
<b>Figure 4.27</b> (a) The schematic device structure of the polymer photovoltaic device based on all-graphene electrode. (b) The corresponding energy band diagram of the device in figure (a). ....	94
<b>Figure 4.28</b> The current-voltage characteristics of the p-type graphene/GO/P3HT:PCBM/n-type graphene polymer solar cell.....	94

## List of Tables

<b>Table 3.1</b> Summary of the photovoltaic performance of different devices as described in the text. The SWNT/GO corresponds to the devices consisting of different number layers of GO as the interfacial layer. The SWNT/r-GO corresponds to the devices consisting of one layer of r-GO with different hydrazine exposure time. The control device consists of the device structure of ITO/PEDOT:PSS/P3HT:PCBM/Al.....	56
<b>Table 4.1</b> The value of FWHM(G), G-band position, $I(2D)/I(G)$ in the Raman spectra of pristine and doped graphene.(fig4.12) .....	80
<b>Table 4.2</b> The solar cell characteristics of the device based on ITO and graphene anode. ....	91
<b>Table 4.3</b> The solar cell characteristics of the device with n-type graphene cathode. ITO and graphene side means the different directions of photo illumination. ....	93
<b>Table 4.4</b> The solar cell characteristics of the device with all graphene electrode. P- and n-type graphene side means the different directions of photo illumination...	94



## List of Publications

### 期刊論文 (Journal paper)

1. **Kun-Hua Tu**, Shao-Sian Li, Wei-Chih Li, Jer-Ren Yang and Chun-Wei Chen\*, Solution Processable Nanocarbon Platform for Polymer Solar Cells, *Energy & Environmental Science*, in press (2011). **(SCI, impact factor 9.446)**
2. **Shao-Sian Li**<sup>†</sup>, **Kun-Hua Tu**<sup>†</sup>, Chih-Cheng Lin, Chun-Wei Chen\* and Manish Chhowalla, Solution-Processable Graphene Oxide as an Efficient Hole Transport Layer in Polymer Solar Cells, *ACS Nano* **4**, 3169-3174 (2010). <sup>†</sup>equally contributed **(SCI, impact factor 9.855)**
3. Yu-Ying Lee, **Kun-Hua Tu**, Chen-Chieh Yu, Shao-Sian Li, Jeong-Yuan Hwang, Chih-Cheng Lin, Kuei-Hsien Chen, Li-Chyong Chen, Hsuen-Li Chen, and Chun-Wei Chen\*, Top Laminated Graphene Electrode in a Semitransparent Polymer Solar Cell by Simultaneous Thermal Annealing/Releasing Method, *ACS Nano*, in press (2011). **(SCI, impact factor 9.855)**
4. S. W. Wang, H. E. Lin, H.-D. Lin, K. Y. Chen, **K.-H. Tu**, Chun-Wei Chen, J.-Y. Chen, C.-H. Liu, Chi-Te Liang and Yang Fang Chen, Transport Behavior and Negative Magnetoresistance in Chemically Reduced Graphene Oxide Nanofilms *Nanotechnology*, in press (2011). **(SCI, impact factor 3.664)**
5. Chih-Cheng Lin, Di-Yan Wang, **Kun-Hua Tu**, You-Ting Jiang, Meng-Hsiang Hsieh, Chia-Chun Chen, and Chun-Wei Chen\*, Enhanced Infrared Light Harvesting of Inorganic Nanocrystal Photovoltaic and Photodetector on Graphene Electrode, *Applied Physics Letters* **98**, 263509 (2011). **(SCI, impact factor 3.820)**



研討會論文 (Conference paper)

1. **Kun-Hua Tu**, Shao-Sian Li, Wei-Chih Li, Jer-Ren Yang, Chun-Wei Chen\*, Polymer Solar Cells Based on Solution Processable Nanocarbon Platform, **MRS spring 2011**, San Francisco, USA.
2. **Kun-Hua Tu**, Shao-Sian Li, Yu-Ying Lee, Chih-Cheng Lin, Manish Chhowalla, Chun-Wei Chen\*, **2010 International Symposium on Graphene, CNT and Ultrafast Phenomena of Nanomaterials**, Taipei, Taiwan. **(Best Poster Award)**
3. **Kun-Hua Tu**, Yun-Yue Lin, Steve Miller, Hsin-An Chen, I-Sheng Chen, Manish Chhowalla, and Chun-Wei Chen\*, Surface Functionalized Single Walled Carbon Nanotube Electrodes on the Performance of Polymer Photovoltaics, **PVSEC-19**, Jeju, South Korea.



## Chapter 1 Introduction

Global warming has become a practical issue. Fossil fuel was also predicted to be exhausted in the coming decades. As a free, clean and renewable energy source, solar energy provides people a reliable alternative for the future energy supply. The polymer solar cells have been developed in recent years with the benefits of light weight, low-cost and mechanically flexible compared to inorganic solar cells. At the same time, the nano-scaled carbon allotropes, fullerene, carbon nanotube and graphene, have been discovered. These low-dimensional carbon nanomaterials have exhibited extraordinary electrical and mechanical properties and showed a great potential to be applied on the future electronics. It motivated my research to focus on integrating the advantages of carbon nanomaterials into PV technology. Therefore, the polymer solar cells based on these carbon nanomaterials were developed.

## 1.1. The demand for alternative energy

Since the industrial revolution brought new manufacturing technologies in 19<sup>th</sup> century, the global energy demand continues to increase every year, especially in the past decades. Until now, the fossil fuels (oil, coal, natural gas) have covered the most of total energy demand in the world. However, they are not inexhaustible and have their own limited reserves. Particularly, the oil was predicted to run out in the near few decades. The fossil fuels could not satisfy the energy demand in the future anymore. On the other hand, a huge amount of carbon dioxide (CO<sub>2</sub>) has been produced and emitted into the air while combusting the fossil fuels. The increasing concentration of CO<sub>2</sub> adds considerably to the greenhouse effect, which will raise the global mean surface temperature and increase the severity and frequency of natural disasters.

Finding alternative energy sources has become more important and urgent. Nuclear power plants have already satisfied people a great energy demand, but the security and health risk as well as the polluted nuclear waste are still unsolved problems. Fortunately, we have some renewable energy sources, such as wind power, hydropower, bio fuel, geothermal energy and solar energy. Due to the features of omnipresent, enormous and free, solar energy becomes one of the best candidates for the power supply in the future. Therefore, how to harvest solar energy efficiently at a low cost by using photovoltaic (PV) technology has become an essential issue deserving more efforts to put in.

## 1.2. Conventional inorganic solar cell

A solar cell or a photovoltaic cell is a device that converts energy of light directly into electricity by the photovoltaic effect. In 1954, the first solar cell was developed by Daryl Chapin at Bell Laboratories and the power conversion efficiency of this crystalline silicon solar cell had reached 6%. [1] Since then, the photovoltaic technology has become extensively studied and the highest efficiency has reached about 25% for crystalline Si solar cells nowadays. [2] Figure 1.1 illustrates the working mechanism of conventional inorganic solar cells. Practically, the conventional inorganic solar cells incorporate a semiconductor that is doped to form a p-n junction and a built-in electric field. When the light was absorbed by a solar cell, electron-hole pairs would be generated in semiconductor materials and then diffused to depletion region of p-n junction. Once the electron-hole pairs enter the depletion region, the electrons and holes would be directed by electric field toward the proper electrode, leading to photovoltage or photocurrent through the device. Besides Si solar cell, other inorganic solar cells using materials like Ge, GaAS and GaInP also achieved impressive efficiency at 20~30%. However, these solar cells have several disadvantages such as bulky modules (Fig1.2), complex fabrication processes and the limited availability of purified raw materials. Therefore, to ensure the sustainable technology path of photovoltaic, the development of new materials and new device architectures is required.

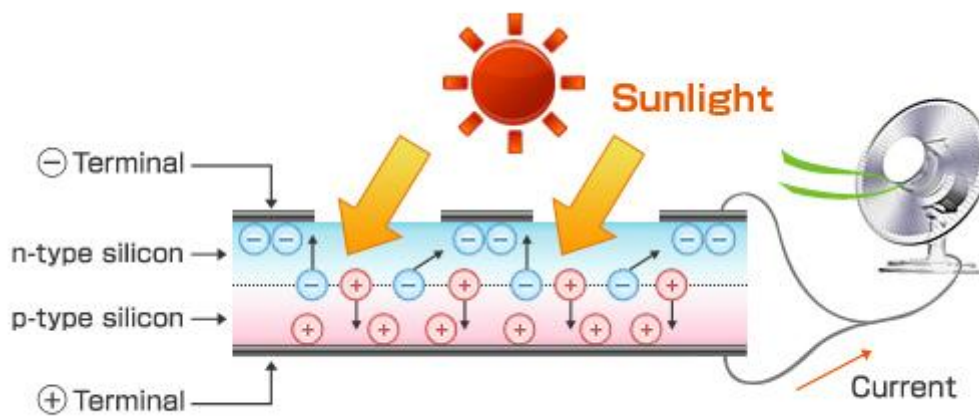


**Figure 1.1** Operation mechanism of inorganic solar cells

<http://www.sumcosi.com/english/products/solar/structure.html>



**Figure 1.2** Crystalline Si solar cell modules

[http://en.wikipedia.org/wiki/Photovoltaic\\_system](http://en.wikipedia.org/wiki/Photovoltaic_system)

### 1.3. Organic/polymer photovoltaics

Organic materials have the potential to develop a long-term PV technology due to its suitability for large-scale manufacturing and the unlimited availability of raw materials. Organic semiconductors are a less expensive alternative to inorganic semiconductors like Si, and they can have high optical absorption coefficient which offer the possibility to produce thin film solar cells. Also there are some additional attractive features, such as high flexibility, light weight and large-scale producible by employing roll-to-roll manufacturing process [3], making the organic/polymer solar cells become a promising one for the future PV technology.



**Figure 1.3** Roll-to-roll manufacturing process of polymer photovoltaics [3]

#### **The working principle of organic photovoltaic (OPV) devices**

The conversion of photons into electricity in OPVs is fundamentally different from inorganic devices. OPVs are comprised of electron donor and electron acceptor materials compared to inorganic semiconductor p-n junction. When a photon with

appropriate energy is absorbed by the OPV, a ground state electron would be elevated from the HOMO (Highest Occupied Molecular Orbital) to the LUMO (Lowest Unoccupied Molecular Orbital) in the donor material. However, the electron and the resulting hole are strongly bounded as an exciton because of the localized electronic wave functions in organic molecules and their Coulomb attraction. In order to dissociate the exciton into free electron and hole, an interface across which the chemical potential of electron decreases must be provided. Therefore the electron acceptor molecules would be introduced into the donor polymer matrix and act as dissociation centers. But if the chemical potential of electron acceptor is not adequate or the exciton is not sufficiently close to the donor/acceptor interface, the exciton will recombine or transfer its energy to the polymer matrix. Figure 1.4 shows the proper energy band alignment and the working mechanism of OPV devices. In summary, the process of converting light into current in OPVs accomplished in four steps: (1) absorption of a photon leading to generation of an exciton, (2) the exciton diffuse to the interface of donor and acceptor, (3) charge separation through exciton dissociation at the donor/acceptor interface, (4) electron and hole transport to the anode and cathode respectively.

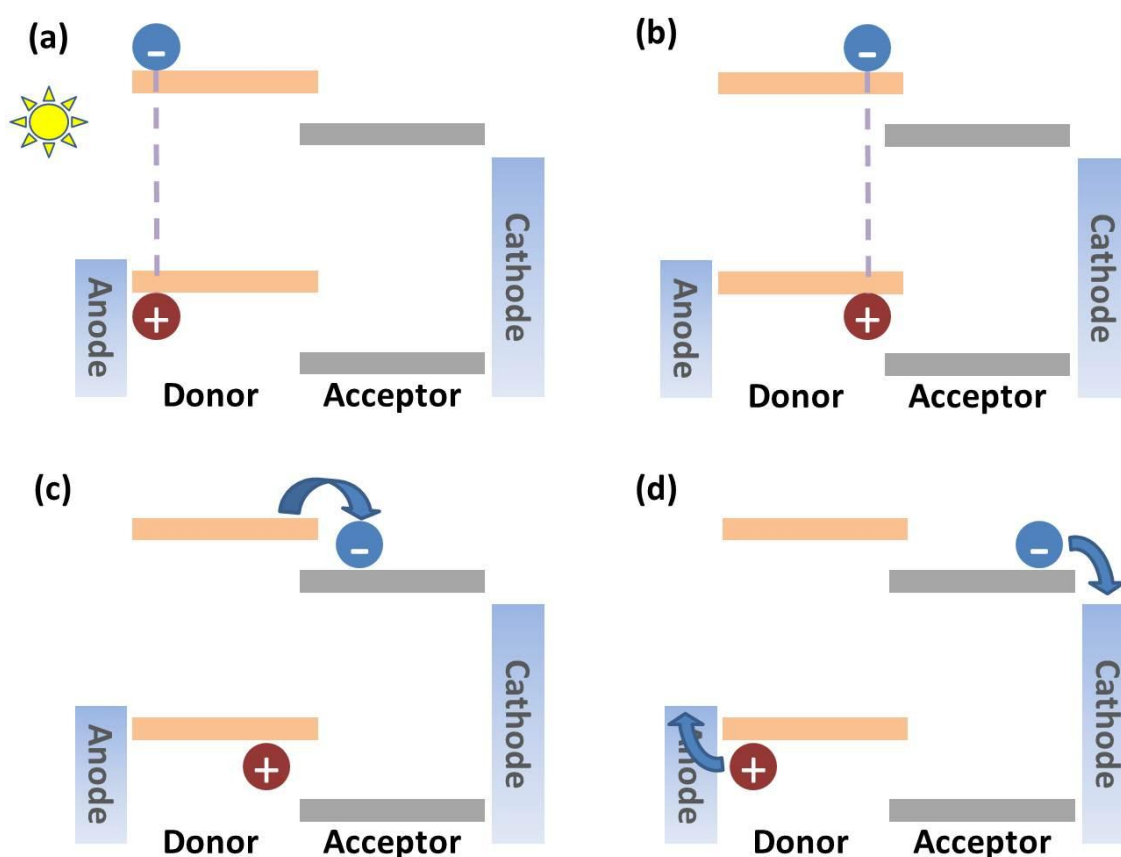


**Figure 1.4** Schematic working mechanisms of OPVs. (a) Absorption of a photon leading to generation of an exciton. (b) Exciton diffuse to the interface of donor and acceptor. (c) Charge separation through exciton dissociation at the donor/acceptor interface. (d) Electron and hole transport to the anode and cathode respectively.

### The architectures of organic/polymer solar cells

The historical evolution of organic/polymer solar cells was start from single layer structure (Fig1.5(a)), followed by bi-layer structure (Fig1.5(b)) and the bulk heterojunction structure (Fig1.5(c)) commonly used nowadays.[4] The first single layer structure was proposed by T. Feng in 1978.[5] This MIS-Schottky barrier-type solar cell was formed by sandwiched the donor material, merocyanine, between the silver and semitransparent aluminum electrode. The conversion efficiency was only 0.7% due to



the poor absorption of light and the insufficient charge separation. Then the bi-layer structure was first proposed by C. W. Tang in 1986.[6] Using copper phthalocyanine (CuPc) as donor and a perylene tetracarboxylic derivative as acceptor, the two layer heterojunction organic solar cell had reached the power conversion efficiency about 1%. Some other conjugated polymer based bi-layer solar cells were also demonstrated in the next few years; however, the efficiencies were still low.[7,8] There were several persistent limitations prevented the dramatic increase of the efficiency. Specifically, since charge dissociation occurred at the interface, the loss due to exciton recombination (diffusion length < 20nm) was prevalent. Furthermore, since carrier mobility in organic layers was low, dissociated charge losses due to traps was also high.[9] In order to enhance exciton dissociation and carrier transport properties, an interpenetrating network of donors and acceptors, referred to as bulk heterojunctions, was developed.

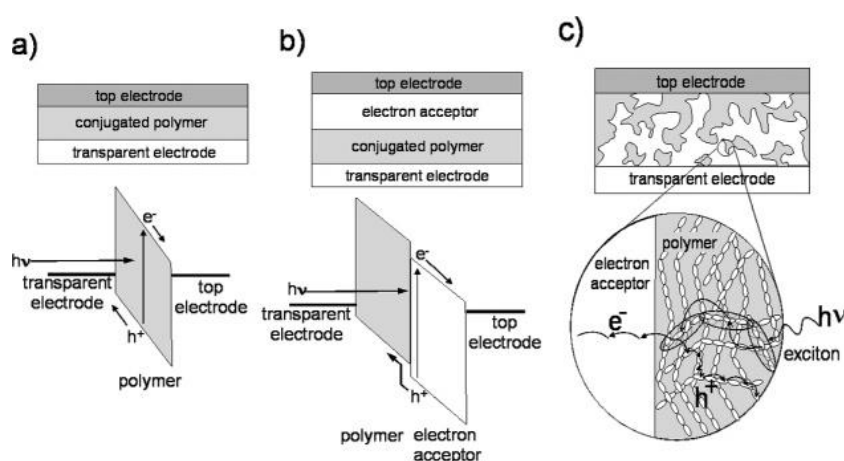


**Figure 1.5** The structure evolution of organic/polymer solar cell. (a) Single layer structure (b) bi-layer structure (c) Bulk heterojunction structure

In 1992, N.S. Sariciftci and A. J. Heeger discovered significant photoluminance (PL) quenching of MEH-PPV by blending C<sub>60</sub> into MEH-PPV polymer matrix, which is an evidence of efficient exciton dissociation at the donor/acceptor interface.[10] Based on this concept, A. J. Heeger proposed the first bulk heterojunction polymer/fullerene solar cell with MEH-PPV as the donor and C<sub>60</sub> as the acceptor, showing an order of magnitude larger than the pure polymer in photosensitivity. Since then, the bulk heterojunction devices have attracted lots of interests and become a major topic in the organic/polymer solar cell field. So far, the most popular bulk heterojunction OPV is based on poly(3-hexylthiophene)(P3HT) and phenyl-C61-butyric acid methyl ester (PCBM) and reached about 5% efficiency reported by A. J. Heeger.[11] By utilizing low bandgap polymer as the donor material in further, the highest efficiency of bulk heterojunction OPV has already moved forward to 7.4% reported by Liang recently.[12]

## 1.4. Carbon based nanomaterials

Atomic carbon is a very short-lived species and, therefore, carbon is stabilized in various allotropes with different dimensions. Ranging from 3D to 0D, diamond and graphite, graphene, carbon nanotube, and fullerene, all the carbon allotropes exhibit extraordinary properties in different aspects which have been extensively researched not only in the science but also in the engineering. The thesis mainly focuses on utilizing carbon nanomaterials in the OPVs, so the brief overviews of fullerene, single walled carbon nanotube and graphene are given in the following sections.

### 1.4.1. Fullerene and fullerene derivatives

A fullerene is any molecule composed entirely of carbon, in the form of a hollow sphere, ellipsoid, or tube. C<sub>60</sub> buckyball (Fig. 1.6(a)) was first discovered by H. W. Kroto at Rice University in 1985 and shortly thereafter came to the fullerenes.[13] Because of having the high electron affinity,[14] C<sub>60</sub> molecules were used as the electron acceptor in OPVs. However, the poor solubility and electron transport properties of C<sub>60</sub> limited the power conversion efficiencies of OPVs. Therefore, the fullerene derivative phenyl-C<sub>61</sub>-butyric acid methyl ester (PCBM) (Fig. 1.6(b)) was developed to replace C<sub>60</sub> as the electron acceptor, resulting in the improved efficiency of the P3HT/PCBM bulk heterojunction polymer solar cell up to 5%.[11] Some further improvements of the OPV

efficiency by using some other modified fullerene molecules have also been reported recently.[15–18]

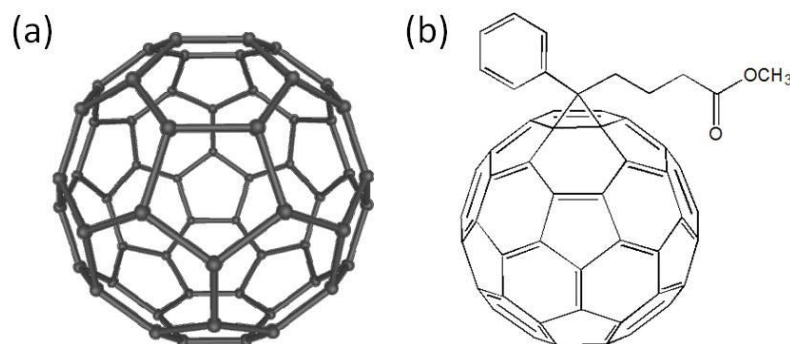


**Figure 1.6** (a) C<sub>60</sub> buckyball (b) PCBM

#### 1.4.2. Single walled carbon nanotube

Carbon nanotubes are allotropes of carbon with a cylindrical nanostructure. With the structure formed by rolling up graphene sheets, carbon nanotubes have a significantly large length to diameter ratio as being 1-D materials. The first carbon nanotubes were multi-walled carbon nanotubes grown by Sumio Iijima at NEC in 1991.[19] Then two years later, single walled carbon nanotubes (SWNT) were first synthesized by Iijima[20] and Bethune[21] using catalytic arc discharge method. Depending on the way the graphene sheet rolled up, the single walled carbon nanotubes can divide into three general configurations as shown in fig1.7: armchair, zig-zag and chiral.

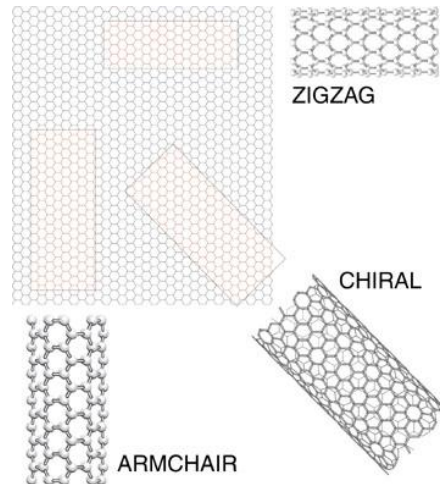


**Figure 1.7** Schematic of three configurations of single walled carbon nanotubes.

The different types of nanotubes can be described by the chiral vector  $(n, m)$ , where  $n$  and  $m$  are integers of the vector equation  $\mathbf{C}_h = n\mathbf{a}_1 + m\mathbf{a}_2$ .  $\mathbf{a}_1$  and  $\mathbf{a}_2$  are the unit vectors of the hexagonal lattice as described by the diagram in figure 1.8. By unwrapping the nanotube along its axis, two lines can be drawn to define the tube axis  $\mathbf{T}$  which is perpendicular to the chiral vector  $\mathbf{C}_h$ . SWNTs are referred to as ‘armchair’ while wrapping angle  $\phi$  equals zero, as ‘zigzag’ while  $\phi$  equals  $30^\circ$ , and as ‘chiral’ while  $\phi$  lies between  $0^\circ < \phi < 30^\circ$ .

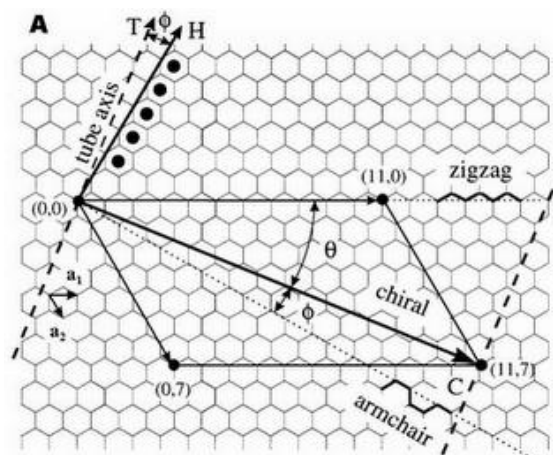


**Figure 1.8** Relation between the hexagonal carbon lattice and the chirality of single walled carbon nanotubes

[http://nanoall.blogspot.com/2008\\_11\\_09\\_archive.html](http://nanoall.blogspot.com/2008_11_09_archive.html)

The integers  $n$  and  $m$  determine the chirality of the SWNT, which define the electronic structure, lattice, and density, among other properties. Since a single walled carbon nanotube has the structure of a single graphene sheet rolled into a cylinder, the band structure and electronic properties of SWNTs can be extrapolated from the band structure of graphene. Figure 1.9(a) is the 2D energy band diagram of a graphene sheet and the black lines represent one-dimensional Brillouin zones of SWNT. And we can simply get the band structure of SWNT by folding all the other Brillouin zones back to the 1<sup>st</sup> Brillouin zone. So if one of the Brillouin zones has intersected the K-points of graphene's band structure, the conduction band and valence band of SWNT will contact each other, resulting into a metallic SWNT (Fig.1.10(a)-(c)); otherwise, the SWNT is semiconducting.(Fig.1.10(a)-(c)) In brief, the relationship between integers ( $n$ ,  $m$ ) and the electronic properties of SWNTs can be described by the following equation.

$$n - m = 3q \quad \text{Eq.1.1}$$

While  $q$  is an integer, the SWNT is considered to be metallic, and the other SWNTs are semiconducting.

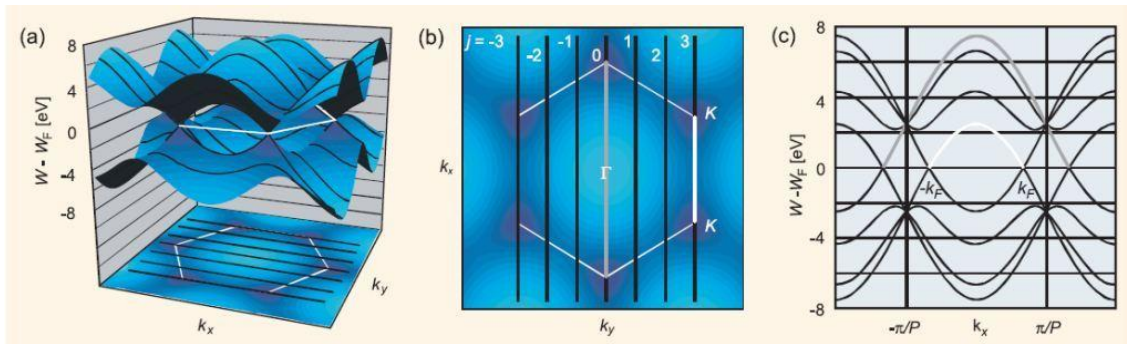


**Figure 1.9** (a) 3-D illustration of the dispersion relation for graphene including the allowed states for the (3,3) SWNT. The periodic boundary conditions along the circumference of the tube result in a discrete set of allowed  $k_y$  values. (b) Projection of the allowed states onto the first Brillouin zone of graphene. Obviously, the K-points are allowed states for CNTs of this chirality. (c) 2-D illustration of the dispersion  $W(k_x)$ . The states at the Fermi level indicate the metallic behavior of this tube. The periodicity volume in the k-space is given by the interval from  $-\pi/P$  to  $+\pi/P$ . [22]

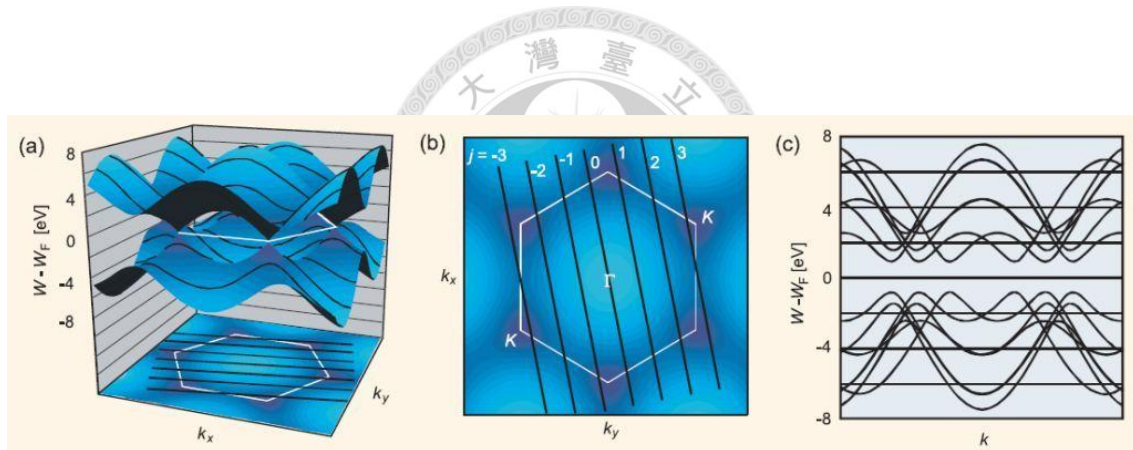


**Figure 1.10** (a) 3-D illustration of the dispersion relation for graphene including the allowed states for the (4,2) SWNT. The periodic boundary conditions along the circumference of the tube result in a discrete set of allowed  $k$  values. (b) Projection of the allowed states onto the first Brillouin zone of graphene. Obviously, the K points are no allowed states for CNTs of this chirality. (c) 2-D illustration of the dispersion  $W(k)$ . the conduction band and the valence band are separated by a bandgap. [22]

Until now, there are some techniques to produce carbon nanotubes in sizeable quantities, including arc discharge, laser ablation, high pressure carbon monoxide (HiPco), and chemical vapor deposition (CVD). SWNTs produced by these techniques do not have preferred chirality, so in general, one-thirds of the SWNTs are expected to be metallic, and the others are semiconducting.

### 1.4.3. Graphene

Graphene is an one-atom-thick planar sheet of  $sp^2$ -bonded carbon atoms that are densely packed in a honeycomb crystal lattice.(Fig.1.11) A single graphene sheet was first pulled out from graphite using Scotch tape by Andre Geim and Kostya Novoselov at Manchester University in 2004.[23] From then on, graphene has already attracted numerous fundamental and technological studies.

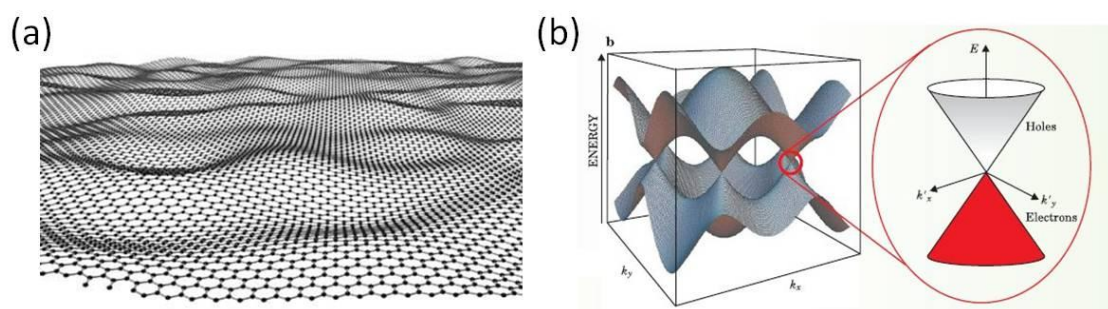


**Figure 1.11** (a) Schematic of graphene sheet (b) 3D illustration band structure of graphene. ([www.sciencefriday.com/news/030107/graphene.jpg](http://www.sciencefriday.com/news/030107/graphene.jpg))

Figure 1.11(b) shows the energy band structure of graphene. The E-k relation is linear for low energies near the six corners of the two-dimensional hexagonal Brillouin



zone, leading to zero effective mass for electrons and holes. Due to this linear (or “conical”) dispersion relation at low energies, electrons and holes near these six points behave like relativistic particles described by the Dirac equation for spin 1/2 particles.[24] Hence, the electrons and holes are called Dirac fermions, and the six corners of the Brillouin zone are called the Dirac points. There is no allowed state at the Dirac point, so graphene is generally considered as a semi-metal or zero-gap semiconductor.

As an exciting material, graphene has large specific surface area, high Young’s modulus ( $\sim 1.0$  TPa)[25] and thermal conductivity ( $\sim 5000$   $\text{Wm}^{-1}\text{K}^{-1}$ )[26] as well as shows good electrical conductivity and high intrinsic carrier mobility (up to  $200,000$   $\text{cm}^2\text{V}^{-1}\text{s}^{-1}$ ). All these extraordinary characteristics make graphene become a potential material to apply on the future electronics. However, the flake thickness, size and location are largely uncontrollable of mechanically exfoliated graphene. Fortunately, there are several ways to synthesis graphene. The most promising approach is growing graphene on transition metal surface by chemical vapor deposition (CVD).[27.28] In particular, recent developments on uniform single layer deposition of graphene on copper foils over large areas[29] have allowed access to high quality material, giving the opportunity to expand graphene from scientific research to industrial engineering.

### 1.5. Research motivation

Since the global warming becomes more serious issue due to the increasing emission of greenhouse gas, people are encouraged to conserve the energy and reduce the carbon footprint in our daily life. Over 180 countries also agreed with the Kyoto Protocol for the purpose to stabilize greenhouse gas concentrations in the atmosphere at a level that would prevent dangerous anthropogenic interference with the climate system. Nevertheless, besides passively trying to conserve energy and reduce carbon emission, we can do the things more positively. Maybe there is another effective way to acquire energy from carbon materials, not just through combustion of them. Carbon based nanomaterials have already shown extraordinary properties in various aspects. And it is suitable to incorporate the merits of carbon nanomaterials into PV systems. In the view of this thought, the thesis mainly focused on developing polymer solar cells based on carbon nanomaterials, providing a new route to realize the low-cost, large area organic photovoltaic technology. On the basis of this approach, to save the earth, we can not only conserve the energy and reduce the carbon emission but also use the nanocarbon based photovoltaics to produce green energy in the future.

## 1.6. Reference

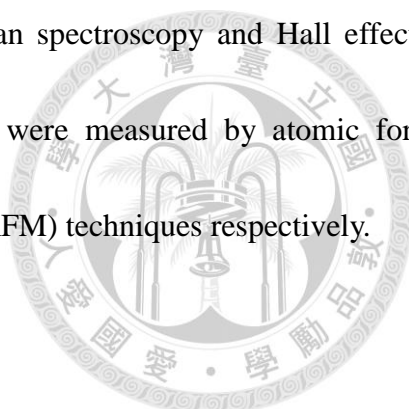
- [1] D. M. Chapin, C. S. Fuller, G. L. Pearson, A new silicon p-n junction photocell for converting solar radiation into electrical power, *Journal of Applied Physics* **25**, 676 (1954).
- [2] M. A. Green, K. Emery, Y. Hishikawa, W. Warta, Solar cell efficiency tables (version 37), *Prog. Photovolt: Res. Appl.* **19**, 84 (2011).
- [3] H. J. Park, M.-G. Kang, S. H. Ahn, L. J. Guo, A Facile Route to Polymer Solar Cells with Optimum Morphology Readily Applicable to a Roll-to-Roll Process without Sacrificing High Device Performances, *Adv. Mater.* **22**, E247 (2010).
- [4] K. M. Coakley, M. D. McGehee, Conjugated Polymer Photovoltaic Cells, *Chem. Mater.* **16**, 4533 (2004).
- [5] A. K. Ghosh, T. Feng, Merocyanine organic solar cells, *J. Appl. Phys.* **49**, 5982 (1978).
- [6] C. W. Tang, Two-layer organic photovoltaic cell, *Appl. Phys. Lett.* **48**, 183 (1986).
- [7] J. J. M. Halls, K. Pichler, R. H. Friend, S. C. Moratti, and A. B. Holmes, Exciton diffusion and dissociation in a poly(p-phenylenevinylene)/C60 heterojunction photovoltaic cell, *Appl. Phys. Lett.* **68**, 3120 (1996).
- [8] H. Spanggaard, F. C. Krebs, A brief history of the development of organic and polymeric photovoltaics, *Solar Energy Materials and Solar Cells* **83**, 125 (2004).
- [9] J. J. M. Halls, C. A. Walsh, N. C. Greenham, E. A. Marseglia, R. H. Friend, S. C. Moratti, A. B. Holmes, Efficient photodiodes from interpenetrating polymer networks, *Nature* **376**, 498 (1995).
- [10] N. S. Sariciftci, L. Smilowitz, A. J. Heeger, and F. Wudl, Photoinduced Electron Transfer from a Conducting Polymer to Buckminsterfullerene, *Science* **258**, 1474 (1992).

- [11] W. Ma, C. Yang, X. Gong, K. Lee, A. J. Heeger, Thermally Stable, Efficient Polymer Solar Cells with Nanoscale Control of the Interpenetrating Network Morphology, *Adv. Funct. Mater.* **15**, 1617 (2005).
- [12] Y. Liang, Z. Xu, J. Xia, S.-T. Tsai, Y. Wu, G. Li, C. Ray, L. Yu, For the Bright Future—Bulk Heterojunction Polymer Solar Cells with Power Conversion Efficiency of 7.4%, *Adv. Mater.* **22**, E135 (2010).
- [13] H. W. Kroto, J. R. Heath, S. C. O'Brien, R. F. Curl, R. E. Smalley, C<sub>60</sub>: Buckminsterfullerene, *Nature* **318**, 162 (1985).
- [14] R. F. Curl and R. E. Smalley, Probing C<sub>60</sub>, *Science* **242**, 1017 (1988).
- [15] J. Hou, H.-Y. Chen, S. Zhang, G. Li, Y. Yang, Synthesis, Characterization, and Photovoltaic Properties of a Low Band Gap Polymer Based on Silole-Containing Polythiophenes and 2,1,3-Benzothiadiazole, *J. Am. Chem. Soc.* **130**, 16144 (2008).
- [16] M. M. Wienk, M. Turbiez, J. Gilot, R. A. J. Janssen, Narrow-Bandgap Diketo-Pyrrolo-Pyrrole Polymer Solar Cells: The Effect of Processing on the Performance, *Adv. Mater.* **20**, 2556 (2008).
- [17] M. Lenes, G.-J. A. H. Wetzelaer, F. B. Kooistra, S. C. Veenstra, J. C. Hummelen, P. W. M. Blom, Fullerene Bisadducts for Enhanced Open-Circuit Voltages and Efficiencies in Polymer Solar Cells, *Adv. Mater.* **20**, 2116 (2008).
- [18] Y. He, H.-Y. Chen, J. Hou, Y. Li, *J. Am. Chem. Soc.* **132**, 1377 (2010).
- [19] S. Iijima, Helical microtubules of graphitic carbon, *Nature* **354**, 56 (1991).
- [20] S. Iijima, T. Ichihashi, Single-shell carbon nanotubes of 1-nm diameter, *Nature* **363**, 603 (1993).
- [21] D. S. Bethune, C. H. Klang, M. S. de Vries, G. Gorman, R. Savoy, J. Vazquez, R. Beyers, Cobalt-catalysed growth of carbon nanotubes with single-atomic-layer walls, *Nature* **363**, 605 (1993).
- [22] J. Appenzeller, E. Joselevich, W. Hönlein, Carbon Nanotubes for Data Processing,

- in "Nanoelectronics and Information Technology", eds. WILEY-VCH (2003).
- [23] K. S. Novoselov, A. K. Geim, S. V. Morozov, D. Jiang, Y. Zhang, S. V. Dubonos, I. V. Grigorieva, A. A. Firsov, Electric Field Effect in Atomically Thin Carbon Films, *Science* **306**, 666 (2004).
- [24] P. Avouris, Z. Chen, V. Perebeinos, Carbon-based electronics, *Nat. Nanotechnol.* **2**, 605 (2007).
- [25] C. Lee, X. Wei, J. W. Kysar, J. Hone, *Science* **321**, 385 (2008).
- [26] A. A. Balandin, S. Ghosh, W. Bao, I. Calizo, D. Teweldebrhan, F. Miao, C. N. Lau, Superior Thermal Conductivity of Single-Layer Graphene, *Nano Lett.* **8**, 902 (2008).
- [27] K. S. Kim, Y. Zhao, H. Jang, S. Y. Lee, J. M. Kim, K. S. Kim, J.-H. Ahn, P. Kim, J.-Y. Choi, B. H. Hong, *Nature* **457**, 706 (2009).
- [28] X. Li, W. Cai, J. An, S. Kim, J. Nah, D. Yang, R. Piner, A. Velamakanni, I. Jung, E. Tutuc, S. K. Banerjee, L. Colombo, R. S. Ruoff, Large-Area Synthesis of High-Quality and Uniform Graphene Films on Copper Foils, *Science* **324**, 1312 (2009).
- [29] S. Bae, H. Kim, Y. Lee, X. Xu, J.-S. Park, Y. Zheng, J. Balakrishnan, T. Lei, H. R. Kim, Y. I. Song, Y.-J. Kim, K. S. Kim, B. Ozyilmaz, J.-H. Ahn, B. H. Hong, S. Iijima, Roll-to-roll production of 30-inch graphene films for transparent electrodes, *Nat. Nanotechnol.* **5**, 574 (2010).

## Chapter 2 Experimental setup

The instrument setup to characterize polymer photovoltaic device and the experimental details were described. Standard solar measurement system was used to investigate the basic device characteristics. We further used external quantum efficiency and transient photovoltage measurement to analyze the spectral response and recombination dynamics of the device. The optical and electrical properties of transparent conducting films were characterized by UV-visible spectroscopy, 4-point probes measurement, Raman spectroscopy and Hall effect measurement. The surface morphology and potential were measured by atomic force microscopy (AFM) and Kelvin probe microscopy (KFM) techniques respectively.



## 2.1. Solar cell characterization

### 2.1.1. Air mass 1.5 solar spectrum

Solar radiation closely matches a black body radiator at about 5,800 K. As it passes through the atmosphere, sunlight will be attenuated by scattering and absorption; the more atmosphere through which it passes, the greater the attenuation. According to this, the unity air mass (AM) (Eq. 2.1) is used to define the different sunlight irradiance at the sea level due to different incident angle of the sunlight. (Fig 2.1)

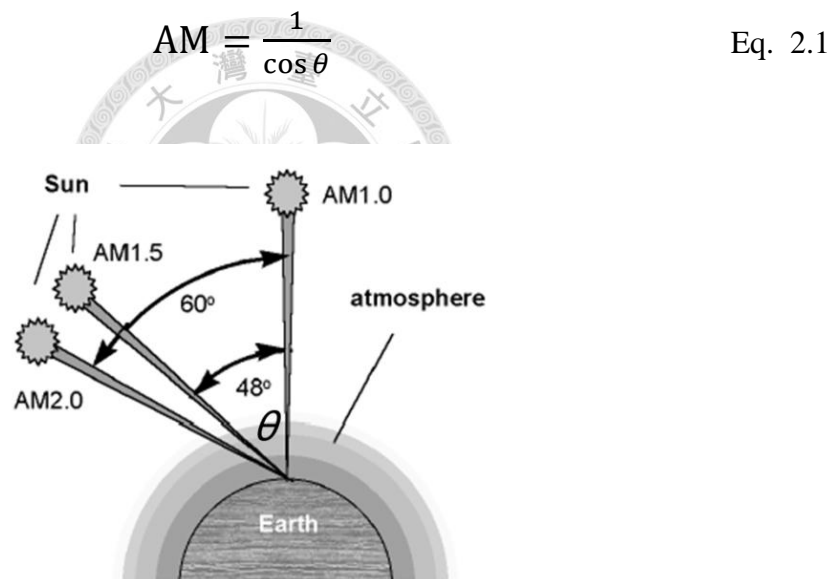


**Figure 2.1** Schematic of the path length difference of the solar irradiation through the Earth's atmosphere in units of air mass (AM).

Hence, when the sun is 48 degrees off overhead, the radiation is AM1.5, which is the preferred standard spectrum for solar cell efficiency measurements in literature. In our experimental setup, we use Newport-Oriel solar simulator (300W) to simulate AM1.5 sunlight spectra, with total irradiation density of  $100\text{mW}/\text{cm}^2$ . And all the

current-voltage characteristics of photovoltaic devices were recorded by Keithley 2410 source meter.

### 2.1.2. External quantum efficiency

The quantum efficiency of a solar cell is a very important measurement for solar cells as it gives information on the current that a given cell will produce when illuminated by a particular wavelength. In polymer solar cells, one often measures the external quantum efficiency (EQE), which is the current obtained outside the device per incoming photon. In the study, we used oriel 500W Xe-Hg light source, and used thermal oriel cornerstone 1/4 monochromator to divide the white light into specific wavelength. The measured spectral range is from 300-800 nm. Optical power is calibrated by silicon diode. Figure 2.2 shows the instrument setup.

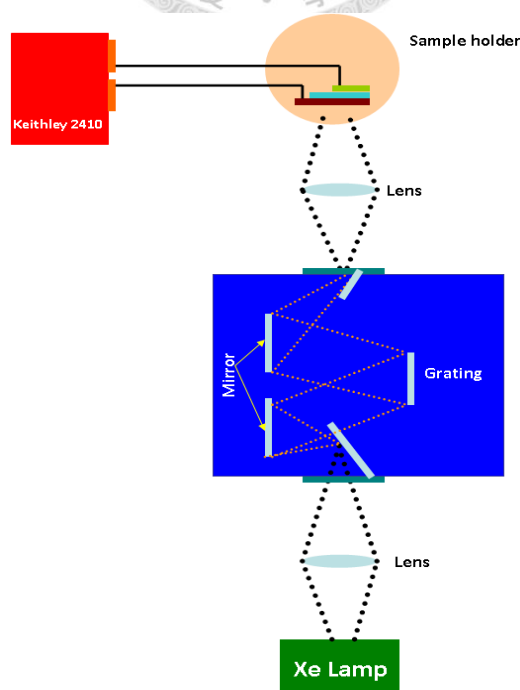
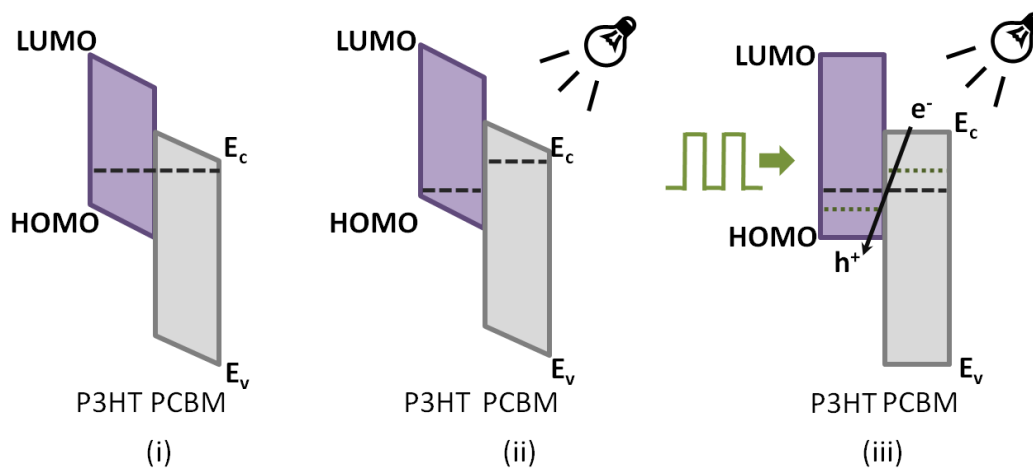


**Figure 2.2** External quantum efficiency (EQE) system setup.



### 2.1.3. Transient photovoltage (TPV)

In order to quantify the carrier recombination in organic photovoltaic devices, the transient photovoltage system was setup. In transient photovoltage measurement, the device was first held at a steady state open circuit voltage, which magnitude was adjusted by varying the intensity of a bias lamp. Then, we induced a pulsed light (frequency-double Nd:YAG pulsed laser ( $\lambda=532nm$ , repetition rate 10Hz, a duration~ 5 ns)) to generate a small perturbation to the open circuit voltage due to the transiently generated electron and hole carriers altering the quasi Fermi levels. At open circuit voltage, these additional carriers decay with the lifetime determined by the rate of charge carrier recombining across the heterojunction interface. At last the transient decay signals were recorded by a digital oscilloscope (Tetronix TDS5052B). The setup schematics were shown in Figure 2.3. A typical photovoltage transient curve is shown in Figure 2.4. The decay curve can be fitted to a monoexponential decay, from which a characteristics lifetime  $\tau$  can be extracted. The effective recombination rate,  $K_{rec}$  is proportional to  $1/\tau$ .



Energy band diagram of donor and acceptor under  
 (i). Dark,  
 (ii). Illumination of bias lamp,  
 (iii). Illumination of bias lamp and pulse light, and applied open circuit voltage.

**Figure 2.3** Schematic of a band diagram in transient photovoltage setup

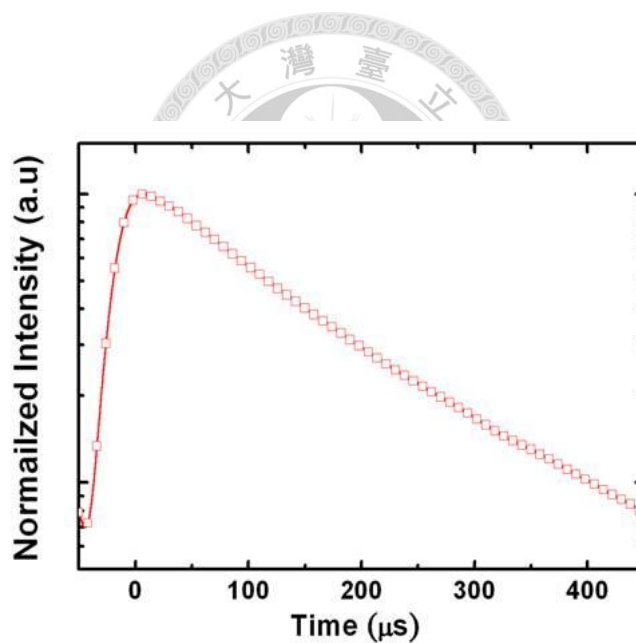


**Figure 2.4** A typical transient photovoltage decay curve.

## 2.2. Transparent conducting electrode characterization

### 2.2.1. UV-visible spectroscopy

UV-Visible spectra were obtained using Jasco V750 UV/Vis/NIR spectrophotometer. To measure the transmission spectra of transparent conducting films, we attached the films on the pre-cleaned 1.5x3cm glass substrates, and used another blank glass substrate as the reference. Spectra data were record in the range of 300-800nm, and the interval of each data point was 2nm.

### 2.2.2. Sheet resistance measurement

Sheet resistance is applicable to two-dimensional systems where the thin film is considered to be a two-dimensional entity. The sheet resistance can be simply derived from the resistivity of 3D system only grouping the thickness with the resistivity. We can use the following Eq. 2.2 and fig.2.5 to express,

$$R = \rho \frac{L}{A} = \rho \frac{L}{Wt} = \frac{\rho}{t} \frac{L}{W} = R_s \frac{L}{W} \quad \text{Eq. 2.2}$$

where  $\rho$  is the resistivity,  $A$  is the cross-sectional area,  $L$  is the length,  $W$  is the width,  $t$  is the sheet thickness and  $R_s$  is the sheet resistance. The common unit of sheet resistance is "ohms per square" (denoted " $\Omega/\text{sq}$ " or " $\Omega/\square$ "), which is dimensionally equal to an ohm, but is exclusively used for sheet resistance.

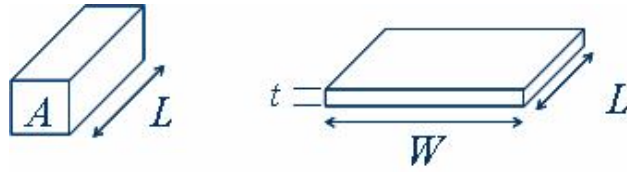


**Figure 2.5** Geometry for defining resistivity (left) and sheet resistance (right).

Practically, we use 4-point probe measurement (QUATEK / QTI-QT-50) to avoid the contact resistance while measuring the sheet resistance. After getting the measured resistance from Keithley 2410 source meter, we can figure out the sheet resistance by

Eq. 2.2.

$$R_s = \frac{\pi R}{\ln 2} \quad \text{Eq.2.2}$$



### 2.3. Raman spectroscopy

Raman spectroscopy is a powerful technique for understanding molecular composition and structure of materials. The technique measures the wavelength and intensity of inelastic scattered light from the light from sample to obtain information about the rotational and vibrational modes of the material. Typically we use monochromatic light source to excite the molecule from the ground state to a virtual energy state. And when the molecule relaxes it emits a photon and it returns to a different rotational or vibrational state. The difference in energy between the original state and this new state leads to a shift in the emitted photon's frequency away from the excitation wavelength. If the emitted photon is less energetic than the incident photon, the resulted shift toward to lower frequency is designated as a Stokes shift. Inversely, if the emitted photon is more energetic than the incident photon, the resulted shift toward to higher frequency is designated as an Anti-Stokes shift. Figure 2.6 shows the related states of Raman signal in the energy level diagram.

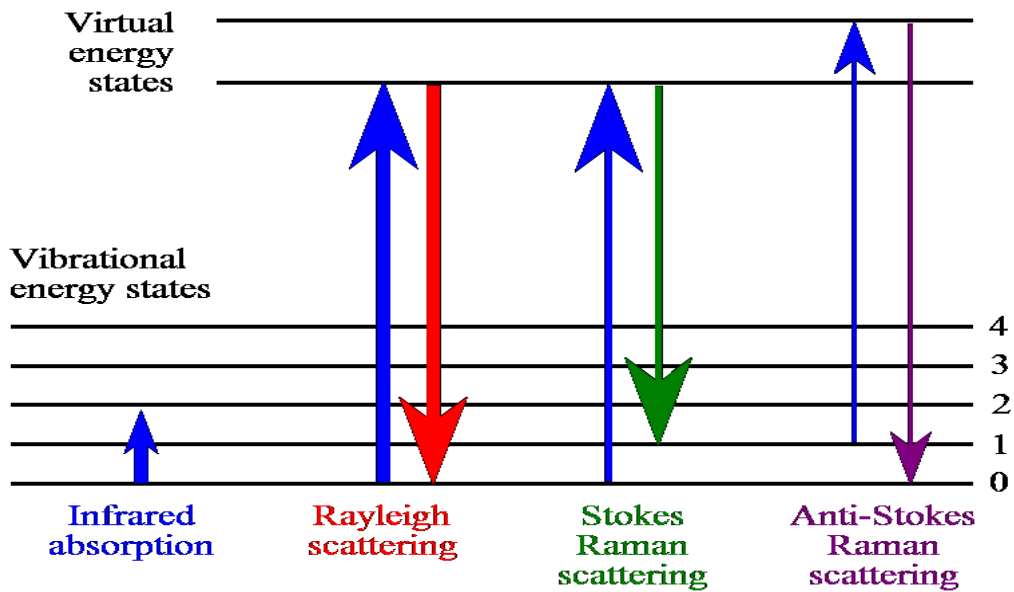


**Figure 2.6** Schematic of energy level diagram related to Raman scattering.  
([http://en.wikipedia.org/wiki/Raman\\_spectroscopy](http://en.wikipedia.org/wiki/Raman_spectroscopy))

In our Raman system setup, we use 632.8nm He-Ne laser as the monochromatic light source, and use the confocal microscope system to focus the laser spot. The spot size was  $2\ \mu\text{m}$ . Raman signals were recorded by using HORIBA iHR550 spectrometer and Symphony CCD detectors. The sample/materials for Raman spectroscopy were deposited on 300nm  $\text{SiO}_2/\text{Si}$  wafer, for obtaining the best signal strength and signal to noise ratio.

## 2.4. Surface morphology and surface potential measurement

### 2.4.1. Atomic force microscopy (AFM)

The atomic force microscopy (AFM) is one kind of scanning probe microscopy that provides high resolution topographical images of materials. It can have a spatial resolution of down to sub-nanometers. To produce surface images, it relies on forces between the AFM tip and the sample and scans line-by-line over a rectangular area with typically few hundred lines using a sharp tip. The sharpness of the AFM tip directly affects the image resolution and typically has a radius of curvature from few to ten nanometers. When the tip is brought within close proximity of the sample surface, the force between the tip and sample cause the cantilever to deflect. Changes in surface topography and material result in changes in the cantilever deflection which is measured by reflecting laser beam onto a photodetector. A piezoelectric scanner moves the sample underneath the tip, providing surface topography in x, y, and z-directions. Figure 2.7 shows the schematic of the AFM system. Since large changes in surface height could result in the collision of the tip and the sample surface, the AFM relies on a feedback loop and the piezoelectric scanner to maintain a constant force on the cantilever. There are two common modes of AFM, contact mode and tapping mode. In contact mode, the AFM tip is brought to directly contact with the sample surface and a constant deflection is maintained by moving of the piezoelectric scanner based on the feedback signal.

However, due to the direct contact to sample surface with a pressure, the contact mode is generally not good choice for soft organic materials. In tapping mode, the AFM tip is oscillated above the sample surface. Through the feedback loop, constant frequency, amplitude and phase of the cantilever are maintained. Changes in topography affect the interaction between the tip and sample and, therefore, the phase and amplitude of the cantilever oscillation changes. Through changes brought by feedback loop, the information about the sample can be obtained. The AFM images in the thesis were all scanned by Veeco Innova Scanning Probe Microscope.

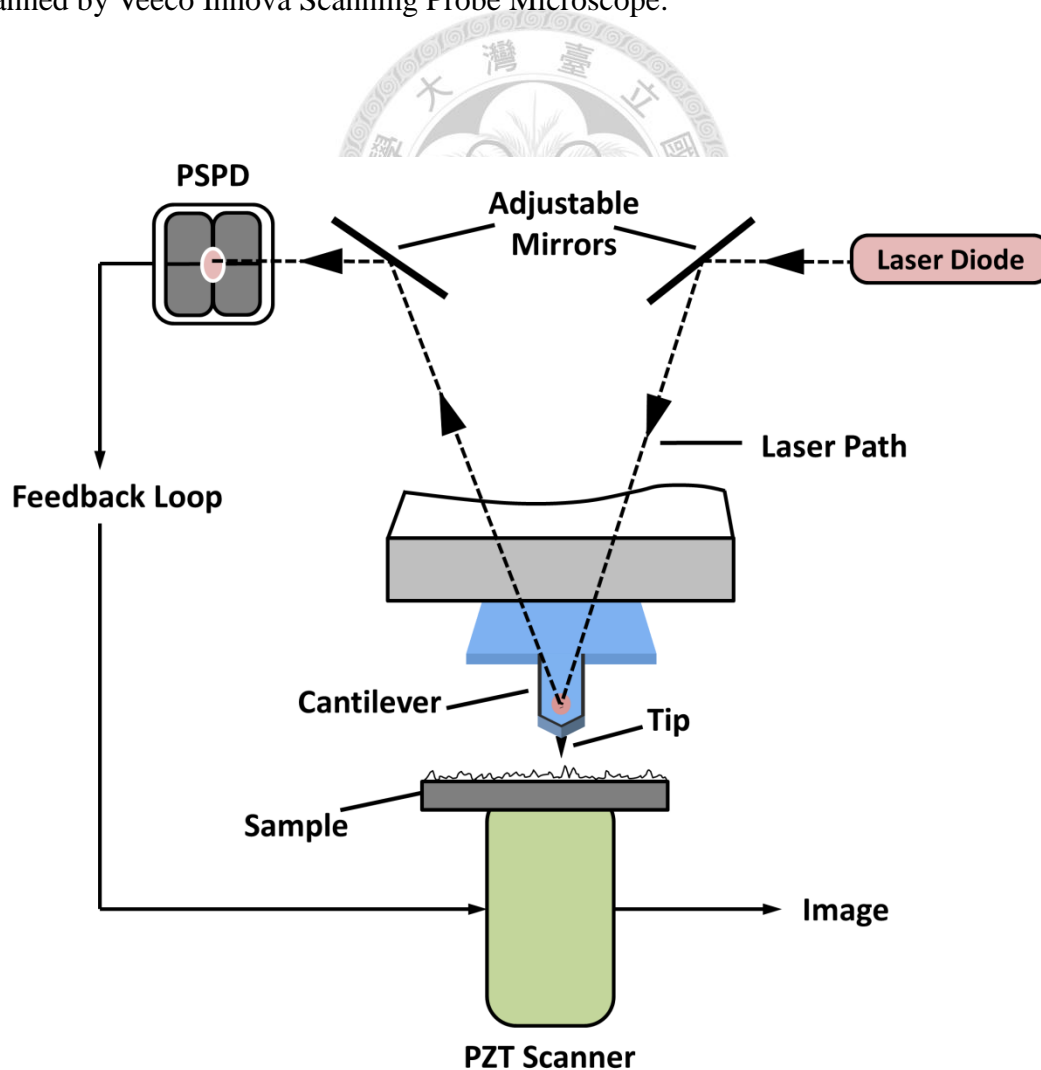


**Figure 2.7** The schematic of basic components in AFM system.



### 2.4.2. Kevin probe force microscopy (KPFM)

Kevin probe force microscopy is one of the imaging modes derived from AFM, providing the surface potential images of our sample. Different from tapping mode, which scan the surface topography forward and backward, the KPFM scan the topography in forward but lift a height and keep a constant distance with the surface in the backward. While the tip is moving backward, an AC voltage bias was applied on the conducting tip with the frequency which is synchronized with tip oscillation frequency. If there is a workfunction difference between the sample surface and the tip, the resulted electrostatic force will affect the oscillation of the tip. And as the same in tapping mode, through the changes brought by feedback loop, the information about the sample can be obtained. Figure 2.8 shows the schematic of KPFM.

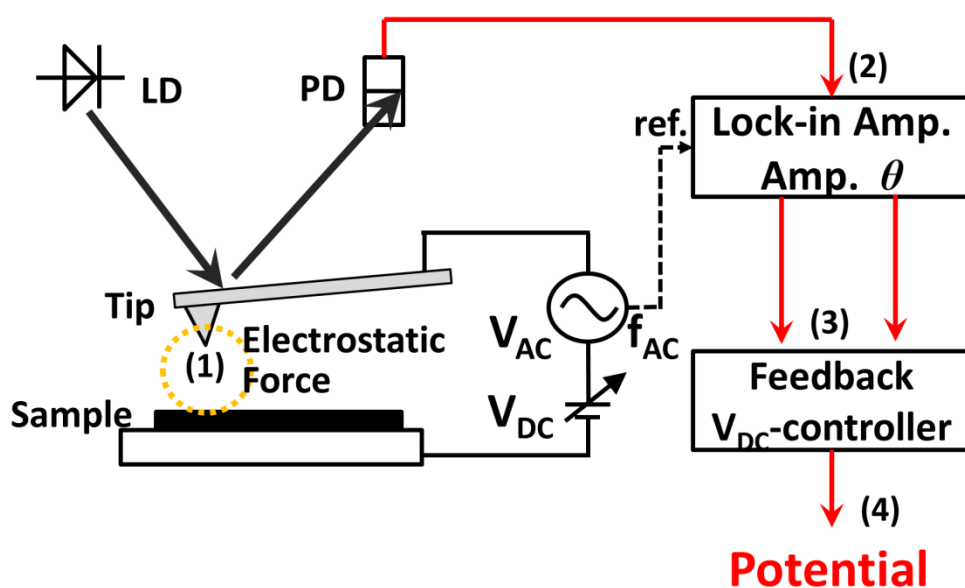
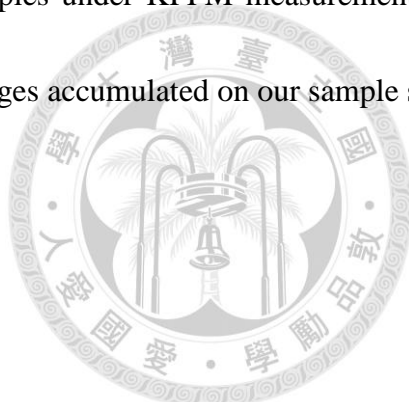


**Figure 2.8** Schematic of Kevin probe force microscopy.

Generally, the value we measured is the surface potential of the sample. To figure out the workfunction, we will first measure the HOPG as our criterion, since its workfunction is stably lying at 4.6eV. Then after compare the surface potential difference between HOPG and our sample, we can determine the workfunction of our sample. For example, typically the average surface potential of HOPG is about 260 mV. If the surface potential of our sample is 460 mV, the workfunction of our sample is 4.4 eV. And if the surface potential of our sample is -140 mV, the workfunction of our sample is 5.0 eV. The samples under KPFM measurement are all grounded to ensure that there are not static charges accumulated on our sample surface.



## 2.5. Hall effect measurement

The Hall effect measurement, as well as the van der Pauw Method, is a technique commonly used to measure the resistivity and the Hall coefficient of a sample. Also some properties of the material can be calculated, such as doping type, the sheet carrier density of the majority carrier, and the mobility of the majority carrier. The instrument we used in the study was Van der Pauw Ecopia HMS-3000 Hall Measurement System. The sample prepared for Hall effect measurement was deposited on 300 nm SiO<sub>2</sub>/Si substrate in a square shape. Metal contacts were deposited on the corners of the square, for the purpose of contacting with the probe without destructing our sample. The schematic of the sample we prepared for Hall effect measurement is shown in figure 2.9.

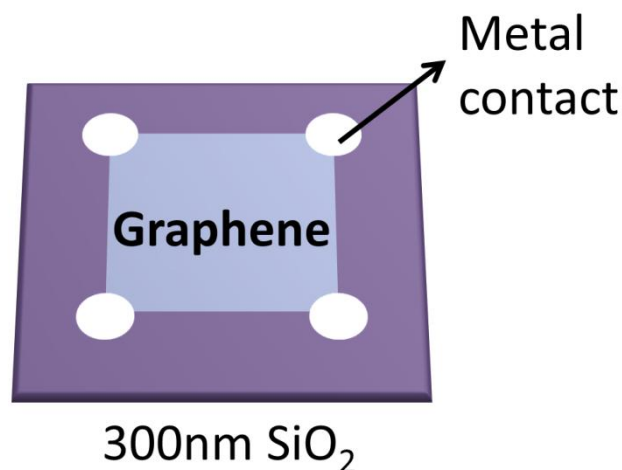


**Figure 2.9** Schematic of the sample we prepared for Hall effect measurement.

## Chapter 3

### Solution processable nanocarbon platform for polymer solar cells

#### 3.1. Introduction

Polymer solar cells have attracted a great concern for fabricating low-cost large-area mechanically flexible photovoltaic devices compared to the conventional inorganic counterparts.[1–5] Conventionally, indium tin oxide (ITO) was used as transparent and conducting hole collecting electrode in polymer solar cells. A thin and planar layer of Poly(3,4-ethylenedioxythiophene)poly(styrenesulfonate) (PEDOT:PSS) was usually coated on top of ITO and served to minimize the detrimental effects of ITO roughness as well as to align the work function. Although such a device design has achieved a very promising power conversion efficiency, there still exist several fundamental issues to be overcome by using the ITO/PEDOT:PSS as an anode electrode in the future market integration of low-cost plastic solar cells. For example, the price of ITO has increased by an order of magnitude over the last decade due to an increase in demand for liquid crystal displays (LCDs) and the scarcity of In. The lack of mechanical flexibility of ITO limits its application in the plastic organic electronics. Moreover, the interface between ITO and PEDOT:PSS is not stable since PEDOT:PSS is usually deposited from highly acidic (pH~1) aqueous suspensions that are known to corrode ITO at elevated temperatures.[6,7] Several alternatives to ITO and PEDOT:PSS

have been pursued and reported. For example, other transparent conducting oxide,[8] conducting polymer,[9,10] single walled carbon nanotube (SWNT)[11 – 18] and graphene films[19] have been demonstrated to replace ITO as a transparent conducting electrode. Transition metal oxides such  $V_2O_5$ ,  $MoO_3$ [20] and  $NiO$ [21] deposited by vacuum techniques were also found to effectively substitute PEDOT:PSS as the buffer layers in the polymer solar cells. Nevertheless, the main advantage of polymer solar cells is that devices can be fabricated at room temperature over large areas using *solution processing* or *transfer printing* onto substrates. It would be great potential to develop fully solution-processable fabrications of polymer solar cells for deposition of both electrodes and photoactive layers. In this chapter, we would like to demonstrate an architecture of polymer solar cells based on allotropes of nanocarbon materials, consisting of a transparent conducting electrode using one-dimensional (1D) single-walled carbon nanotubes (SWNTs), a hole transporting interfacial layer using two-dimensional (2D) graphene oxide (GO) and the zero-dimension (0D) fullerene derivative PCBM/P3HT bulk heterojunctions as a photoactive layer. The advantage of this polymer photovoltaic device structure is that it can be fabricated fully compatible with solution processed printable electronics based on the nanocarbon platform.

## 3.2. SWNT conducting thin film as transparent electrode

It has been demonstrated that solution processed SWNT thin films can be alternative transparent and conducting electrodes.[11 – 18] We utilized it as our bottom electrode for photovoltaic devices due to their high transparency over much of the solar spectrum, excellent electrical conductivity, and the potential for inexpensive roll-to-roll processing.

### 3.2.1. The preparation of SWNT electrode

#### The purification of single walled carbon nanotube

Raw SWNTs purchased from Unidym, Inc. were purified by reiterative low temperature oxidative annealing and acid treatment.[22] In brief, the Raw SWNTs were first annealed in air at 225°C for 24 hours to oxidize the iron catalyst particles and also reduce the amorphous carbon. The second step involved shortly sonication and stirring the SWNTs in 6M to 12M hydrochloric acid (HCl) at approximately 80°C for 12 hours. The purpose of this step was removing the oxidized iron particles by reacting it with HCl solutions. Then the third step was filtered the SWNTs out by using 1µm PTFE filter paper and rinsed it with deionized (DI) water several times. By repeating the process 3 to 4 times, each time raising the annealing temperature 25°C, we could get the purified SWNTs to fabricate the transparent conducting electrode. Figure 3.1 shows the raman spectra of raw and purified SWNTs.

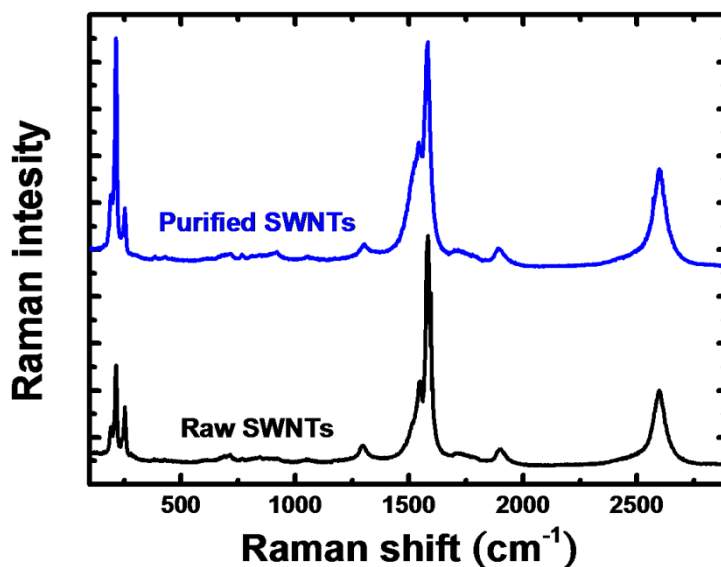


**Figure 3.1** Raman spectra of raw and purified SWNTs.

#### **The fabrication of SWNT thin films**

Aqueous solution of 1wt% sodium dodecyl sulfate (SDS) was used to disperse SWNTs at the concentration of 0.04mg/ml. The SWNT thin film was then deposited on glass using the vacuum filtration and transfer method previously reported by Wu et al.[11] First, the SWNTs were filtrate out on methylcellulose ester (MCE) membrane and rinsed with DI water to remove the surfactant SDS. Second, the SWNT thin film on the membrane was cut into strips and pressed to attach on the glass substrate. And after dissolving the MCE membrane by acetone, we could get the SWNT conducting thin film as the electrode on the glass substrate. Figure 3.2 shows the schematics of the procedures. Here we especially used the membrane with 25nm pore size rather than conventionally used 200nm in order to obtain more smooth and uniform SWNT thin films. To reduce the sheet resistance, further functionalization was carried out by

soaking samples in  $\text{HNO}_3$  (16M) 1 hour, air dried after removed from the acid bath, and followed by rinsing with DI water as well as dried with gentle nitrogen flow.

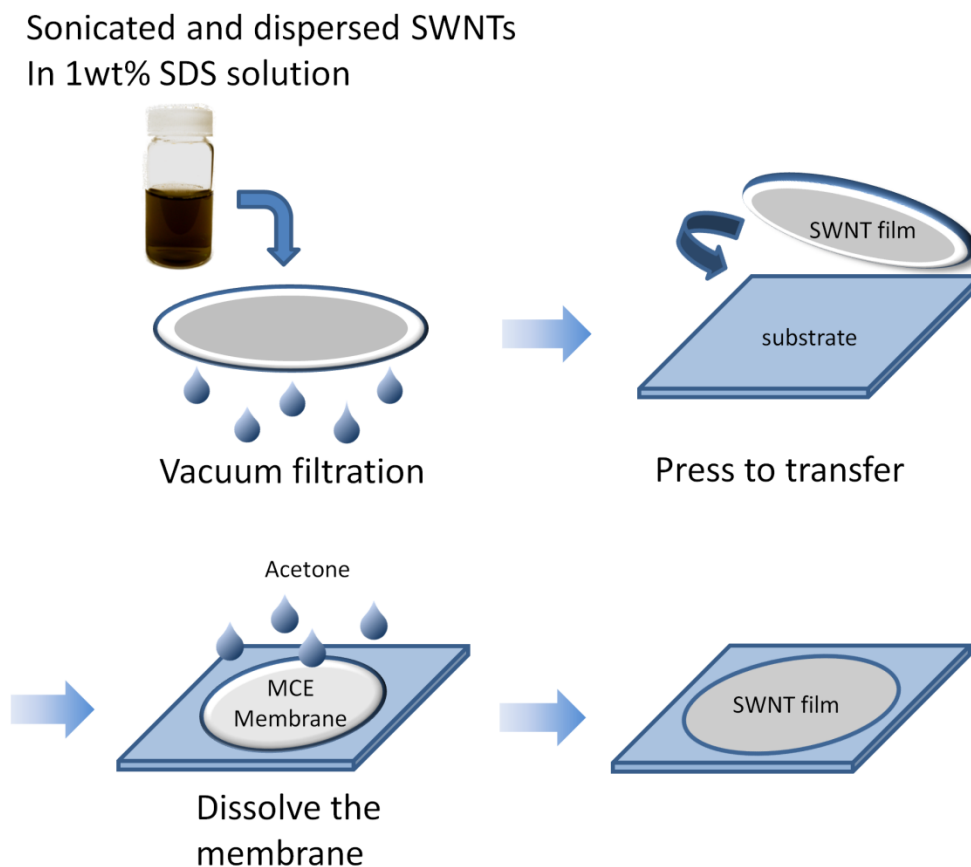


**Figure 3.2** The schematic of fabricating the SWNT thin film electrode.

### 3.2.2. Characterization of SWNT electrode

By employing the vacuum filtration method, we can control the filtration volume to make the SWNT thin film electrodes with different transparencies and sheet resistances. Figure 3.3 shows the transmission spectra of SWNT thin film fabricated by different filtration volume of SWNTs suspensions, ranging from 0.5ml to 3ml. And the inset photograph was the transferred SWNT thin film on the glass substrate. These SWNT electrode were then soaked in  $\text{HNO}_3$  to further reduce the sheet resistance by



removing residual surfactant and also introducing carboxyl groups on the SWNTs to give a p-type doping.[13,17] Figure 3.4 plots the transmittance at 550 nm of SWNT thin films as a function of their sheet resistance before and after nitric acid treatment. A sheet resistance value as low as  $100 \Omega/\square$  can be obtained at a transmittance of  $\sim 75\%$  for the SWNT electrode after treatment.

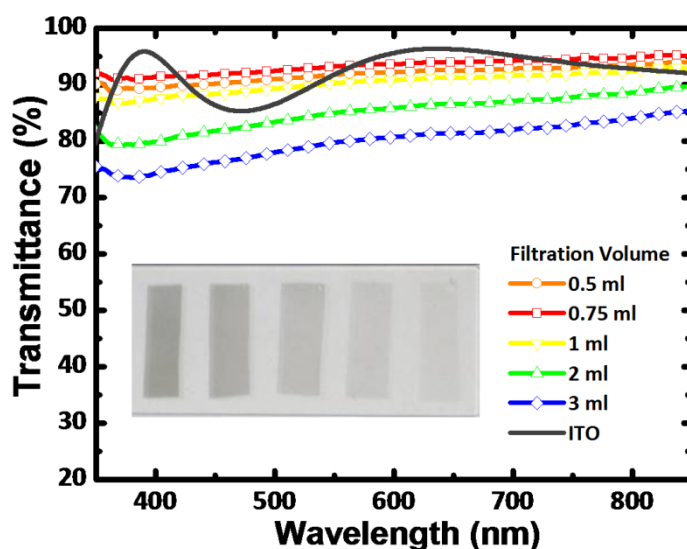


**Figure 3.3** The transmission spectra of SWNT thin film with different filtration volume. (Inset) The photograph of transferred SWNT thin film on the glass substrate.

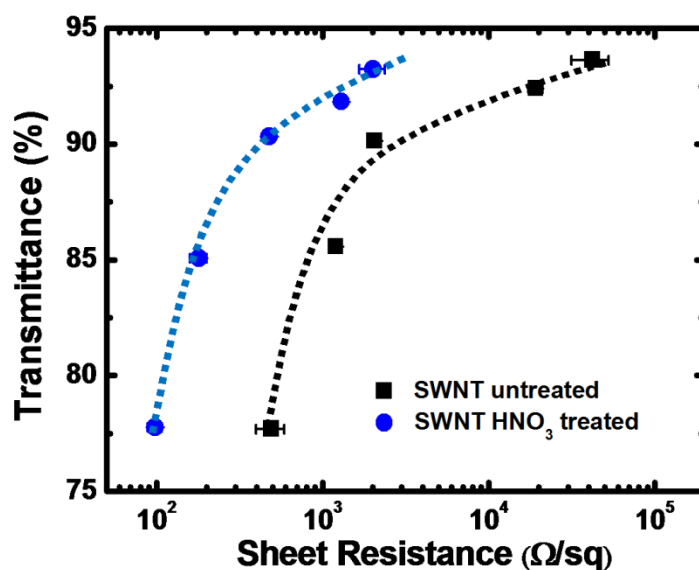


**Figure 3.4** The transmittance@550nm versus sheet resistance of SWNT electrode.

To attain the best performance of our OPV devices, we selected the SWNT electrode existing the lowest resistance, which is the  $\text{HNO}_3$  treated SWNT thin film with 75% transparency. The macro- and microscopic appearances of the SWNT electrode is displayed by figure 3.5(a)(c), which also shows the capability of fabricating large-area, highly flexible electrode to apply on the OPVs.(fig. 3.5(b)(d))

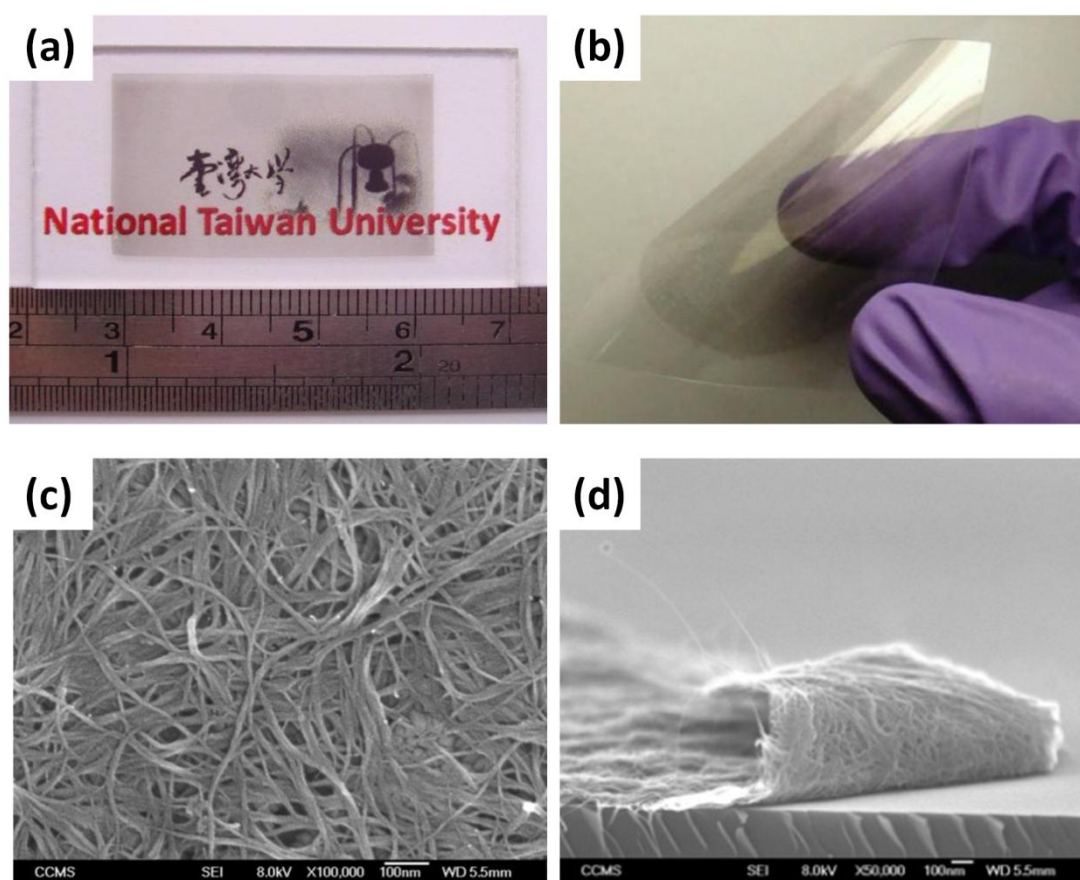


**Figure 3.5** (a) Large-area SWNT thin film on glass substrate. (b) Flexible SWNT thin film on PET substrate. (c) The planar view of SWNT thin film under scanning electron microscopy (SEM). (d) The SEM cross section of SWNT thin film, which shows the extremely high flexibility of SWNT thin film.

### 3.3. Graphene oxide as hole transport layer in OPVs

Graphene oxide (GO) is a graphene sheet functionalized with oxygen functional groups in the form of epoxy and hydroxyl groups attached on the basal plane or decorated at the edges.[23–25] GO thus contains a large fraction of  $sp^3$  hybridized carbon atoms bound to oxygen which makes it an insulator (sheet resistance  $\sim 10^9 \Omega/\square$ ) with a large band gap.[26] Recently, the incorporation of graphene oxide (GO) deposited from neutral solution was found to be a good candidate of hole transport layer.[27] Therefore, we employed GO layer rather than PEDOT:PSS as our hole transporting anode interfacial layer in our following devices. Figure 3.6 shows the device structure and device performance of using GO as the hole transport layer in P3HT:PCBM polymer solar cell.

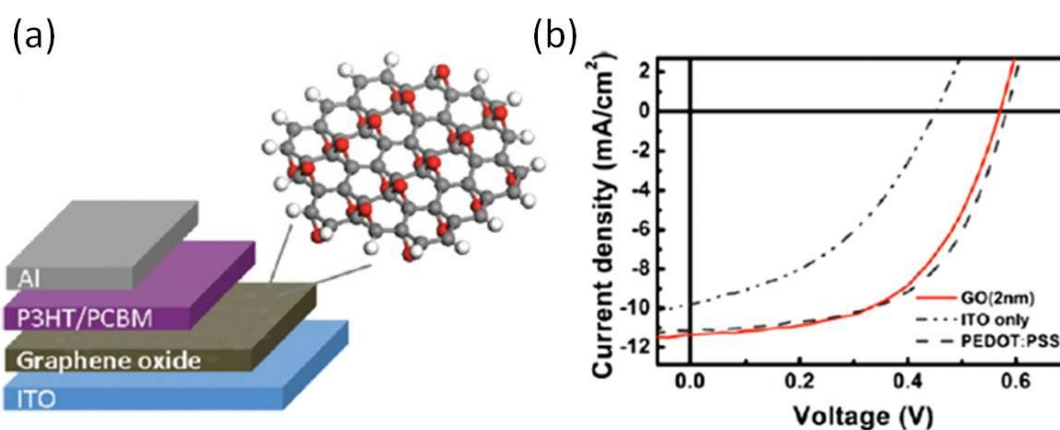


**Figure 3.6** (a) Schematic device structure of using GO as hole transport layer in conventional P3HT:PCBM polymer solar cell. (b) Current-voltage characteristics of photovoltaic devices with no hole transport layer (labeled with ITO), with 30nm PEDOT:PSS and with 1 layer GO as hole transport layer.

### 3.3.1. The preparation of graphene oxide

GO was obtained from purified natural graphite powder (SP-1, Bay Carbon) using the modified Hummers method.[28] At first, 2 g graphite powder and 1.5 g  $\text{NaNO}_3$  were placed in a flask. Then 70 ml of  $\text{H}_2\text{SO}_4$  (98%) was added and the mixture was stirred by a stirring magnet as well as cooled in an ice water bath. Nine grams of  $\text{KMnO}_4$  (99%) was gradually added over 1 hour. Cooling was completed in 2 hours and then keeping the mixture with gentle stirring under room temperature for 5 days. During these days, the mixture would become a highly viscous liquid with the color changing from dark green to dark brown. Five days later, the liquid was gradually added to 200 ml by 5 wt%  $\text{H}_2\text{SO}_4$  aqueous solution over about 1 hour with stirring, and the resultant mixture was further stirred 2 hours. Then, 9 ml  $\text{H}_2\text{O}_2$  (35 wt% aqueous solution) was added to the mixture and the mixture was stirred for 1 hours.

To remove the ions of oxidant origin and get GO, the mixture was further purified by the following procedure cycle 15 times: centrifugation, removal of the supernatant liquid, adding mixed aqueous solution of 3 wt%  $\text{H}_2\text{SO}_4$ /0.5 wt%  $\text{H}_2\text{O}_2$  and shaking to re-disperse. After that, we repeated the procedures 3 times more while changing the mixed aqueous solution into DI water. Well dispersed GO solution with the concentration of 2mg/ml in DI water was prepared for deposition of GO thin films.

Figure 3.7 is the flow chart of the procedures to make GO solution.

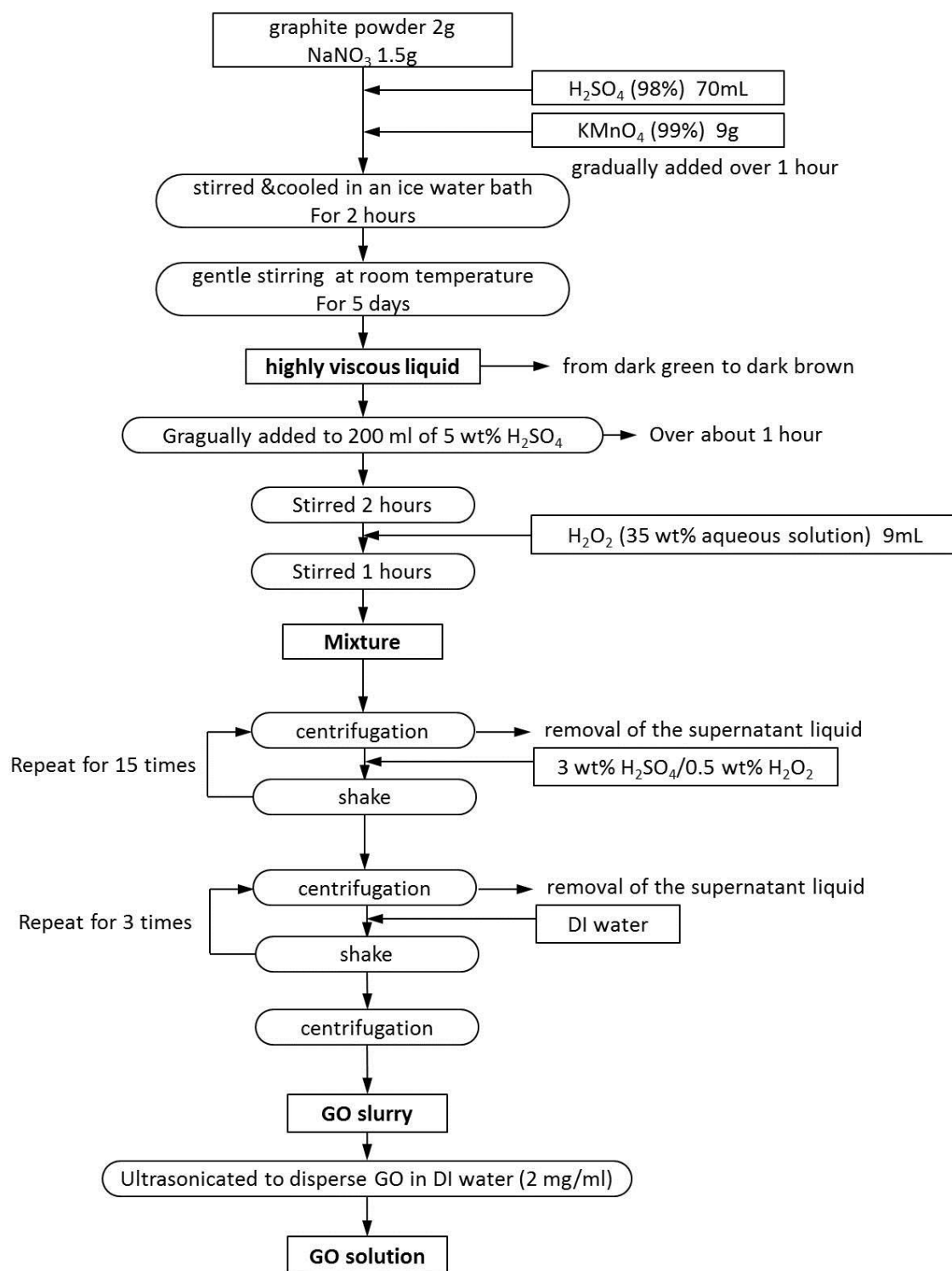


**Figure 3.7** The flow chart of synthesizing GO and making GO solution. The long circle means the action we taken and the rectangle means the substances we used or obtained.

### 3.3.2. Characterization of graphene oxide

Some optoelectronic properties of GO, such as photoluminance and transport behaviors, has already reported by our and the other groups.[29–33] In here, the typical transmission electron microscopy (TEM) and diffraction results are shown to confirm the structure of GO sheets in as-prepared suspensions. Figure 3.8 (a)(b) are the TEM image of a GO sheet on a lacey carbon support and the corresponding selected area electron diffraction pattern (SAED). The 6-fold symmetry in the diffraction pattern is consistent with the hexagonal structure, and the relative intensity of the inner  $1\bar{1}00$ -type and outer  $2\bar{1}\bar{1}0$ -type reflections shown in Figure 3.8 (c). These intensity are consistent with that of a monolayer.[34]

We also use the atomic force microscopy (AFM) to obtain the surface morphology of GO sheets. The lateral dimensions of GO flakes are ranged from 1–5  $\mu\text{m}$  and the height was measured to be about 1 nm, which corresponds to an atom-layer thickness of a single GO sheet. Figure 3.9 shows a single GO sheet deposited on flat silicon substrate from GO aqueous solution.

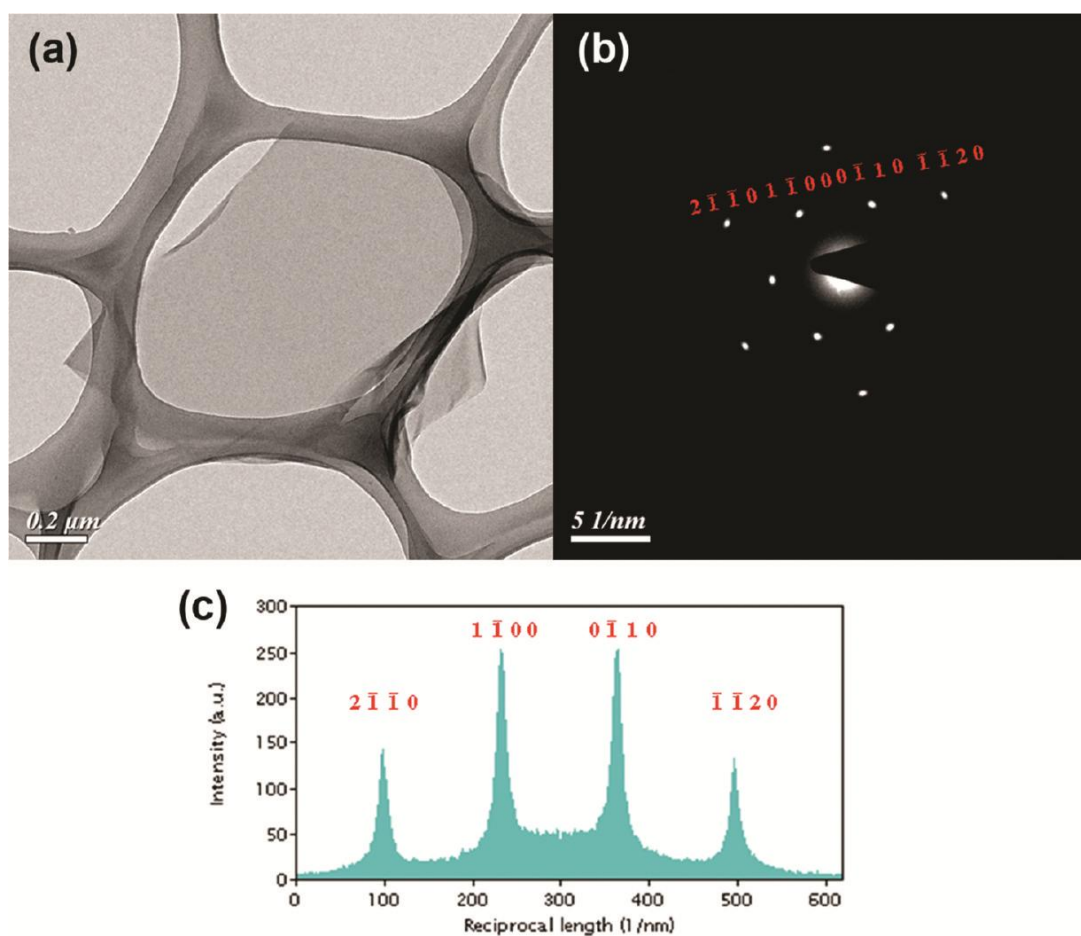


**Figure 3.8** (a) TEM image of as-prepared GO sheet on a lacey carbon support. (b) SAED pattern; the diffraction spots are labeled with Miller Bravais indices. (c) Relative intensity profile obtained from the diffraction pattern in (b).

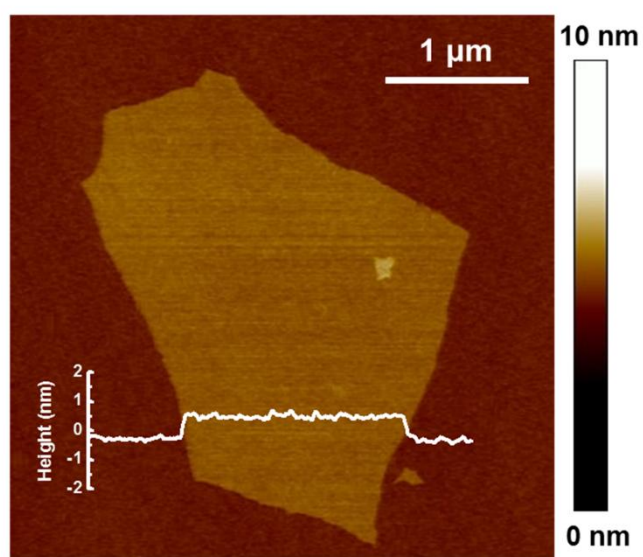


**Figure 3.9** The AFM height image of a GO sheet on Si substrate and the corresponding height profile.

To find out the energy level of GO in the energy band diagram, we were first trying to figure out the band gap of GO. However, the heterogeneous  $sp^2/sp^3$  structure of GO makes it difficult to assign a specific energy for the band gap. Since conduction in GO and reduced GO occurs via tunneling between  $sp^2$  sites,[33] the band gap represents potential barriers for transport formed by covalent  $sp^3$  bonds. That is, in as-synthesized GO, the  $sp^3$  fraction can be as high as 60% so that the  $sp^2$  domains are non-percolating, which prevents conduction.[33] To obtain information about the  $sp^3$  potential barriers, the optical gap of GO can be obtained from the Tauc plot[37] using the following relation,

$$\alpha h\nu \propto (h\nu - E_g)^{1/2} \quad \text{Eq3.1}$$

where  $\alpha$  is the absorption coefficient and  $h\nu$  is the photon energy, and  $E_g$  is the optical gap. The Tauc plot for GO solution shown in the inset of figure 3.10 indicates that  $E_g$  is ~3.6 eV.

Since GO is very insulating with a wide band gap, we have further employed the photoionization measurement (Riken AC-2) to determine the highest occupied molecular orbital (HOMO) of GO. Figure 3.11 shows the HOMO level of GO is fitted to ~5.2 eV, which is only ~0.2 eV below the HOMO level of P3HT lying at 5.0 eV. And also considering with the band gap, we can figure out the lowest unoccupied molecular orbital (LUMO) of GO is ~1.6eV. This LUMO level of GO hinders the possibility for



electrons from the LUMO levels of P3HT or PCBM to be collected at the anode. With these electron blocking and hole transporting properties, GO has shown the potential to serve as the hole transport layer in polymer solar cells.

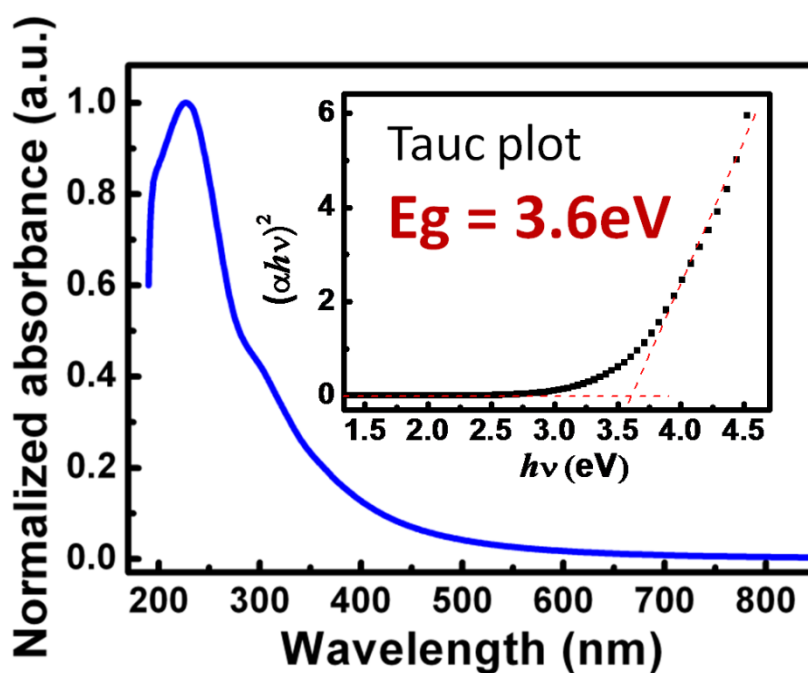


Figure 3.10 The Tauc plot measurement obtained from the absorption spectrum of GO.

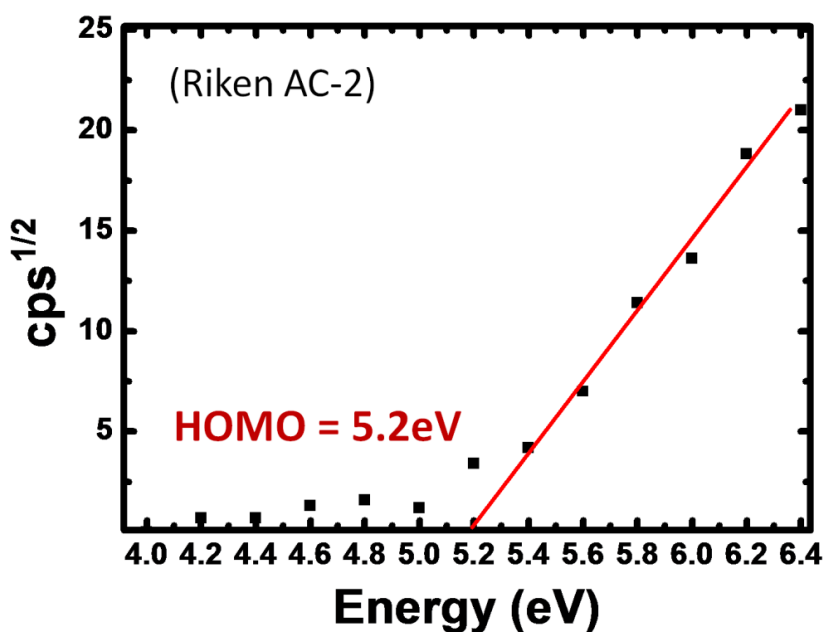


Figure 3.11 The HOMO level of GO determined by Riken Keiki AC-2 photoionization measurement.

### 3.4. P3HT:PCBM polymer solar cell on the SWNT/GO nanocarbon platform

In P3HT:PCBM polymer solar cell, conventionally we use ITO as the anode and PEDOT:PSS as the hole transport layer. However, there are some shortcomings of ITO and PEDOT:PSS. Here we proposed to use nanocarbon based SWNT/GO platform to substitute ITO/PEDOT:PSS. To have the best performance, we have using GO thin films with different thickness and different extent of reduction as the hole transporting interfacial layer in the following device fabrications.

#### 3.4.1. Experimental details

To fabricate the SWNT/GO anode, the GO aqueous solution (2mg/ml) was spin coated onto SWNT thin films at the speed of 2000 rpm for 1 layer. By controlling the times of spin coating, we are able to obtain GO layers with different thicknesses. The AFM image of 1 layer, 3 layers, and 6 layers GO thin films on the atomically flat silicon substrate are shown in figure 3.12(a)–(c). Figure 3.13 shows the dependence of the GO thin film thickness as a function of different number of layers. The average thickness of each layer of GO thin films is found to be slightly larger than that of an individual GO flake as shown in figure 3.9 due to possible stacking between different GO flakes in the thin films by spin coating. To obtain r-GO with different extent of reduction, the samples with 1 layer GO were exposed to hydrazine vapor at room temperature for 3mins, 1hr, and 4hrs respectively.

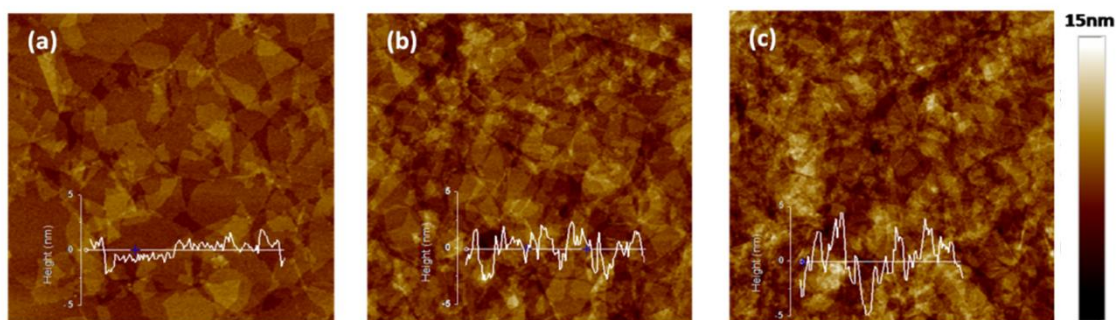


**Figure 3.12** (a) 1 layer, (b) 3 layers, (c) 6 layers GO thin films deposited on flat silicon substrates.

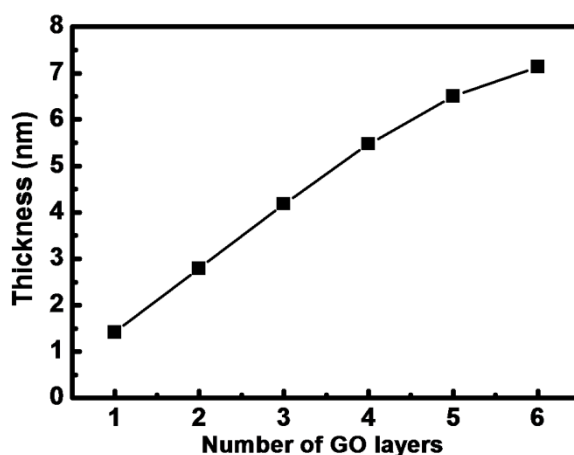


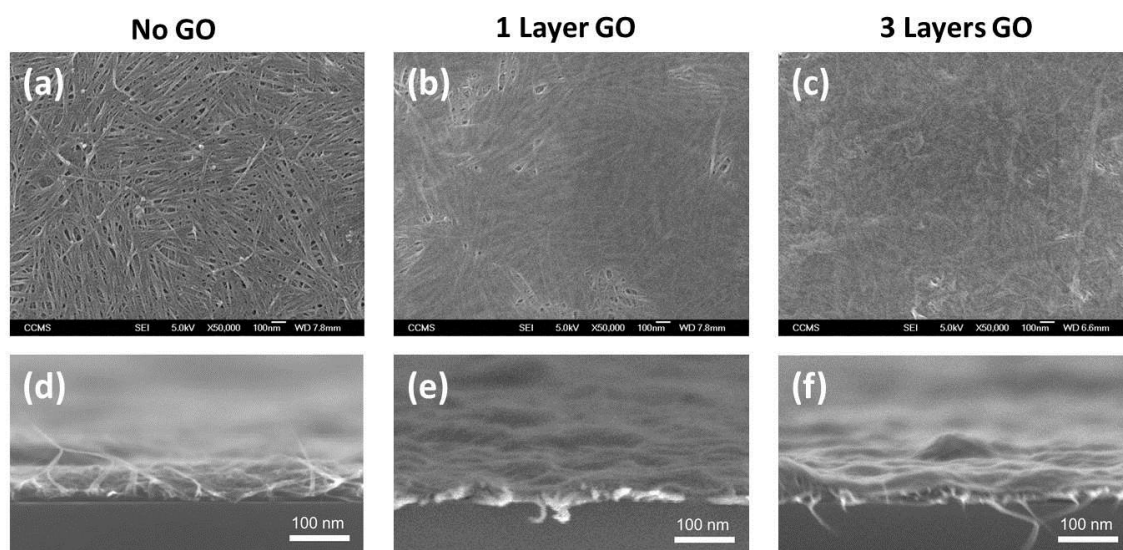
**Figure 3.13** Dependence of the GO thin film thickness as a function of different number of layers.

For the fabrication of P3HT:PCBM devices (area = 0.1 cm<sup>2</sup>), the SWNT/GO thin films were moved into a nitrogen-purged glove box for deposition of the photoactive layers and top electrodes. The photoactive layers were deposited on top of the GO (or r-GO) thin films by spin coating using a 1:0.8 weight ratio blend of P3HT:PCBM dissolved in chlorobenzene. The film thickness of the photoactive layer was about 160 nm. Al cathodes were then deposited onto the blend layers by thermal evaporation at a pressure of  $4 \times 10^{-6}$  Torr. After deposition of Al cathodes, all devices were thermally annealed at 150°C for 5 minutes in the nitrogen glove box.

### 3.4.2. Characterization of SWNT/GO platform

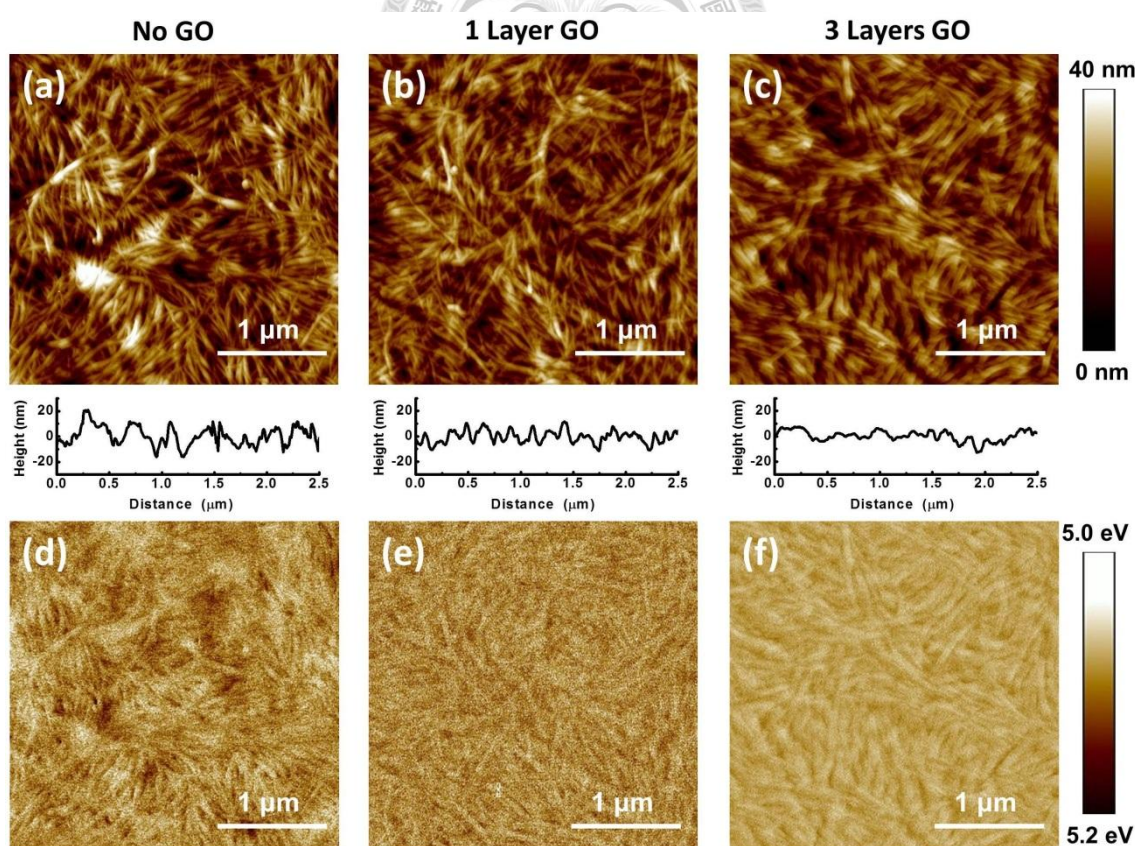
The topography and local work function mapping images of the SWNT electrodes without and with different layers of GO thin films were further revealed by AFM, scanning electron microscope (SEM), and Kelvin probe force microscope (KPFM).

Figure 3.14 (a)–(f) show the planar view and cross section SEM image of GO layers on the SWNT electrode. From SEM image, we can found that the morphology of a membrane-transferred SWNT electrode displayed a nonuniform height due to its porosity. And there were some protrusion of SWNTs, which protrusion may easily protrude into the active layer and then possibly result in the shorting of the device or a low shunt resistance.[35] Nevertheless, by deposition of GO thin films, we can not only use GO as a hole transporting anode interfacial layer but also reduce the protrusion and assist the planarization of the SWNT electrodes.(Fig. 3.14(e)(f))



**Figure 3.14** SEM planar view of SWNT electrode with (a) none, (b) 1 layer and (c) 3 layers GO thin film. (d)–(f) The corresponding SEM cross section images.

Figure 3.15 are the AFM and the corresponding KPFM images of SWNT electrodes without and with different layers GO thin films. The root-mean-square (rms) roughness of the pristine SWNT electrode was about 5.77 nm while several spots with height larger than 40 nm can be clearly seen (Figure 3.15(a)). A decreasing roughness of the SWNT electrodes after depositing the GO thin layers was clearly observed. The rms roughness for the SWNT electrodes with 1 layer and 3 layers of GO thin films were 4.20 nm and 3.94 nm respectively. And the average work function values of the SWNT/GO anode measured by KPFM were found to slightly decrease from 5.09 eV for the SWNT electrode to 5.08, 5.05 eV after depositing 1 and 3 layers of GO thin films.



**Figure 3.15** AFM height image of SWNT electrode with (a) none, (b) 1 layer and (c) 3 layers GO thin film. (d)–(f) The corresponding KPFM images.

### 3.4.3. Solar cell device characteristics

The cross sectional transmission electron microscope (TEM) image of the nanocarbon based polymer solar cell device is shown in figure 3.16. Using 0D to 2D nanocarbon materials, the device consisted of 50nm SWNT electrode, 1nm GO anode interfacial layer, 160nm P3HT:PCBM photoactive layer, and 100nm thermal evaporated Al electrode. The relevant energetics of each component in the nanocarbon based polymer solar cell device are shown in Figure 3.17.

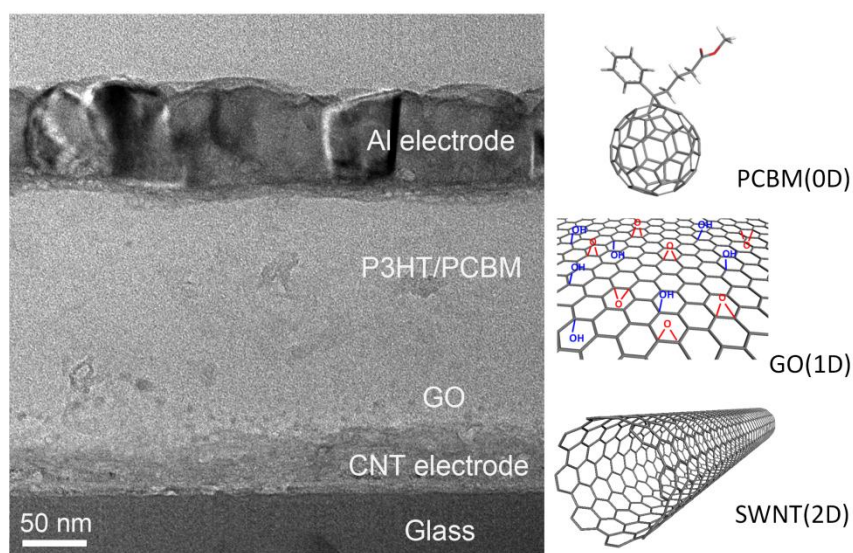


**Figure 3.16** The cross sectional TEM image of the nanocarbon based polymer solar cell of SWNT/GO/P3HT:PCBM/Al.

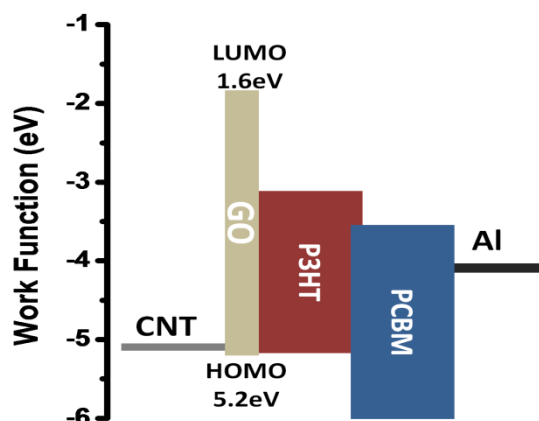


**Figure 3.17** The relevant energetics of the polymer solar cell based on the SWNT/GO/P3HT:PCBM/Al device structure.

### The I-V characteristic and performance of the devices

The current-voltage characteristics of the solar cells based on the SWNT/GO/P3HT:PCBM/Al device structure with different thicknesses of GO interfacial layers are shown in figure 3.18. Firstly, the device consisting of no GO interfacial layer with a structure of SWNT/P3HT:PCBM/Al exhibits a short circuit current density ( $J_{sc}$ ) of 8.45 mA/cm<sup>2</sup>, an open circuit voltage ( $V_{oc}$ ) of 0.48V, a fill factor (FF) of 0.42, and a power conversion efficiency ( $\eta$ ) of 1.67 % respectively under A.M.1.5 (100 mW/cm<sup>2</sup>) illumination. After depositing one layer GO thin film on top of the SWNT electrode, a large improvement in the photovoltaic performance of the SWNT/GO/P3HT:PCBM/Al device can be obtained, exhibiting a  $J_{sc}$  of 10.3 mA/cm<sup>2</sup>, an  $V_{oc}$  of 0.57 V and a FF of 0.53, corresponding to a power conversion efficiency ( $\eta$ ) of 3.11 %. Further increase in the layer thickness of GO thin films results in a clear trend of decreasing power conversion efficiencies of lower  $J_{sc}$  and FFs with increased serial resistance and decreased shunt resistance. To examine whether the resistivity of GO is the key factor to affect the power conversion efficiencies, we have further optimized the device performances of the SWNT/GO/P3HT:PCBM/Al solar cells by using more conductive reduced GO thin films to replace the original insulating GO layers. It has been reported that the insulating GO can be transferred to more graphene-like reduced GO (r-GO) through exposure to hydrazine vapor and/or

annealing in inert conditions to render the material electrically conductivity.[33] The sheet resistance can be largely lowered from  $1 \times 10^9 \Omega/\square$  for the pristine GO to  $5 \times 10^4$ ,  $6 \times 10^3$  and  $1 \times 10^3 \Omega/\square$  for the reduced GO thin films by exposure to hydrazine vapor for 3 minutes, 1 hour and 4 hours respectively. Figure 3.19 exhibits the photovoltaic performances of devices using one layer of reduced GO thin films as an anode interfacial layer with different hydrazine exposure time. All these devices consisting of reduced GO thin films show significant decreasing cell efficiencies of lower  $J_{sc}$ ,  $V_{oc}$  and FF, accompanying with a large enhancement of leakage current.

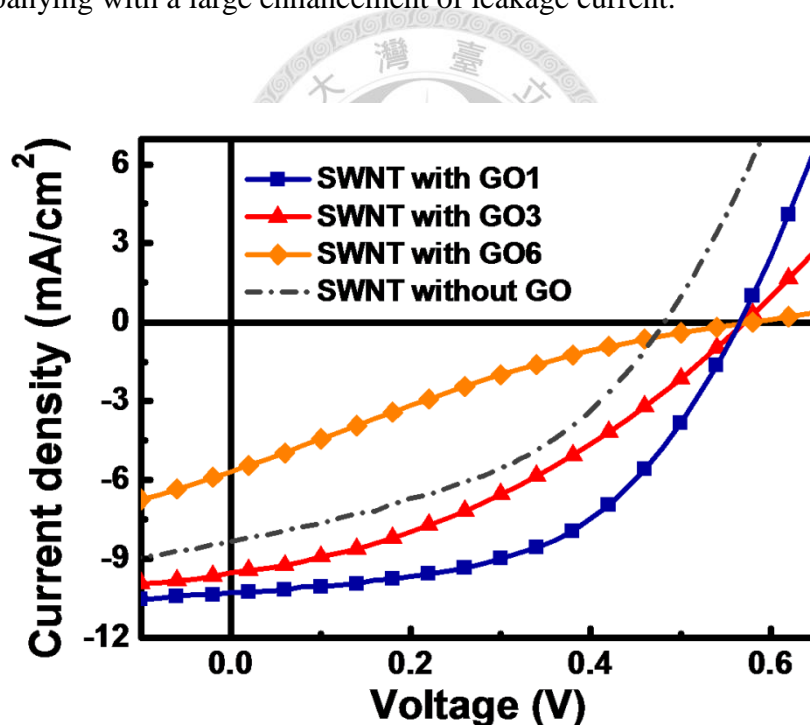


**Figure 3.18** The current-voltage characteristics of the SWNT/GO/P3HT:PCBM/Al solar cells with different thicknesses of GO layers. (under A.M.1.5,  $100 \text{ mW/cm}^2$  illumination) GO1, GO3 and GO6 correspond to one, three and six layers of GO.



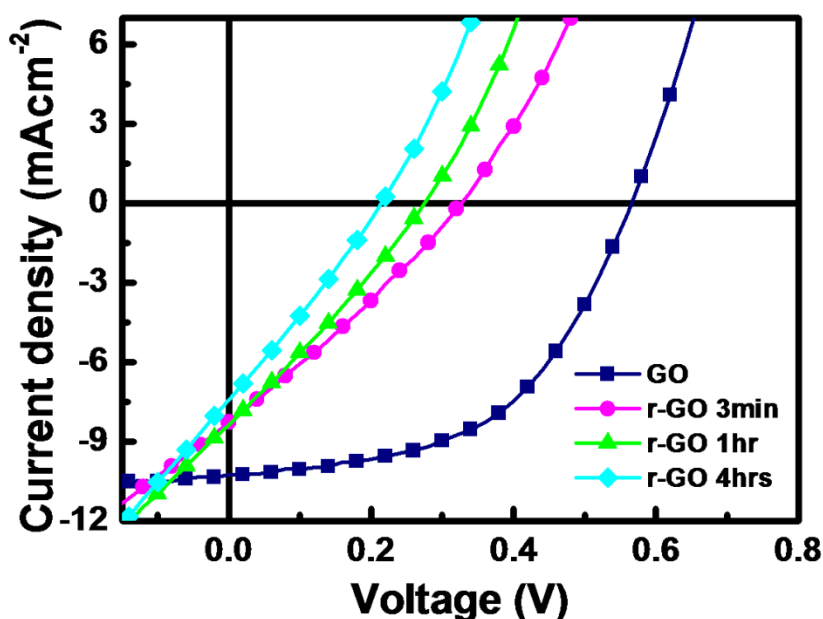


**Figure 3.19** The photovoltaic performances of SWNT/r-GO/P3HT:PCBM/Al devices consisting of one layer of GO thin films reduced with different hydrazine exposure time.

**Table 3.1** Summary of the photovoltaic performance of different devices as described in the text. The SWNT/GO corresponds to the devices consisting of different number layers of GO as the interfacial layer. The SWNT/r-GO corresponds to the devices consisting of one layer of r-GO with different hydrazine exposure time. The control device consists of the device structure of ITO/PEDOT:PSS/P3HT:PCBM/Al.

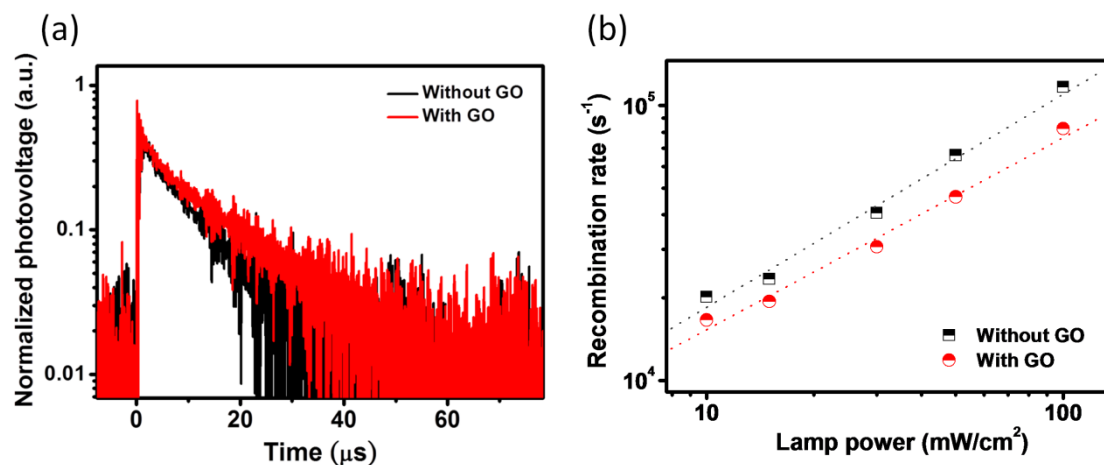
	$V_{oc}$ (V)	$J_{sc}$ (mA/cm <sup>2</sup> )	F.F.	PCE (%)
ITO/PEDOT:PSS (Control)	<b>0.57</b>	<b>11.0</b>	<b>0.57</b>	<b>3.57%</b>
SWNT (No GO)	<b>0.48</b>	<b>8.33</b>	<b>0.42</b>	<b>1.67%</b>
SWNT/GO(GO1)	<b>0.57</b>	<b>10.3</b>	<b>0.53</b>	<b>3.10%</b>
SWNT/GO(GO3)	<b>0.57</b>	<b>9.53</b>	<b>0.36</b>	<b>1.99%</b>
SWNT/GO(GO6)	<b>0.58</b>	<b>5.68</b>	<b>0.20</b>	<b>0.65%</b>
SWNT/r-GO (GO1) (3 mins)	<b>0.32</b>	<b>8.27</b>	<b>0.34</b>	<b>0.89%</b>
SWNT/r-GO (GO1) (1 hr)	<b>0.27</b>	<b>8.36</b>	<b>0.34</b>	<b>0.76%</b>
SWNT/r-GO (GO1) (4 hrs)	<b>0.21</b>	<b>7.41</b>	<b>0.33</b>	<b>0.51%</b>

Table 3.1 summarizes all the device performance of the solar cells based on the SWNT/GO (or r-GO) anodes with different configurations. For comparison, we have also fabricated a control device using the conventional polymer solar cell of

ITO/PEDOT:PSS/P3HT:PCBM/Al under the same fabrication conditions, which exhibits a photovoltaic performance of a  $J_{sc}$  of 11.0 mA/cm<sup>2</sup>, an  $V_{oc}$  of 0.57V, a FF of 0.57, and a power conversion efficiency ( $\eta$ ) of 3.57 %. From the above result, it is concluded that the device consisting of the thinnest insulating GO interfacial layer gives the best performance of a SWNT/GO/P3HT:PCBM/Al solar cell.

### **Transporting mechanism of the GO hole transporting interfacial layer**

To further examine the origin of transporting mechanism of the GO hole transporting interfacial layer, we have employed the conductive-AFM (C-AFM) and transient photovoltage (TPV) measurements to probe the transport and recombination behaviors of the nanocarbon based polymer solar cells. Figure 3.20(a) shows the photovoltage transient curves of the devices with and without GO. The device with 1 layer GO thin film had the longer carrier life time, which means the lower recombination rate of the device. The dependences of recombination rates versus different illumination powers are shown in figure 3.20(b). The device with GO always shows the lower recombination rate compared to that without GO, indicating that 1 layer GO can facilitate the holes transporting from P3HT polymer matrix to the SWNT anode.

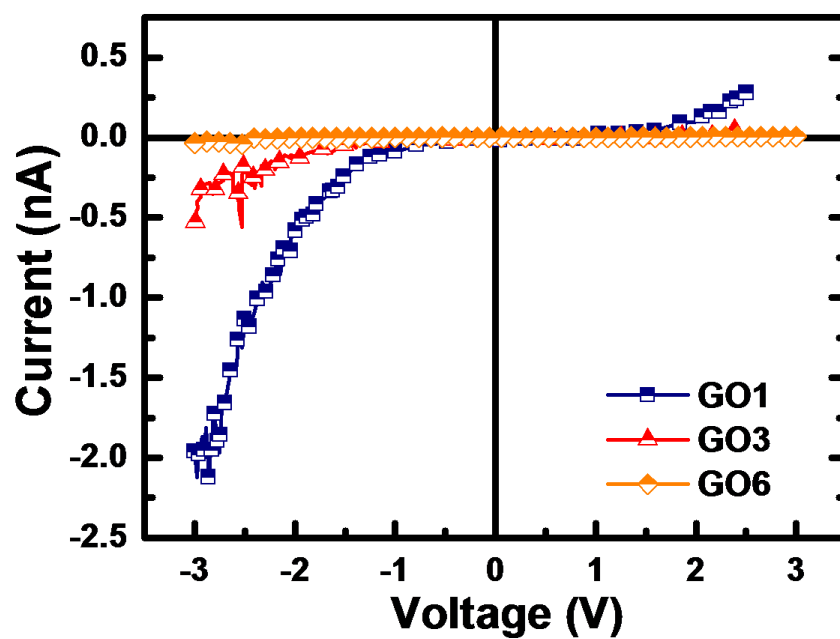


**Figure 3.20** (a) Photovoltage transient decay curves of SWNT/GO (or no GO) /P3HT:PCBM/Al solar cell device. (b) Power dependent recombination rates of the two devices in (a).

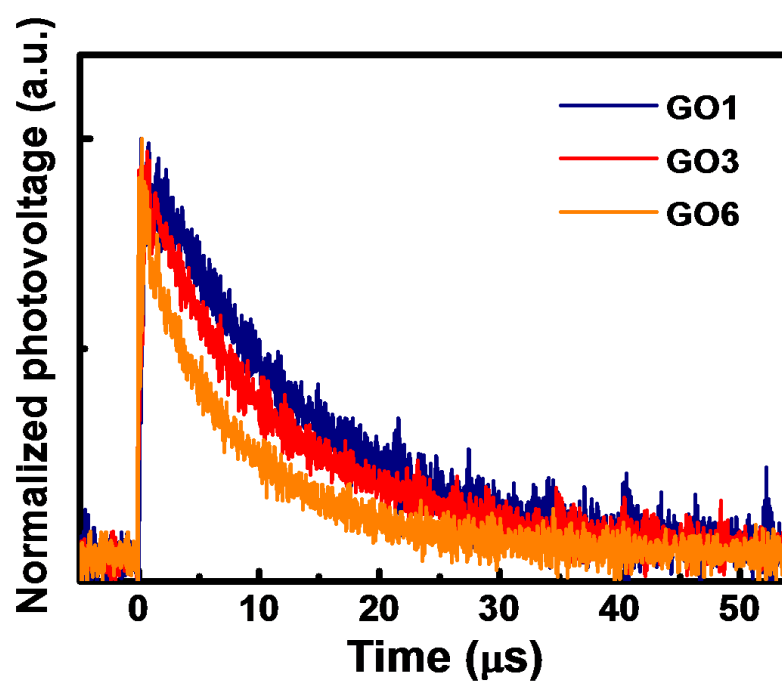
We have further employed C-AFM to find out the effect of thick GO thin film.

Figure 3.21 shows the local current-voltage characteristics of the devices consisting of one, three and six layers of GO thin films onto the SWNT electrodes. It is found that the conductive current becomes largely suppressed from 2 nA to 0.06 nA at bias of -3V as the thickness of the GO thin films increases from one to six layers. This insulating property of thick GO layer may lead to the accumulation of holes at the anode side, which explains the S-shaped I-V characteristics. Some similar results were carefully investigated and already reported by Wagenpfahl et al.[36] The thin insulating GO layer in the nanocarbon based polymer solar cell therefore acts as a tunneling barrier which favors holes to transport through and blocks electrons effectively, as compared to the energy level diagram in figure 3.17. The transporting of holes in GO is very different from that in PEDOT:PSS which is very conductive and is contrast to the NiO interfacial

layer where transfer of holes to the anode electrode is facilitated by injection into  $\text{Ni}^{2+}$  defect levels close to the valence band.[21] The tunneling probability of holes from P3HT becomes largely reduced while the thickness of the GO layer is increased, although electrons can be effectively blocked. Additionally, from transient photovoltage measurement, we can observe that the electron-hole back recombination rate was increased with GO thickness as a result of a decreasing recombination time of 13.7, 12.5, and 8.9  $\mu\text{s}$  for the devices consisting of one, three and six layers of GO respectively as shown in figure 3.22. The results were consistent with increased serial resistance and decreased shunt resistance. On the other hand, while the conductivity of GO is increased by increasing the concentration of  $sp^2$  fractions through reduction, both electrons and holes can transport along these more conductive  $sp^2$  sites via delocalized  $\pi$  electron[33] toward the SWNT anode. As a result, holes and electrons can be easily recombined at the SWNT anode with a shorter recombination time of 6.7  $\mu\text{s}$ , giving large leakage current and low shunt resistance.



**Figure 3.21** Conductive-AFM current-voltage characteristics of the devices consisting of one, three and six layers of GO thin films onto the SWNT electrodes.



**Figure 3.22** The transient photovoltage decay curves of the SWNT/GO/P3HT:PCBM/Al solar cell devices.

### 3.5. Conclusion

In conclusion, we have demonstrated nanocarbon based polymer solar cells which consist of the SWNT transparent electrode, GO hole transporting anode interfacial layer and polymer/fullerene hybrid photoactive layer. A thin layer of GO between the anode and the active layer can not only facilitate holes transporting to the anode but also prevent from the protrusion of SWNTs into the active layer. This fully solution processable SWNT/GO anode can be a good candidate to replace the conventional transparent conducting electrode ITO and the hole transport layer PEDOT:PSS, providing a new route to develop low-cost, large area and flexible organic photovoltaic devices. Further optimization of the SWNT/GO anode via the enhanced conductivity and transparency of the SWNT electrode or improved uniformity of the SWNT/GO interface should lead to additional improvements in the device performance.

### 3.6. Reference

- [1] W. Ma, C. Yang, X. Gong, K. Lee, A. J. Heeger, Thermally Stable, Efficient Polymer Solar Cells with Nanoscale Control of the Interpenetrating Network Morphology, *Adv. Func. Mater.* **15**, 1617 (2005).
- [2] W. U. Huynh, J. J. Dittmer, A. P. Alivisatos, Hybrid Nanorod-Polymer Solar Cells, *Science* **295**, 2425 (2002).
- [3] G. Li, V. Shrotriya, J. Huang, Y. Yao, T. Moriarty, K. Emery, Y. Yang, High-efficiency solution processable polymer photovoltaic cells by self-organization of polymer blends, *Nat. Mater.* **4**, 864 (2005)
- [4] J. L. Delgado, P.-A. Bouit, S. Filippone, M<sup>a</sup> A. Herranz, N. Martin, Organic photovoltaics: a chemical approach, *Chem. Commun.* **46**, 4853 (2010).
- [5] Y.-Y. Lin, T.-H. Chu, S.-S. Li, C.-H. Chuang, C.-H. Chang, W.-F. Su, C.-P. Chang, M.-W. Chu, C.-W. Chen, Interfacial Nanostructuring on the Performance of Polymer/TiO<sub>2</sub> Nanorod Bulk Heterojunction Solar Cells, *J. Am. Chem. Soc.* **131**, 3644 (2009).
- [6] Y.-H. Kim, S.-H. Lee, J. Noh, S.-H. Han, Performance and stability of electroluminescent device with self-assembled layers of poly(3,4-ethylenedioxythiophene)-poly(styrenesulfonate) and polyelectrolytes, *Thin Solid Films* **510**, 305 (2006).
- [7] M. P. de Jong, L. J. van IJzendoorn, M. J. A. de Voigt, Stability of the interface between indium-tin-oxide and poly(3,4-ethylenedioxythiophene)/poly(styrenesulfonate) in polymer light-emitting diodes, *Appl. Phys. Lett.* **77**, 2255 (2000).
- [8] E. Fortunato, D. Ginley, H. Hosono, D. C. Paine, Transparent Conducting Oxides for Photovoltaics, *MRS Bull.* **32**, 242 (2007).

- [9] G. Gustafsson, Y. Cao, G. M. Treacy, F. Klavetter, N. Colaneri, A. J. Heeger, Flexible light-emitting diodes made from soluble conducting polymers, *Nature* **357**, 477 (1992).
- [10] J. Huang, X. Wang, A. J. deMello, J. C. deMello, D. D. C. Bradley, Efficient flexible polymer light emitting diodes with conducting polymer anodes, *J. Mater. Chem.* **17**, 3551 (2007).
- [11] Z. Wu, Z. Chen, X. Du, J. M. Logan, J. Sippel, M. Nikolou, K. Kamaras, J. R. Reynolds, D. B. Tanner, A. F. Hebard, A. G. Rinzler, Transparent, Conductive Carbon Nanotube Films, *Science* **305**, 1273 (2005).
- [12] C. M. Aguirre, S. Auvray, S. Pigeon, R. Izquierdo, P. Desjardins, R. Martel, Carbon nanotube sheets as electrodes in organic light-emitting diodes, *Appl. Phys. Lett.* **88**, 183104 (2006).
- [13] A. D. Pasquier, H. E. Unalan, A. Kanwal, S. Miller, M. Chhowalla, Conducting and transparent single-wall carbon nanotube electrodes for polymer-fullerene solar cells, *Appl. Phys. Lett.* **87**, 203511 (2005).
- [14] M. W. Rowell, M. A. Topinka, M. D. McGehee, H. J. Prall, G. Dennler, N. S. Sariciftci, L. Hu, G. Gruner, Organic solar cells with carbon nanotube network electrodes, *Appl. Phys. Lett.* **88**, 233506 (2006).
- [15] V. Sgobba, D. M. Guldi, Carbon nanotubes as integrative materials for organic photovoltaic devices, *J. Mater. Chem.* **18**, 153 (2008).
- [16] J.-H. Ahn, H.-S. Kim, K.-J. Lee, S. Jeon, S. J. Kang, Y. Sun, R. G. Nuzzo, J. A. Rogers, Heterogeneous Three-Dimensional Electronics by Use of Printed Semiconductor Nanomaterials, *Science* **314**, 1754 (2006).
- [17] R. Jackson, B. Domercq, R. Jain, B. Kippelen, S. Graham, Stability of Doped Transparent Carbon Nanotube Electrodes, *Adv. Funct. Mater.* **18**, 2548 (2008).
- [18] J.-Y. Lee, S. T. Connor, Y. Cui, P. Peumans, Solution-Processed Metal Nanowire



- Mesh Transparent Electrodes, *Nano Lett.* **8**, 689 (2008).
- [19] S. Bae, H. Kim, Y. Lee, X. Xu, J.-S. Park, Y. Zheng, J. Balakrishnan, T. Lei, H. R. Kim, Y. I. Song, Y.-J. Kim, K. S. Kim, B. Ozyilmaz, J.-H. Ahn, B. H. Hong, S. Iijima, Roll-to-roll production of 30-inch graphene films for transparent electrodes, *Nat. Nanotechnol.* **5**, 574 (2010).
- [20] V. Shrotriya, G. Li, Y. Yao, C.-W. Chu, Y. Yang, Transition metal oxides as the buffer layer for polymer photovoltaic cells, *Appl. Phys. Lett.* **88**, 073508 (2006).
- [21] M. D. Irwin, D. B. Buchholz, A. W. Hains, R. P. H. Chang, T. J. Marks, p-Type semiconducting nickel oxide as an efficiency-enhancing anode interfacial layer in polymer bulk-heterojunction solar cells, *PNAS* **105**, 2783 (2008).
- [22] T.-J. Park, S. Banerjee, T. Hemraj-Benny, S. S. Wong, Purification strategies and purity visualization techniques for single-walled carbon nanotubes, *J. Mater. Chem.* **16**, 141 (2006).
- [23] H. C. Schniepp, J.-L. Li, M. J. McAllister, H. Sai, M. Herrera-Alonso, D. H. Adamson, R. K. Prud'homme, R. Car, D. A. Saville, I. A. Aksay, Functionalized Single Graphene Sheets Derived from Splitting Graphite Oxide, *J. Phys. Chem. B* **110**, 8535 (2006).
- [24] A. Lerf, H. He, M. Forster, J. Klinowski, Structure of Graphite Oxide Revisited, *J. Phys. Chem. B* **102**, 4477 (1998).
- [25] H. He, J. Klinowski, M. Forster, A. Lerf, A new structural model for graphite oxide, *Chem. Phys. Lett.* **287**, 53 (1998).
- [26] C. Mattevi, G. Eda, S. Agnoli, S. Miller, K. A. Mkhoyan, O. Celik, D. Mastrogiovanni, G. Granozzi, E. Garfunkel, M. Chhowalla, Evolution of Electrical, Chemical, and Structural Properties of Transparent and Conducting Chemically Derived Graphene Thin Films, *Adv. Funct. Mater.* **19**, 2577 (2009).
- [27] S.-S. Li, K.-H. Tu, C.-C. Lin, C.-W. Chen, M. Chhowalla, Solution-Processable

- Graphene Oxide as an Efficient Hole Transport Layer in Polymer Solar Cells, *ACS Nano* **4**, 3169 (2010).
- [28] M. Hirata, T. Gotou, S. Horiuchi, M. Fujiwara, M. Ohba, Thin-film particles of graphite oxide 1:: High-yield synthesis and flexibility of the particles, *Carbon* **42**, 2929 (2004).
- [29] G. Eda, Y.-Y. Lin, S. Miller, C.-W. Chen, W.-F. Su, M. Chhowalla, Transparent and Conducting Electrodes for Organic Electronics from Reduced Graphene Oxide, *Appl. Phys. Lett.* **92**, 233305 (2008).
- [30] G. Eda, Y.-Y. Lin, C. Mattevi, H. Yamaguchi, H.-A. Chen, I.-S. Chen, C.-W. Chen, M. Chhowalla, Blue Photoluminescence from Chemically Derived Graphene, *Adv. Mater.* **22**, 505 (2010).
- [31] K. A. Mkhoyan, A. W. Contryman, J. Silcox, D. A. Stewart, G. Eda, C. Mattevi, S. Miller, M. Chhowalla, Atomic and Electronic Structure of Graphene-Oxide, *Nano Lett.* **9**, 1058 (2009).
- [32] G. Eda, M. Chhowalla, Graphene-Based Composite Thin Films for Electronics, *Nano Lett.* **9**, 814 (2009).
- [33] C. Mattevi, G. Eda, S. Agnoli, S. Miller, K. A. Mkhoyan, O. Celik, D. Mastrogianni, G. Granozzi, E. Garfunkel, M. Chhowalla, Evolution of Electrical, Chemical, and Structural Properties of Transparent and Conducting Chemically Derived Graphene Thin Films, *Adv. Funct. Mater.* **19**, 2577 (2009).
- [34] J.C. Meyer, A.K. Geim, M.I. Katsnelson, K.S. Novoselov, D. Obergfell, S. Roth, C. Girit, A. Zettl, On the roughness of single- and bi-layer graphene membranes, *Solid State Comm.* **143**, 101 (2007).
- [35] R. C. Tenent, T. M. Barnes, J. D. Bergeson, A. J. Ferguson, B. To, L. M. Gedvilas, M. J. Heben, J. L. Blackburn, Ultrasooth, Large-Area, High-Uniformity, Conductive Transparent Single-Walled-Carbon-Nanotube Films for Photovoltaics

Produced by Ultrasonic Spraying, *Adv. Mater.* **21**, 3210 (2009).

- [36] A. Wagenpfahl, D. Rauh, M. Binder, C. Deibel, V. Dyakonov, S-shaped current-voltage characteristics of organic solar devices, *Phys. Rev. B* **82**, 115306 (2010).
- [37] J. Tauc, Optical properties and electronic structure of amorphous Ge and Si, *Mat. Res. Bull.* **3**, 37 (1968).



## Chapter 4 Polymer solar cells based on all-graphene electrodes

### 4.1. Introduction

The unique optical,[1,2] electrical,[3] mechanical[4,5] and chemical[6,7] properties of graphene have triggered numerous fundamental and technological studies. In the view of these properties, many potential applications of graphene have already been reported in various aspects, such as field-effect transistors,[8] ultrafast photodetectors,[9] bio-sensors,[10,11] ultracapacitors[12] and transparent conducting electrodes.[13–19]

One of the most promising applications is transparent conducting electrodes, owing to the high optical transparency (>90%) and good electrical conductance ( $<100\Omega/\square$ ) of graphene films, which are comparable to the current state-of-the-art indium tin oxide.

Various methods to make thin-films of graphene have been developed like the scotch tape-method,[20] epitaxial growth,[21] and reduced from GO thin film, but they were either unsuitable for large-area fabrication or having poor electrical conductivity.

Therefore, how to make a high quality, large-scale graphene on the substrate became a critical issue. In 2009, Li and colleagues discovered and demonstrated a CVD method that used centimeter-scale copper foils,[22] making a big progress in producing large-scale, high-quality graphene films. On the other hand, S. Bae et al. improved the way of transferring graphene from copper foil onto a foreign substrate from formerly used PMMA method to thermal release method.[13] These two important breakouts

have opened a new route to large-area, roll-to-roll fabrication of high quality graphene films for future transparent conducting electrode applications.

In polymer solar cell, graphene usually served as the anode owing to its p-type prone characteristic, replacing ITO in the conventional device[18,23] or the high workfunction metal in the inverted type device.[24] However, there were still some disadvantages. In conventional polymer solar cell device, a low workfunction metal electrode must be used as cathode, which is not quite stable under air ambience. And in inverted type device, brittle and expensive ITO was still served as transparent electrode for electrons to transport. As a result, here we propose a new concept of an all-graphene polymer photovoltaic device by using graphene as the both side electrodes. To achieve the goal, controlling the Fermi levels of graphene films with a desirable workfunction to be used as a cathode or anode is critically essential, because the band offsets between electrodes and the photoactive semiconducting layer will strongly affect the carrier injection or collecting efficiencies through the contact of devices. Fortunately, graphene has shown a great versatility of modifying its electronic properties by some chemical doping in previous reports.[13,31,38] In this work, we would like to demonstrate a systematic modification of graphene electrodes through controllable n- and p- type chemical doping of layer-by-layer stacked graphene films, for tuning the workfunction of graphene to be suitable as cathode or/and anode in polymer solar cells. Based on the

layer-by-layer chemical doping technique, the first n-type graphene electrode and the prototype of polymer solar cell with both top and bottom electrodes using n- and p- type doped graphene films were reported. Consisting the structure of p-type graphene/GO/P3HT:PCBM/n-type graphene, the all-graphene polymer photovoltaic device has the advantages of that it is low-cost, semitransparent, and can be roll-to-roll producible without any high vacuum process, showing the potential for the practical use of polymer solar cells in the future. The schematic structure of all-graphene polymer photovoltaic device is shown in figure 4.1.

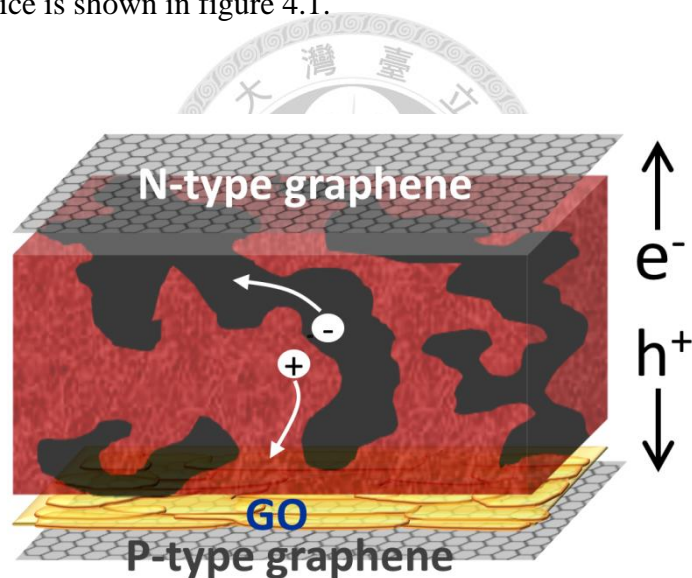


**Figure 4.1** Schematic device structure of all-graphene polymer solar cell.

## 4.2. Graphene as transparent conducting electrode

### 4.2.1. The synthesis of graphene on copper foil

The growth of graphene films on Cu foils (Aldrich) by CVD process was similar to the works reported previously.[22,25] In brief, a roll of  $25\ \mu\text{m}$ -thick Cu foil was inserted into 1.5- inch fused silica tube and then heated to  $950^\circ\text{C}$  with flowing of 20 sccm  $\text{H}_2$  in 30 minutes . Prior to graphene growth, the sample was further annealed for 30 minutes by keeping the same flow rate of  $\text{H}_2$  and temperature. Then 100 sccm  $\text{CH}_4$  was introduced with the same  $\text{H}_2$  flow for graphene growth. After a growth time of 30 minutes,  $\text{CH}_4$  was shut off and the system was naturally cooled down to room temperature in  $\text{H}_2$  flow. All the procedures were conducted at low pressure ( $\sim 500\ \text{mTorr}$  during the growth stage) by using a mechanical pump. Figure 4.2(a)(b) shows the schematics of graphene growth process by CVD.

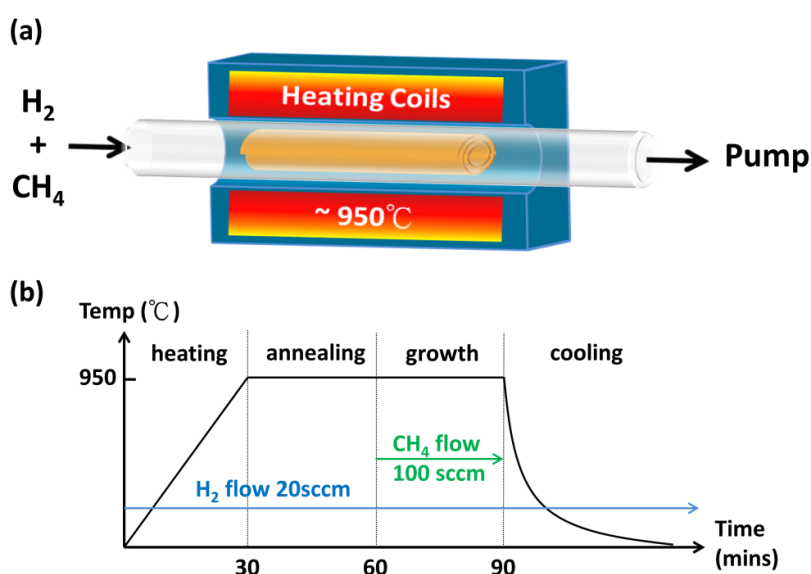


**Figure 4.2** (a) Schematic of graphene growth by CVD. (b) Illustration of the graphene growth process.

#### 4.2.2. The preparation of graphene electrode

After growth, we have to transfer graphene from Cu foils to target substrate to obtain the graphene electrode. Here we employed the roll-to-roll production method reported by S. Bae et al.[13] First, the Cu foil with graphene was attached to a thermal release tape (Nitto Denko). Then the Cu foil was removed by using 1M iron nitrate as etchant. Subsequently, graphene film on thermal release tape was rinsed with DI water and then we can cut the tape into the shape we wanted. To obtain patterned graphene electrode on substrate, we inserted the tape into two hot rollers (150°C) with substrate and then the graphene film will be transferred from the tape to substrate. By repeating the steps several times on the same substrate, we can stack up multilayer graphene films for better electrical conductance. Figure 4.3 shows the schematic of the roll-to-roll transfer process of graphene films. And figure 4.4 shows the different layers of graphene films we made on the same substrate. The SEM and AFM images reveals that the graphene electrodes we prepared by roll-to-roll method were quite uniform and smooth except the existence of few wrinkles of graphene films.(fig. 4.5 & fig. 4.6)

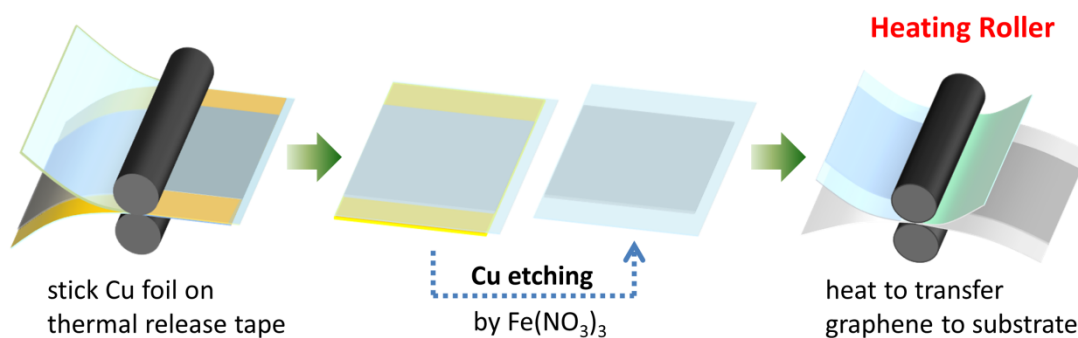


**Figure 4.3** Schematic of the roll-to-roll production of graphene films grown on Cu foil.



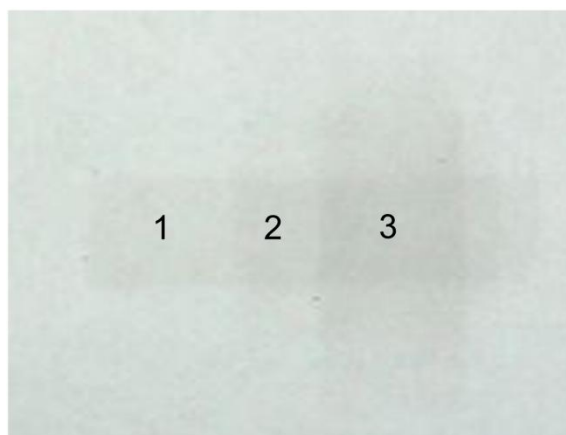


**Figure 4.4** The photograph of different layers graphene on same glass substrate.

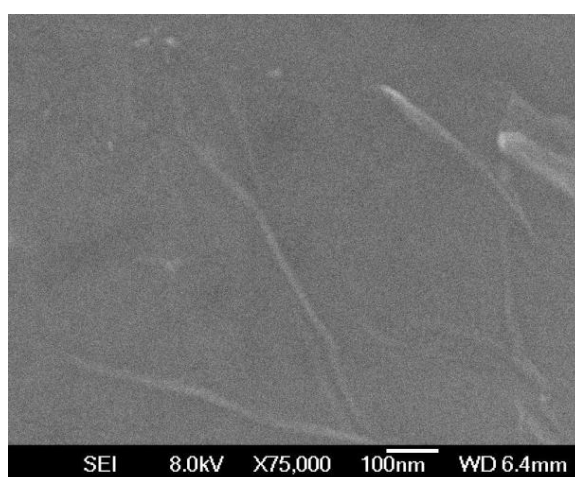


**Figure 4.5** SEM planar view image of four layer graphene films. The white line areas were the wrinkles of graphene films.

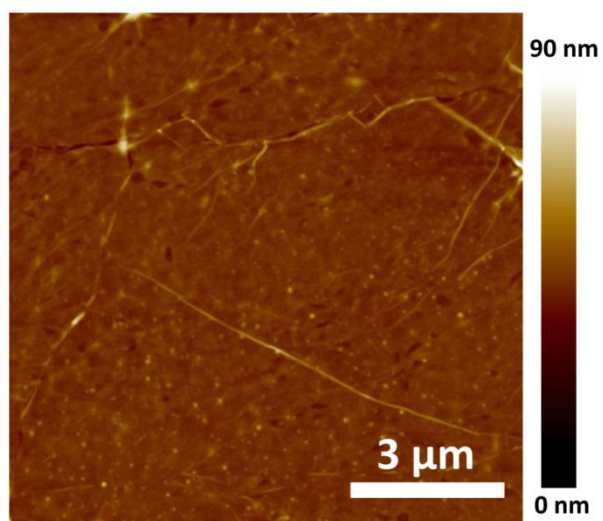


**Figure 4.6** AFM height image of four layers graphene films. The wrinkles of graphene films were clearly visible.

### 4.3. Work function engineering of graphene electrodes by using layer-by-layer doping technique

For tuning the workfunction of graphene electrode, we use the n- and p-type doping techniques to change the energy level of pristine graphene.  $\text{HNO}_3$  treatment was used here to achieve p-type graphene, which would lower the Fermi level of graphene as well as increase the work function of graphene electrode. On the contrary, PEI was used as an n-type dopant to raise the Fermi level of graphene, so we can obtain a low workfunction graphene electrode by PEI doping. Figure 4.7 illustrate the changes in Fermi level after n- and p-type doping of graphene. In addition, in this study we employed the layer-by-layer doping concept proposed by A. Kasry and F. Gunes,[14,26] trying to change the electronic properties of entire graphene electrode, not only in the surface of graphene electrode.

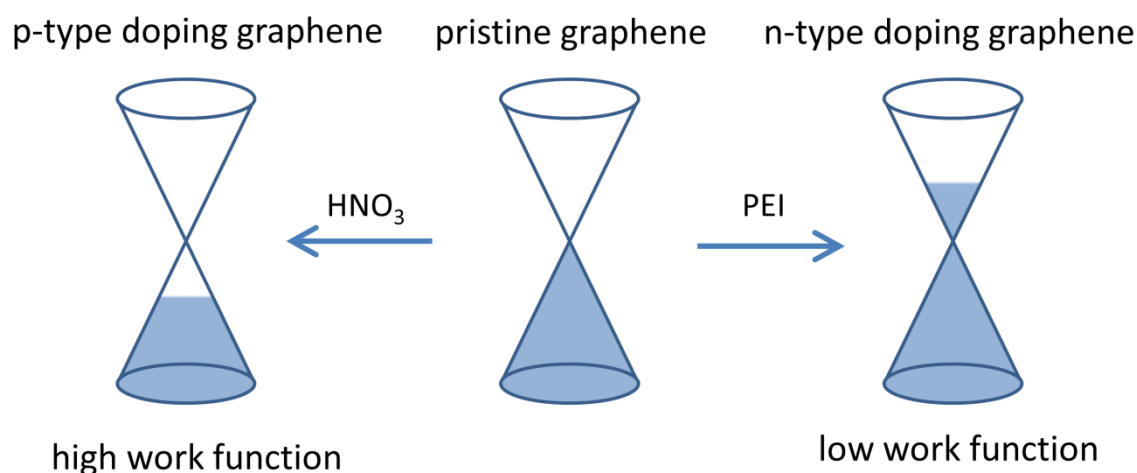


**Figure 4.7** Schematics of Fermi level changes in graphene band structure after n- and p-type doping process.

### 4.3.1. The preparation of p-type doping graphene electrode

P-type doping of graphene was achieved by utilizing nitric acid treatment, which was previously reported.[13,14] First, the graphene on thermal release tape was transferred onto the substrate. Then we dipped the substrate with the first layer graphene into the nitric acid solution (16M) for 10 seconds and thereafter dried by gentle nitrogen flow. At last we rinsed the sample with DI water and dried by nitrogen flow again. Layer-by-layer doping of multilayer graphene electrode was obtained by repeating the cycle several times. In this study we mainly used four layers graphene films as our high workfunction electrode. The schematic procedures of fabricating layer-by-layer p-type doped graphene electrode are shown in figure 4.8.

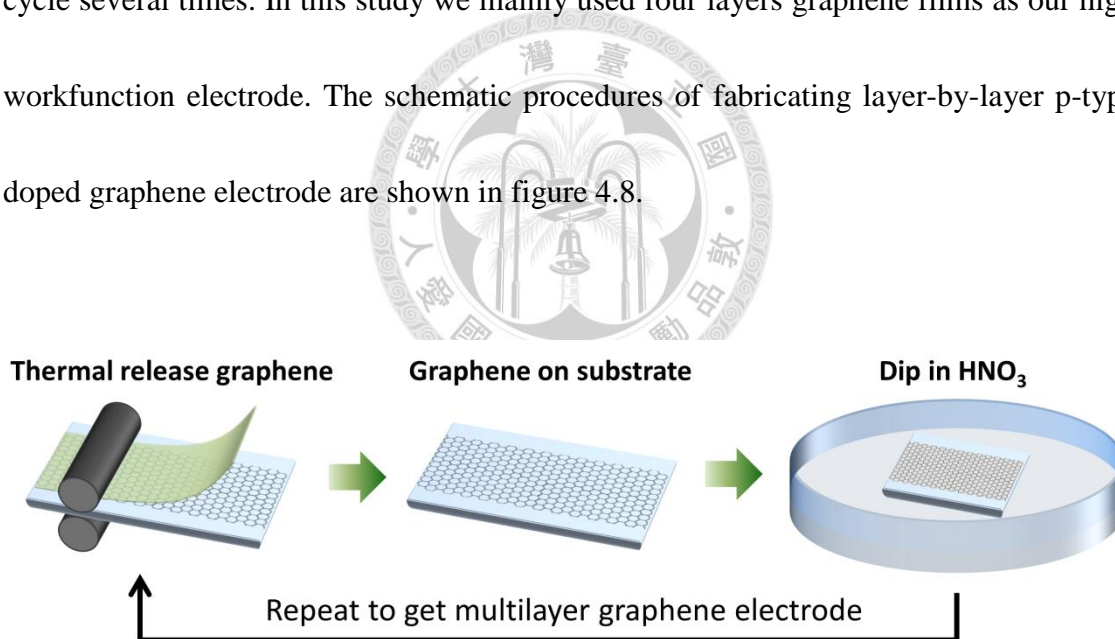


**Figure 4.8** The process of fabricating layer-by-layer p-type doped graphene electrode.

### 4.3.2. The preparation of n-type doping graphene electrode

N-type doping of graphene was achieved by using poly(ethyleneimide) (PEI) as the electron dopant. PEI is a kind of amine-containing polymers, which can provide the excess electrons to our graphene films. The PEI we used in the study was branched and its average molecular weight was ~25000 g/mol, whose chemical structure is shown in figure 4.9. This n-type doping method was previously used on SWNTs,[27–29] and recently was also used to dope graphene sheets.[30,31] Here we took the advantage of this n-type doping method to obtain the low workfunction graphene electrode on our polymer solar cells.

Because the low workfunction electrode was directly made onto the active layer of polymer solar cell, we cannot dip the whole device into the solution like  $\text{HNO}_3$  treatment. Therefore, we dipped the thermal release tape into PEI aqueous solution (20%) for doping. In detail, the thermal release tape with graphene was dipped into PEI solution about one minute, following by rinsing in DI water to remove the excess PEI. And then the doped graphene was thermal transferred onto the device. We can also simply repeat the doping and transferring process to get multilayer n-doped graphene electrode. Here we mainly used four layers graphene films as our cathode in polymer photovoltaic device. Figure 4.10 shows the fabrication process of n-type doped graphene top electrode on the device.

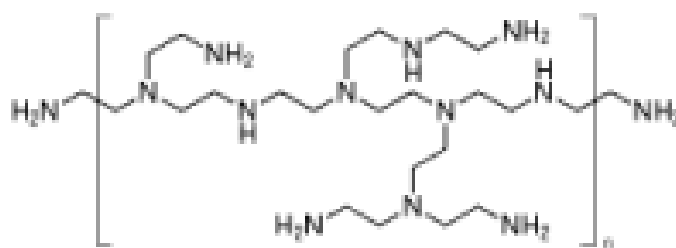


**Figure 4.9** The chemical structure of poly(ethyleneimine) (PEI).

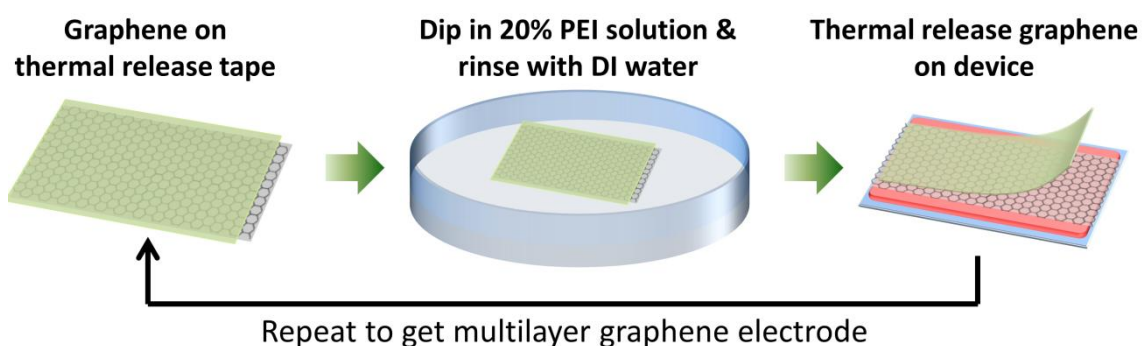


**Figure 4.10** The process of fabricating layer-by-layer n-type doped graphene electrode.

#### 4.3.3. Characterization of LbL doped graphene electrode

In the work, we used X-ray photoelectron spectroscopy, Raman spectroscopy, field-effect transistor and Hall effect measurement to look into the doping effects on the electronic properties of graphene. Some basic characteristics of transparent conducting graphene electrode, such as transparency, sheet resistance and workfunction, were also examined by transmission spectroscopy, 4-point probe measurement and Kelvin probe force microscopy (KPFM) respectively.

## X-ray photoelectron spectroscopy

X-ray photoelectron spectroscopy (XPS) is a powerful tool to identify the elemental composition, empirical formula, chemical state and electronic state of the elements that exist within a material. Here we employed XPS analysis to examine the n- and p-type doping effects of four layers graphene films. Figure 4.11(a) shows the C1s spectra of graphene films. In HNO<sub>3</sub> doped graphene, The C1s peak corresponding to sp<sup>2</sup> and sp<sup>3</sup> hybridized states was shifted to lower energy, which is similar to the work previously reported.[13] And the blue shift in PEI doped graphene may mainly attributed to the carbon atoms in PEI molecules. The PEI doping effects can be further examined by N1s spectra. In PEI doped graphene, we can clearly observe the N1s peak while there was nothing in HNO<sub>3</sub> doped and pristine graphene, which indicates the successful adsorption of PEI molecules on graphene films. Figure 4.11(b) shows the N1s spectra of pristine and doped graphene films.

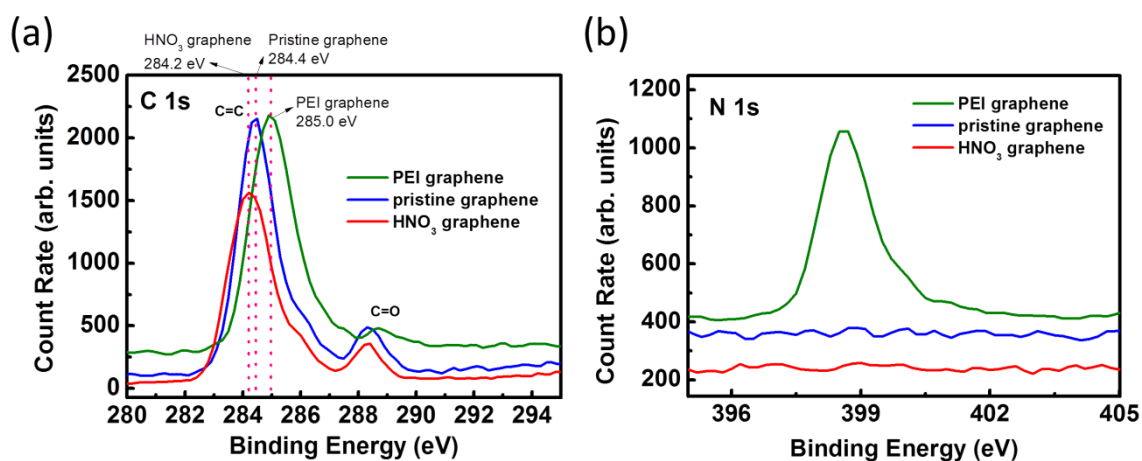


**Figure 4.11** The XPS (a) C1s and (b) N1s spectra of pristine and doped graphene films.

## Raman spectroscopy

Raman spectroscopy is a powerful non-destructive tool for identifying the number of layers, structure, doping and disorder of graphene.[32–36] The prominent Raman features in graphene are the G-band peak at  $\sim 1584\text{ cm}^{-1}$  and the 2D band at  $\sim 2650\text{ cm}^{-1}$ , which position depend on the excitation laser energy. Figure 4.12 shows the Raman spectra of doped and pristine single layer graphene by using 632.8 nm Laser as the excitation source. There were no obvious D peaks in the Raman spectra, indicating the high quality of graphene synthesized by CVD.

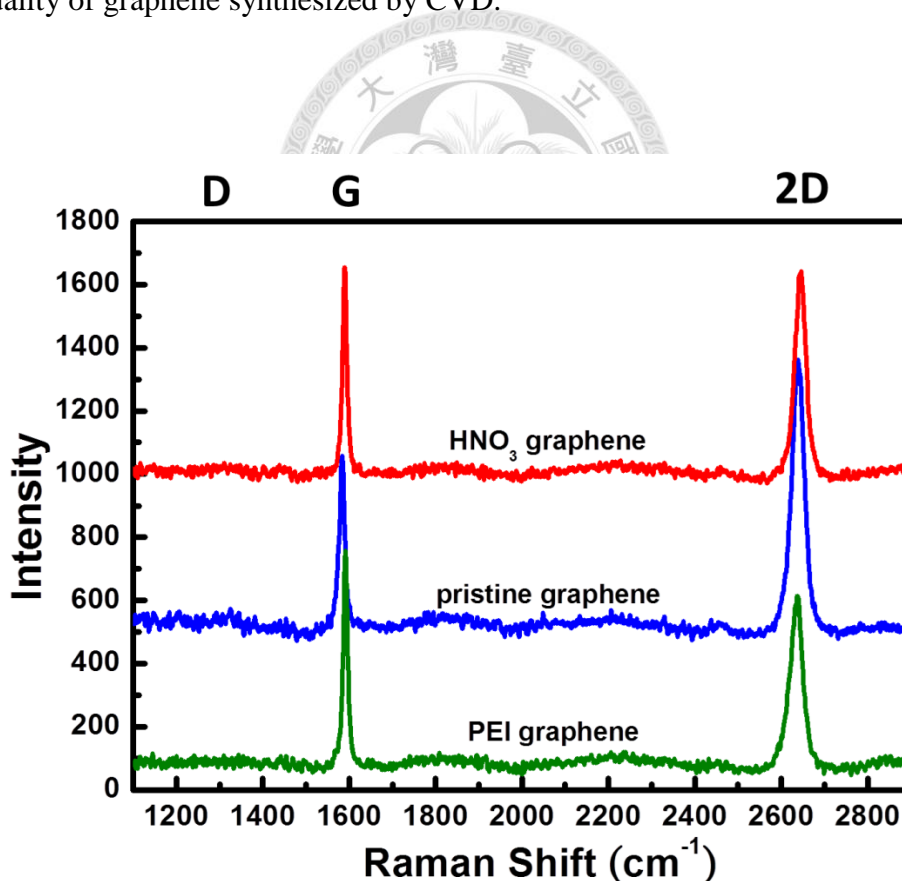


**Figure 4.12** Raman spectra of pristine and doped single layer graphene.

Moreover, the G-band peak was found blue-shifting from  $1584\text{ cm}^{-1}$  of pristine graphene to  $1590\text{ cm}^{-1}$  and  $1592\text{ cm}^{-1}$  of  $\text{HNO}_3$  and PEI doped graphene respectively.(Fig.4.13) This blue-shift of G-band peak was contributed to the non-adiabatic removal of Kohn anomaly from  $\Gamma$  point resulting from electron or hole doping.[33] Also the corresponding decreases in full-width at half-maximum (FWHM) of G-band peak were observed. This sharpening of FWHM(G) occurs because of the blockage of the decay channel of phonons into electron-hole pairs due to the Pauli exclusion principle, when the electron hole gap becomes higher than phonon energy.[33] Further information were provided by the peak intensity changes of G-band and 2D-band. It was found that the  $I(2D)/I(G)$  ratio decreased from 1.58 of pristine graphene to 1.00 of  $\text{HNO}_3$  doped graphene and 0.80 of PEI doped graphene, which are owing to the stronger dependence of 2D-band to the doping density. All the trends of changes in Raman spectra after our chemical doping consisted with the works previously reported.[33,34] Table 4.1 concluded the FWHM(G), G-band position and  $I(2D)/I(G)$  value obtained from the Raman spectra of pristine and doped graphene in figure 4.12.



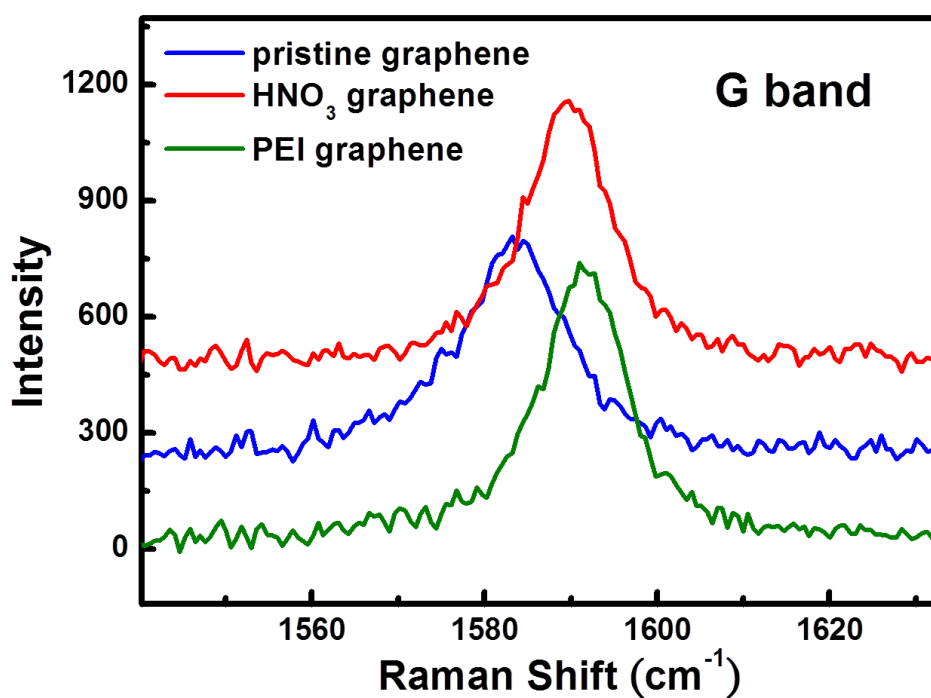


**Figure 4.13** The G-band peaks of pristine and doped graphene.

**Table 4.1** The value of FWHM(G), G-band position,  $I(2D)/I(G)$  in the Raman spectra of pristine and doped graphene.(fig4.12)

	FWHM(G) (cm <sup>-1</sup> )	G position (cm <sup>-1</sup> )	$I(2D)/I(G)$
<b>HNO<sub>3</sub> graphene</b>	11.4	1589.78	1.00
<b>Pristine graphene</b>	14.4	1583.85	1.58
<b>PEI graphene</b>	11.8	1591.55	0.80

### Field-effect transistor

Field-effect transistors (FETs) were fabricated to investigate the electronic properties of pristine and doped graphene. In the work, pristine and doped graphene films were transferred onto 200nm SiO<sub>2</sub>/p<sup>+</sup> Si substrate, where SiO<sub>2</sub> served as the dielectric and p<sup>+</sup> Si served as the bottom gate for applying gate voltage. Source/drain electrodes were deposited on graphene by thermal evaporation of Cr (2nm)/Au (60nm). The length and width between two electrodes were 50 μm. All measurements were preceded under vacuum ambience (10<sup>-4</sup> Torr). In general, graphene shows a bipolar behavior in field-effect transistor, resulting in a “V” shape in drain current-gate voltage (I<sub>d</sub>-V<sub>G</sub>) plot. Figure 4.14 shows the I<sub>d</sub>-V<sub>G</sub> characteristics of pristine and doped single layer graphene FETs. The Dirac point of pristine graphene was a little deviated from V<sub>G</sub>=0 V, and the absolute value of the slope in negative gate region is larger than that in positive gate region. It indicated that the pristine graphene is p-type prone due to slightly doping by O<sub>2</sub> and H<sub>2</sub>O molecules in our environment. And after n-type doping by PEI, the Dirac point was shifted to V<sub>G</sub>=-40V, exhibiting an n-type characteristic of PEI doped graphene. On the contrary, after graphene was p-type doped by HNO<sub>3</sub> treatment, the I<sub>d</sub>-V<sub>G</sub> plot shows a great positive shift of Dirac point, even out of the gate voltage range that we can measure. However, the absolute value of the slope compared to that of pristine graphene was decreased, as well as the corresponding the hole

mobility decreased from  $2885 \text{ cm}^2 \text{ V}^{-1} \text{ s}^{-1}$  of pristine graphene to  $501 \text{ cm}^2 \text{ V}^{-1} \text{ s}^{-1}$  of  $\text{HNO}_3$  doped graphene. It may be contributed by the created  $-\text{COOH}$  group by  $\text{HNO}_3$  treatment would not only withdraw electrons to create excess holes but also act as obstacles blocking the holes to transport.

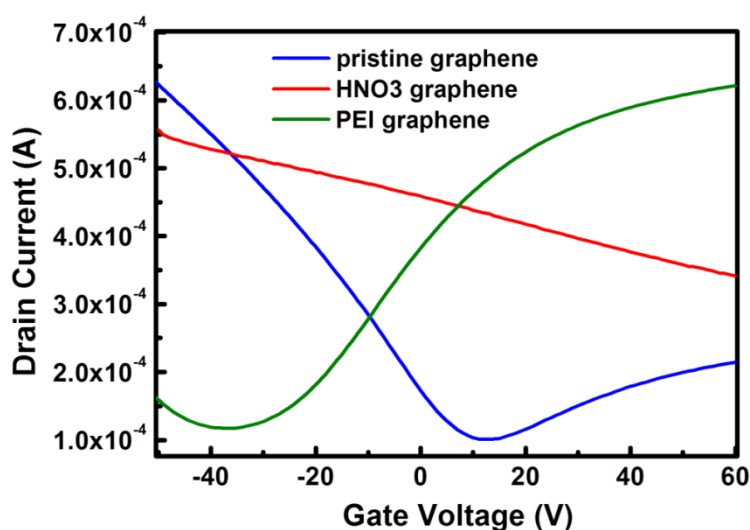


**Figure 4.14**  $I_d$ - $V_G$  characteristics of pristine and doped single layer graphene FETs.

### Hall effect measurement

Here we employed Hall effect measurement to estimate the carrier concentration and sheet resistance changes of graphene films before and after doping process. Figure 4.15 shows the sheet resistance of graphene films with different layers. The sheet resistances of p-type doped graphene films were the lowest while that of n-type doped graphene were slightly larger than pristine graphene. And when there is more than four layers of graphene films, the sheet resistance would not decrease much even that it was added more layers of graphene. The carrier densities depending on different graphene

layers are shown in figure 4.16. A great increase of hole density from the order of  $10^{12}$  to  $10^{13-14}$  was observed after  $\text{HNO}_3$  p-type doping. This increase of hole density explains the origin of the decreasing sheet resistance of graphene after  $\text{HNO}_3$  p-type doping. On the other hand, PEI doping has changed the major carrier type of graphene from hole to electron, resulting in a negative carrier density value in the Hall effect measurement.

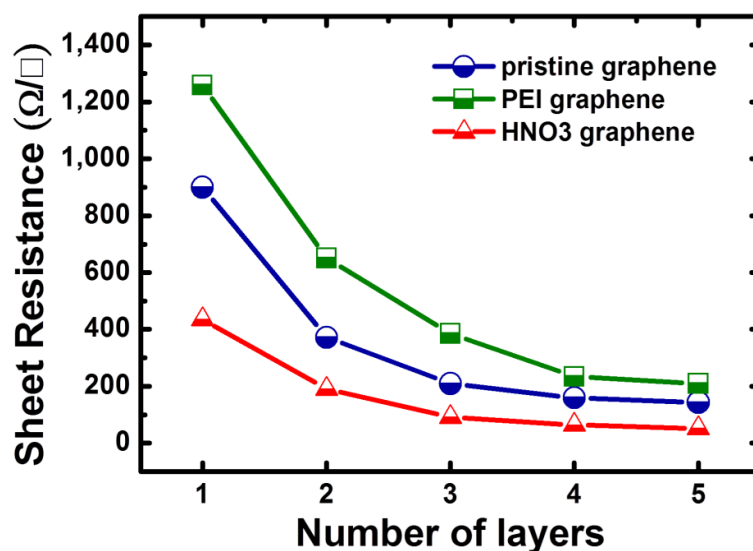


Figure 4.15 The sheet resistance of pristine and doped graphene with different layers.

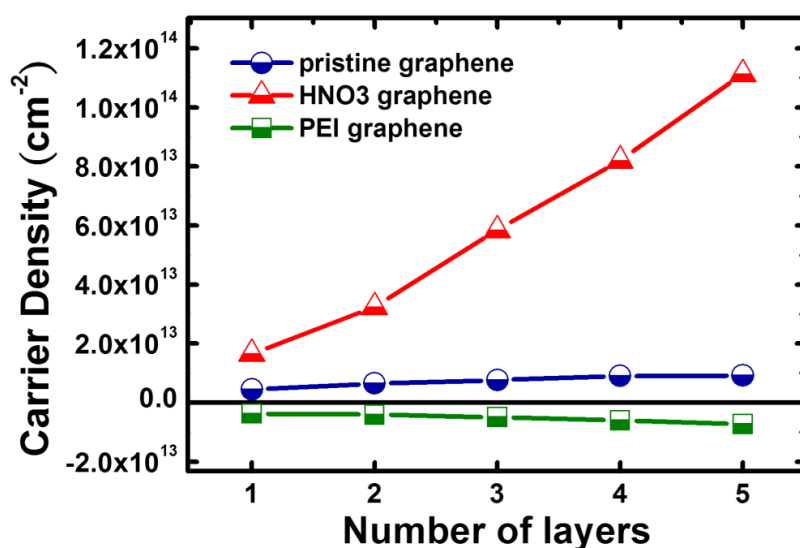
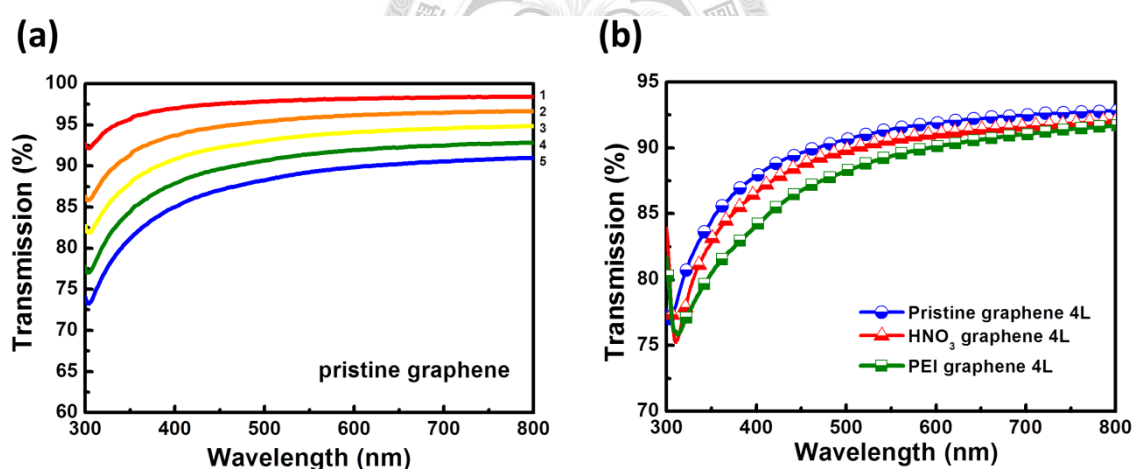


Figure 4.16 The carrier densities dependent on different layers of graphene.

## Optical and electrical properties

To utilize graphene films as the transparent conducting electrode, sheet resistance and transmittance are the essential parts needing to be known. The transmission spectra of pristine graphene with different layers are shown in figure 4.17(a). There was about 2.3% difference in transparency of each graphene layer, which is consistent to the theoretical absorption value of single layer graphene. Figure 4.17(b) shows the transmission spectra of three kinds of graphene with 4 layers. The slight decrease in transparency after doping may be caused by the larger scattering of doped graphene films.



**Figure 4.17** (a) Transmission spectra of pristine graphene films with different layers. (b) Transmission spectra of pristine and doped graphene films with 4 layers.

By further combining the transmittance and sheet resistances of graphene films, we can make the plot of transmissions versus sheet resistances shown in figure 4.18.

Graphene has exhibited a great potential to serve as transparent conducting electrode

owing to its low sheet resistance and high transparency, which is almost comparable to the conventionally used ITO. In the following photovoltaic device fabrication, the four layers n- and p-type doped graphene films were selected to be the cathode and anode respectively.

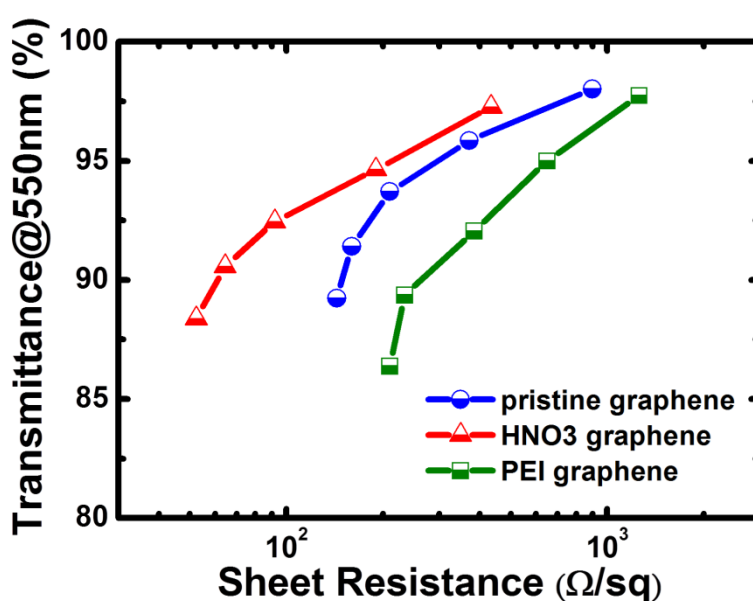


**Figure 4.18** The transmittance at 550 nm of graphene films as a function of their resistance before and doping process.

#### Workfunction measurement by Kelvin probe force microscopy (KPFM)

Workfunction is also an important characteristic of an electrode. In this work, we determined the workfunction of pristine and doped graphene electrodes by KPFM. Figure 4.19(a) shows the surface morphology of 4 layers pristine graphene films and the corresponding mapping of workfunction (figure 4.19(b)), and figure 4.20, figure 4.21 show that of HNO<sub>3</sub> and PEI doped graphene films.

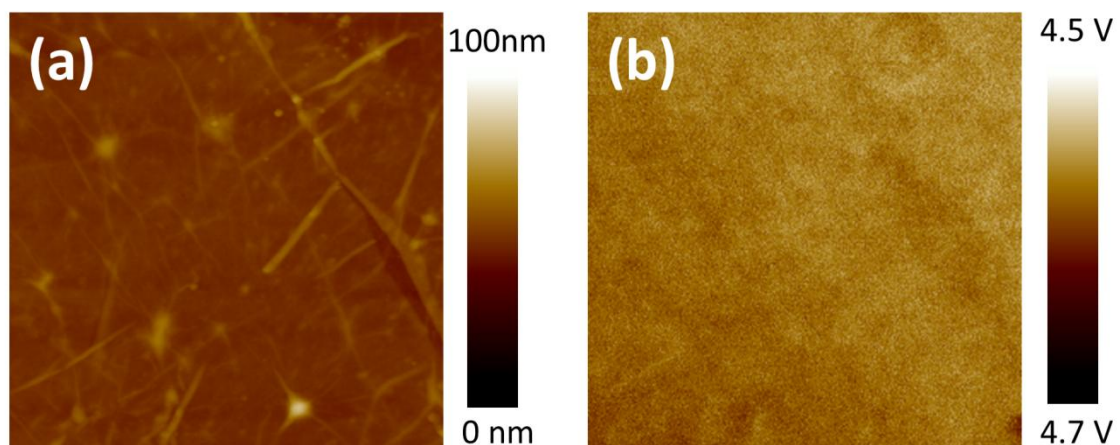


**Figure 4.19** (a) Surface morphology and (b) workfunction mapping of 4 layers pristine graphene films.

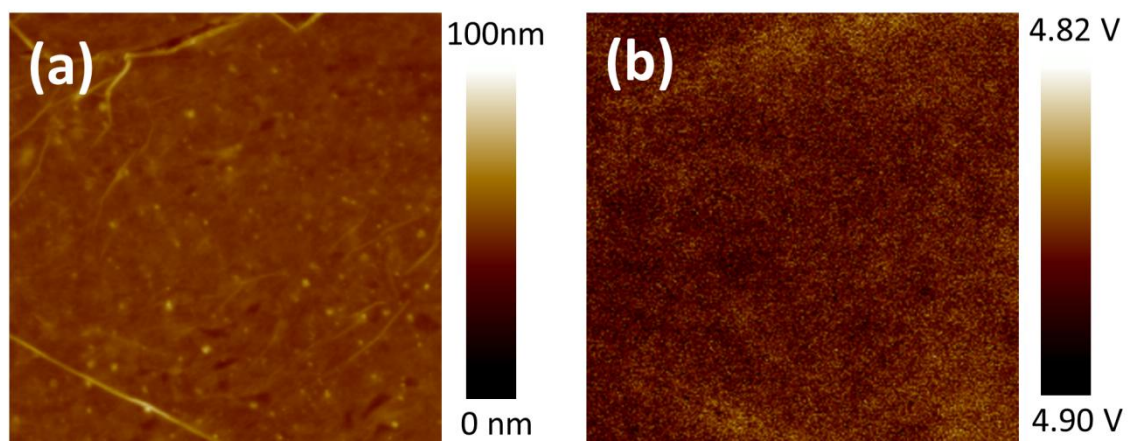


**Figure 4.20** (a) Surface morphology and (b) workfunction mapping of 4 layers HNO<sub>3</sub> doped graphene films.

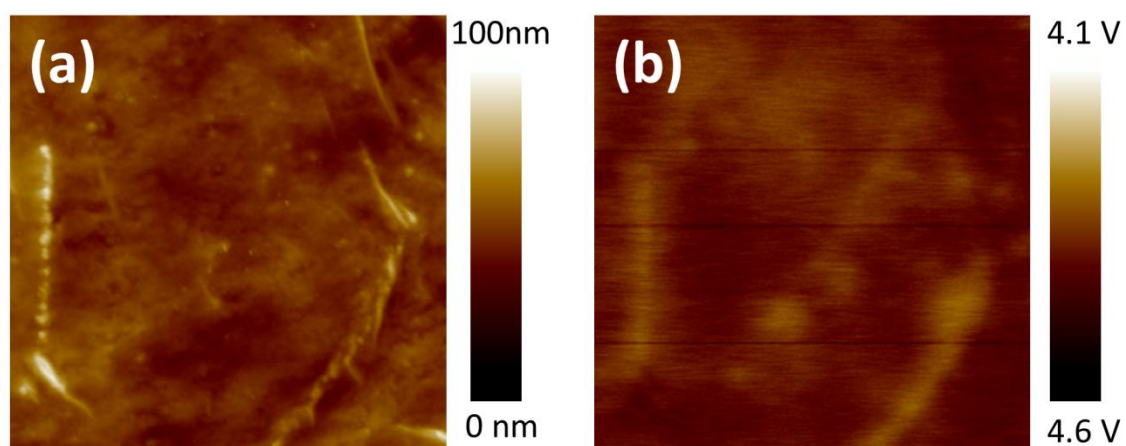


**Figure 4.21** (a) Surface morphology and (b) workfunction mapping of 4 layers PEI doped graphene films.

Figure 4.22 shows the workfunction dependence of different layers of graphene films. Because a single layer graphene is only ~1nm, the workfunction measured by KPFM will strongly affect by the substrate underneath. Only when there were more than four layers graphene films, the workfunctions would become close to the original values. The workfunction of pristine, HNO<sub>3</sub> doped and PEI doped 4 layers graphene films measured by KPFM were 4.63 eV, 4.86 eV and 4.32 eV respectively. So here we made use of HNO<sub>3</sub> graphene films as our anode and PEI doped graphene films as our cathode in polymer photovoltaic device.

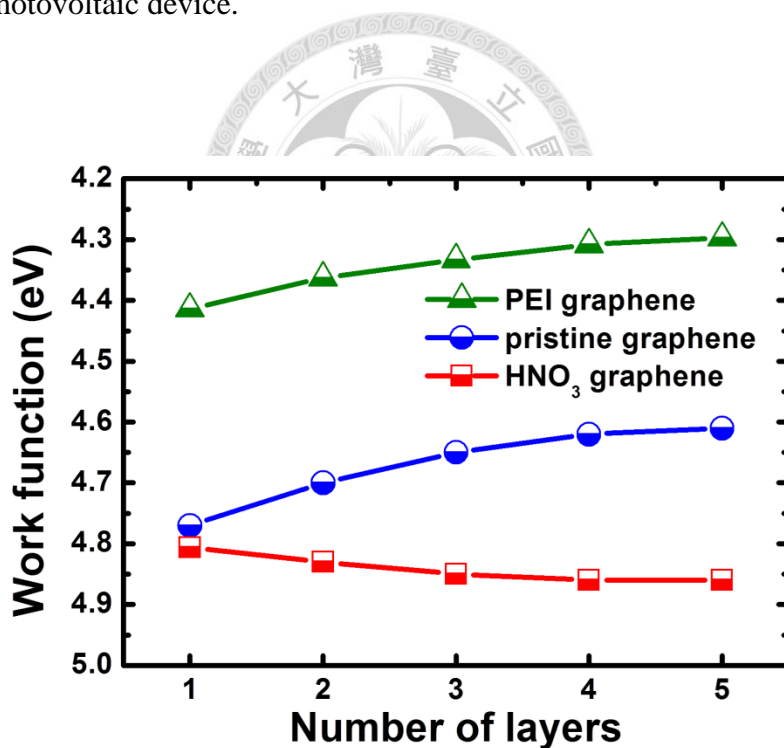


**Figure 4.22** The graphene workfunctions depend on different layers of graphene films.



#### **4.4. P3HT:PCBM polymer solar cells with n- and p-type doped graphene electrodes**

##### **4.4.1. Experimental details**

In order to know whether the polymer photovoltaic devices with n- and p-type doping graphene electrodes can work successfully, we started the experiments with changing the anode and cathode individually. And after that was the device with both side graphene electrodes.

##### **Fabrication of device with p-type doped graphene as the anode**

We first substitute the ITO by p-type doping graphene electrode. In this device, a thin layer of GO was spin-coated on the pre-prepared p-type doping graphene electrode, and then moved the sample into nitrogen filled glove box for deposition of the photoactive layers and top electrodes. The photoactive layers were deposited on top of the GO thin film by spin coating using a 2 wt% of P3HT:PCBM (weight ratio=1:0.8) blend dissolved in chlorobenzene. Al cathodes were then deposited onto the blend layers by thermal evaporation at a pressure of  $4 \times 10^{-6}$  Torr.

##### **Fabrication of device with n-type doped graphene as the cathode**

To fabricate the polymer photovoltaic device with n-type doped graphene as the cathode, we first make the conventional device without depositing the Al top electrode.

Patterned ITO substrate was used as our anode and then spin coated a thin layer GO as the hole transport layer. The photoactive layer was deposited in the glove box, using the same solution mentioned above. At last the n-type doping graphene electrode was transferred onto the active layer by the method described in 4.3.2.

### **Fabrication of device with all-graphene electrodes**

Finally, we would like to fabricate a polymer photovoltaic device without ITO anode and metal cathode, which were substituted by p- and n-type doping graphene electrode respectively. The p-type doping graphene electrode was first made by roll-to-roll transfer process, following with spin-coating a thin layer GO as hole transport layer. The photoactive layer and n-type doping graphene cathode were deposited and transferred by the same process mentioned above.

#### **4.4.2. Device with p-type doped graphene as the anode**

By replacing ITO with p-type doped graphene as the anode, the polymer photovoltaic device had the structure of p-type graphene/GO/P3HT:PCBM/Al. A schematic of this device structure is shown in figure 4.23(a), and the corresponding energy levels in energy band diagram are shown figure 4.23(b). The p-type doping of graphene here not only lower the sheet resistance but also raise the workfunction of the electrode, both of which are favorable for holes to transport. The current-voltage

characteristic under photo illumination (A.M. 1.5) of this device is shown in figure 4.24, exhibiting a short circuit current density ( $J_{sc}$ ) of  $7.74 \text{ mA cm}^{-2}$ , an open circuit voltage ( $V_{oc}$ ) of  $0.55\text{V}$ , a fill factor (FF) of  $0.41$ , and a power conversion efficiency (PCE) ( $\eta$ ) of  $1.76 \%$ . This performance corresponded to  $\sim 50\%$  of the PCE of a control device based on ITO/GO/P3HT:PCBM/Al (PCE=3.5%).

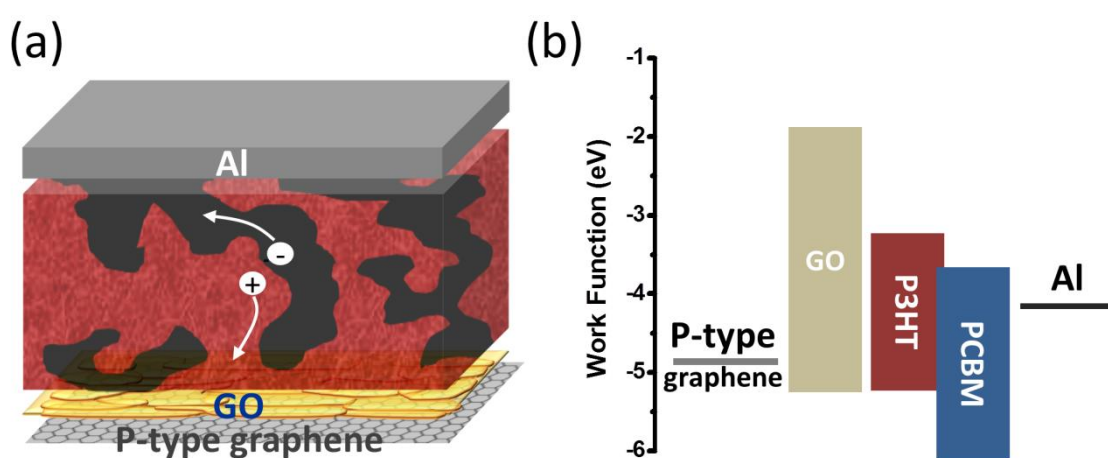


**Figure 4.23** (a) Schematic of the device structure with p-type graphene as anode. (b) The corresponding energy band diagram of the device in figure (a).

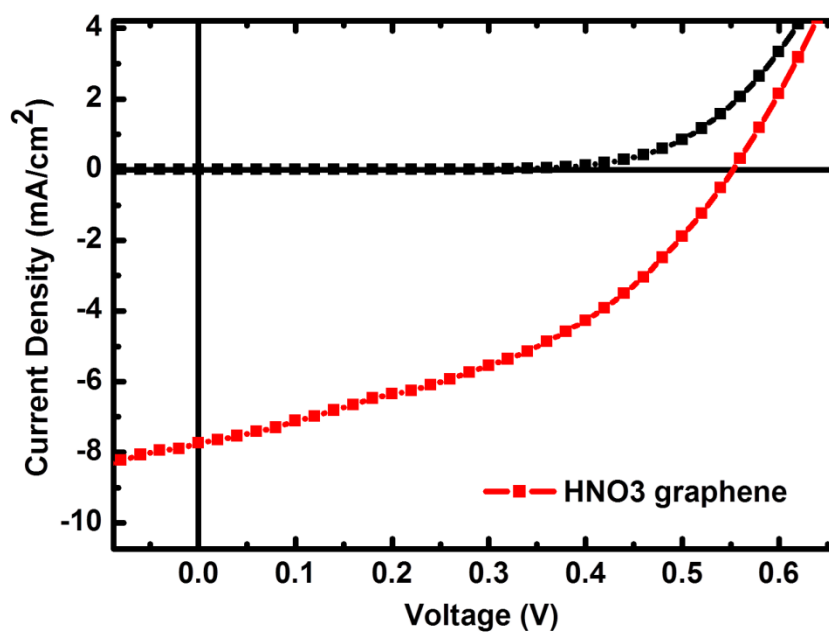


**Figure 4.24** The current-voltage characteristics of the p-type graphene/GO/P3HT:PCBM/Al polymer solar cell.

Table 4.2 lists all the parameters of the test and controlled device. We can find that there is a significant decrease in fill factor of the device with p-type graphene anode. This decrease may be caused by the wrinkles of transferred graphene films, which will easily contact with the active layer and result in the low shunt resistance in the device.

**Table 4.2** The solar cell characteristics of the device based on ITO and graphene anode.

	Voc (V)	Jsc (mA/cm <sup>2</sup> )	Fill Factor	Efficiency
Graphene/GO	0.55	7.74	0.41	1.76%
ITO/GO	0.57	11.4	0.54	3.51%

#### 4.4.3. Device with n-type doped graphene as the cathode

In this device, ITO was still served as the anode while the cathode was changed from thermal evaporated aluminum to n-type doping graphene electrode. Figure 4.25(a)(b) shows the schematic of device configuration and the corresponding energy band diagram. The current-voltage characteristic under photo illumination (A.M. 1.5) of this device is shown in figure 4.26, exhibiting a short circuit current density ( $J_{sc}$ ) of 6.10 mA cm<sup>-2</sup>, an open circuit voltage ( $V_{oc}$ ) of 0.45V, a fill factor (FF) of 0.28, and a power conversion efficiency (PCE) ( $\eta$ ) of 0.76 %. Because the graphene electrode is also transparent, there was another IV curve obtained by photo illuminating from the graphene side.

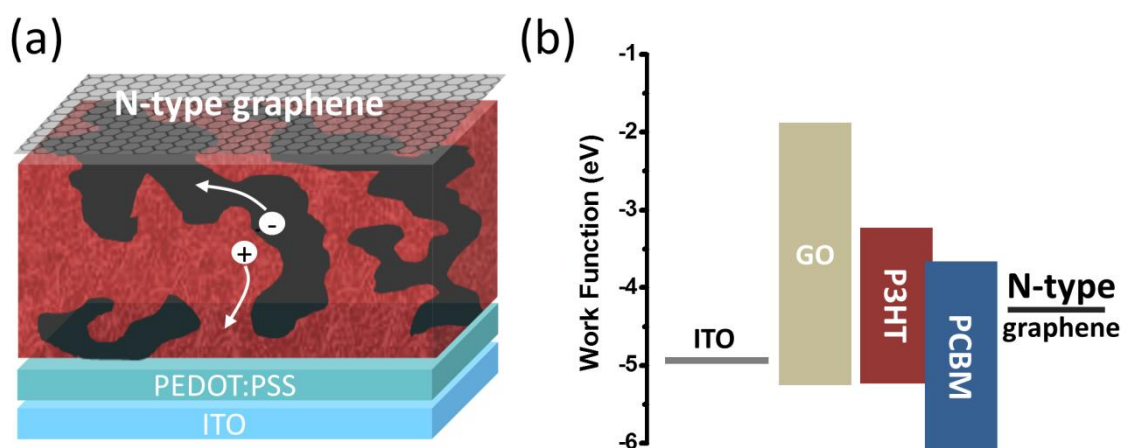


**Figure 4.25** (a) Schematic of the device structure with n-type graphene as cathode. (b) The corresponding energy band diagram of the device in figure (a).

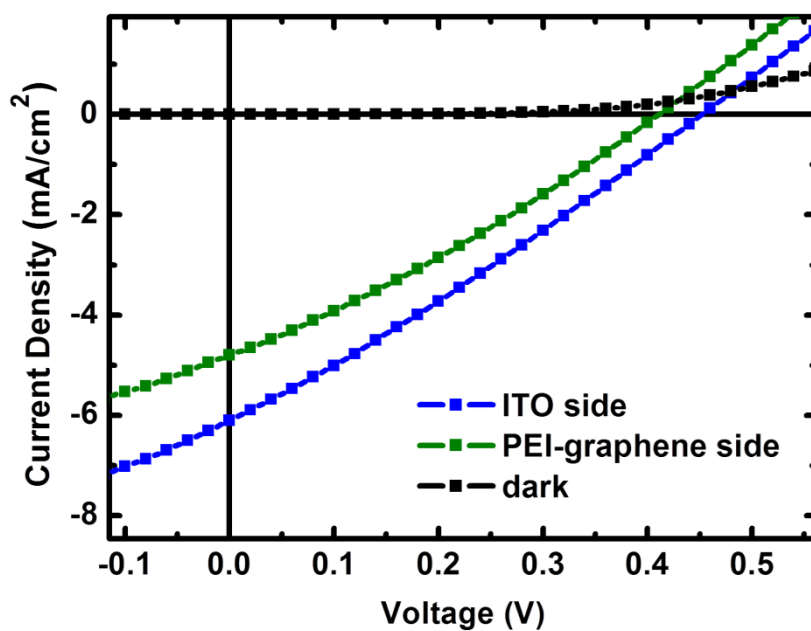


**Figure 4.26** The current-voltage characteristics of the ITO/GO/P3HT:PCBM/n-type graphene polymer solar cell.

The decreases in open-circuit voltage were observed in the IV characteristics, which may mainly contributed to that the workfunction of n-type graphene electrode was a little higher than previous aluminum cathode. And the low fill factor was resulted from the higher resistance of n-type doped graphene. The detail solar cell parameters of

this device are shown in Table 4.3.

**Table 4.3** The solar cell characteristics of the device with n-type graphene cathode. ITO and graphene side means the different directions of photo illumination.

	Voc (V)	Jsc (mA/cm <sup>2</sup> )	Fill Factor	Efficiency
<b>ITO side</b>	<b>0.45</b>	<b>6.10</b>	<b>0.28</b>	<b>0.76%</b>
<b>Graphene side</b>	<b>0.41</b>	<b>4.80</b>	<b>0.29</b>	<b>0.57%</b>

#### 4.4.4. Device with all-graphene electrodes

The ultimate goal of this work is to make the polymer photovoltaic device based on all-graphene electrode. To achieve the goal, we replaced ITO anode by p-type doping graphene electrode and replaced Al cathode by n-type doping graphene electrode, making the device with the following structure: p-type graphene / GO / P3HT:PCBM / n-type graphene. Figure 4.27(a) shows the schematic of device configuration and figure 4.27(b) shows the corresponding energy band diagram. With both side graphene electrodes, this device could also be illuminated from the different sides. Figure 4.28 shows the current-voltage characteristics of the all-graphene device. We can find that whether the light was illuminated from the anode side or cathode side, they had almost the same performance. Table 4.4 lists the basic solar cell parameters of the device illuminated from two different sides.

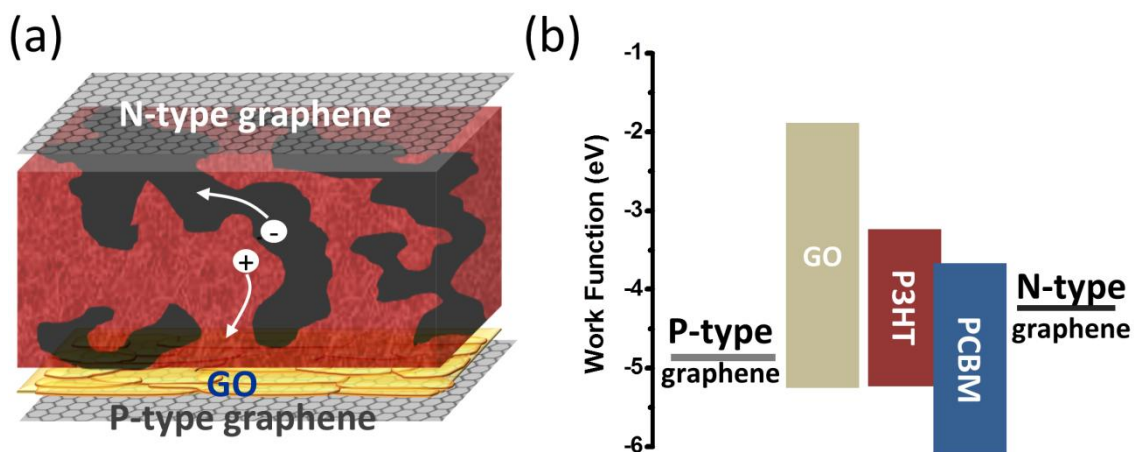


**Figure 4.27** (a) The schematic device structure of the polymer photovoltaic device based on all-graphene electrode. (b) The corresponding energy band diagram of the device in figure (a).

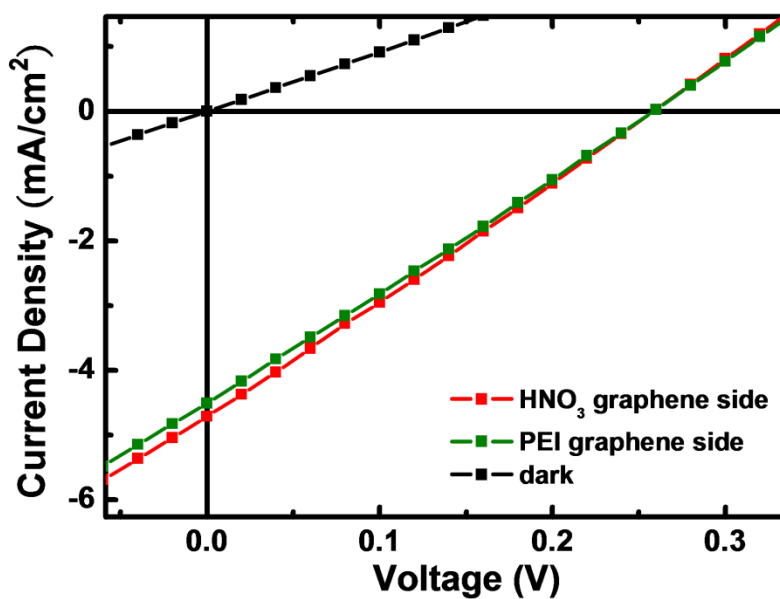


**Figure 4.28** The current-voltage characteristics of the p-type graphene/GO/P3HT:PCBM/n-type graphene polymer solar cell.

**Table 4.4** The solar cell characteristics of the device with all graphene electrode. P- and n-type graphene side means the different directions of photo illumination.

	Voc (V)	Jsc (mA/cm <sup>2</sup> )	Fill Factor	Efficiency
p-type graphene side	0.26	4.71	0.26	0.32%
n-type graphene side	0.26	4.51	0.26	0.30%

Although the device performance was not quite good, we had successfully demonstrated a working polymer photovoltaic device based on the all-graphene electrode, which had not been previously reported. This new kind of architecture provides the world a promising way to fabricate a flexible, semitransparent polymer solar cell by using low-cost, roll-to-roll process. Some further improvements in the performance may be achieved by changing a more effective dopant material, improving the transferring process to obtain a smooth surface of graphene films, and lowering the sheet resistance of graphene electrodes.





#### 4.5. Conclusion

Graphene has already shown a great versatility to apply on the future electronics. In this work, chemical doping processes were utilized to modify the intrinsic electronic properties of graphene. HNO<sub>3</sub> and PEI doped graphene had exhibited p- and n-type characteristics in Raman spectroscopy, field-effect transistor and Hall effect measurement respectively. The p- and n-type graphene electrodes can be the good candidates to replace the conventional transparent conducting electrode ITO anode and the low workfunction metal cathode. Based on this, a new architecture of polymer solar cell was demonstrated, consisting of p-type graphene as the anode, GO as the hole transport layer, P3HT:PCBM as the photoactive layer and n-type graphene as the cathode. This all-graphene electrode based polymer solar cell provides the world a potential route to fabricate a flexible, semitransparent photovoltaic device by low-cost, roll-to-roll process in the future.

#### 4.6. Reference

- [1] R. R. Nair, P. Blake, A. N. Grigorenko, K. S. Novoselov, T. J. Booth, T. Stauber, N. M. R. Peres, A. K. Geim, Fine Structure Constant Defines Visual Transparency of Graphene, *Science* **320**, 1308 (2008).
- [2] F. Bonaccorso, Z. Sun, T. Hasan and A. C. Ferrari, Graphene photonics and optoelectronics, *Nat. Photonics*, **4**, 611 (2010).
- [3] A. K. Geim, K. S. Novoselov, The rise of graphene, *Nat. Mater.* **6**, 183 (2007).
- [4] C. Lee, X. Wei, J. W. Kysar, J. Hone, Measurement of the elastic properties and intrinsic strength of monolayer graphene, *Science* **321**, 385 (2008).
- [5] J. S. Bunch, S. S. Verbridge, J.S. Alden, A. M. van der Zande, J. M. Parpia, H. G. Craighead, P. L. McEuen, Impermeable atomic membranes from graphene sheets, *Nano Lett.* **8**, 2458 (2008).
- [6] D. C. Elias, R. R. Nair, T. M. G. Mohiuddin, S. V. Morozov, P. Blake, M. P. Halsall, A. C. Ferrari, D. W. Boukhvalov, M. I. Katsnelson, A. K. Geim, K. S. Novoselov, Control of graphene's properties by reversible hydrogenation: evidence for graphene, *Science* **323**, 610 (2009).
- [7] X. Wang, X. Li, L. Zhang, Y. Yoon, P. K. Weber, H. Wang, J. Guo, H. Dai, N-doping of graphene through electrothermal reactions with ammonia, *Science* **324**, 768 (2009).
- [8] Y.-M. Lin, C. Dimitrakopoulos, K. A. Jenkins, D. B. Farmer, H.-Y. Chiu, A. Grill, Ph. Avouris, 100-GHz Transistors from Wafer-Scale Epitaxial Graphene, *Science*, **327**, 662 (2010).
- [9] F. Xia, T. Mueller, Y.-M. Lin, A. Valdes-Garcia, P. Avouris, Ultrafast graphene photodetector, *Nat. Nanotechnol.* **4**, 839 (2009).
- [10] C. H. Lu, H. H. Yang, C. L. Zhu, X. Chen, G. N. Chen, A Graphene Platform for

- Sensing Biomolecules, *Angew. Chem., Int. Ed.* **48**, 4785 (2009).
- [11] Y. Wang, Y. Shao, D. W. Matson, J. Li, Y. Lin, Nitrogen-Doped Graphene and Its Application in Electrochemical Biosensing, *ACS Nano* **4**, 1790 (2010).
- [12] M. D. Stoller, S. Park, Y. Zhu, J. An, R. S. Ruoff, Graphene-Based Ultracapacitors, *Nano Lett.* **8**, 3498 (2008).
- [13] S. Bae, H. Kim, Y. Lee, X. Xu, J.-S. Park, Y. Zheng, J. Balakrishnan, T. Lei, H. R. Kim, Y. I. Song, Y.-J. Kim, K. S. Kim, B. Ozyilmaz, J.-H. Ahn, B. H. Hong, S. Iijima, Roll-to-roll production of 30-inch graphene films for transparent electrodes, *Nat. Nanotechnol.* **5**, 574 (2010).
- [14] A. Kasry, M. A. Kuroda, G. J. Martyna, G. S. Tulevski, A. A. Bol, Chemical Doping of Large-Area Stacked Graphene Films for Use as Transparent, Conducting Electrodes, *ACS Nano* **4**, 3839 (2010).
- [15] K. S. Kim, Y. Zhao, H. Jang, S. Y. Lee, J. M. Kim, K. S. Kim, J.-H. Ahn, P. Kim, J.-Y. Choi, B. H. Hong, Large-scale pattern growth of graphene films for stretchable transparent electrodes, *Nature* **457**, 706 (2009).
- [16] P. Matyba, H. Yamaguchi, G. Eda, M. Chhowalla, L. Edman, N. D. Robinson, Graphene and Mobile Ions: The Key to All-Plastic, Solution-Processed Light-Emitting Devices, *ACS Nano* **4**, 637 (2010).
- [17] J. Wu, M. Agrawal, H. A. Becerril, Z. Bao, Z. Liu, Y. Chen, P. Peumans, Organic Light-Emitting Diodes on Solution-Processed Graphene Transparent Electrodes, *ACS Nano* **4**, 43 (2010).
- [18] Y. Wang, S. W. Tong, X. F. Xu, B. Özyilmaz, K. P. Loh, Interface Engineering of Layer-by-Layer Stacked Graphene Anodes for High-Performance Organic Solar Cells, *Adv. Mater.* **23**, 1514 (2011).
- [19] X. Wang, L. Zhi, K. Mullen, Transparent, Conductive Graphene Electrodes for Dye-Sensitized Solar Cells, *Nano Lett.* **8**, 323 (2008).

- [20] K. S. Novoselov, A. K. Geim, S. V. Morozov, D. Jiang, Y. Zhang, S. V. Dubonos, I. V. Grigorieva, A. A. Firsov, Electric Field Effect in Atomically Thin Carbon Films, *Science* **306**, 666 (2004).
- [21] E. Rollings, G.-H. Gweon, S.Y. Zhou, B.S. Mun, J.L. McChesney, B.S. Hussain, A.V. Fedorov, P.N. First, W.A. de Heer, A. Lanzara, Synthesis and characterization of atomically thin graphite films on a silicon carbide substrate, *J. Phys. Chem. Solids* **67**, 2172 (2006).
- [22] X. Li, W. Cai, J. An, S. Kim, J. Nah, D. Yang, R. Piner, A. Velamakanni, I. Jung, E. Tutuc, S. K. Banerjee, L. Colombo, R. S. Ruoff, Large-Area Synthesis of High-Quality and Uniform Graphene Films on Copper Foils, *Science* **324**, 1312 (2009).
- [23] Y. Wang, X. Chen, Y. Zhong, F. Zhu, K. P. Loh, Large area, continuous, few-layered graphene as anodes in organic photovoltaic devices, *Appl. Phys. Lett.* **95**, 063302 (2009).
- [24] Y.-Y. Lee, K.-H. Tu, S.-S. Li, C.-C. Yu, C.-C. Lin, J.-Y. Huang, K.-H. Chen, L.-C. Chen, H.-L. Chen, C.-W. Chen, Top laminated graphene electrode in semitransparent inverted polymer solar cells by simultaneous thermal annealing/releasing method. *ACS Nano* (in press).
- [25] J.-Y. Hwang, C.-C. Kuo, L.-C. Chen, K.-H. Chen, *Nanotechnology* **21**, 465705 (2010).
- [26] F. Gunes, H.-J. Shin, C. Biswas, G. H. Han, E. S. Kim, S. J. Chae, J.-Y. Choi, Y. H. Lee, Layer-by-Layer Doping of Few-Layer Graphene Film, *ACS Nano* **4**, 4595 (2010).
- [27] M. Shim, A. Javey, N. W. S. Kam, H. Dai, Polymer Functionalization for Air-Stable n-Type Carbon Nanotube Field-Effect Transistors, *J. Am. Chem. Soc.* **123**, 11512 (2001).

- [28] Z. Li, V. Saini, E. Dervishi, V. P. Kunets, J. Zhang, Y. Xu, A. R. Biris, G. J. Salamo, A. S. Biris, Polymer functionalized n-type single wall carbon nanotube photovoltaic devices, *Appl. Phys. Lett.* **96**, 033110 (2010).
- [29] K. S. Mistry, B. A. Larsen, J. D. Bergeson, T. M. Barnes, G. Teeter, C. Engtrakul, J. L. Blackburn, n-Type Transparent Conducting Films of Small Molecule and Polymer Amine Doped Single-Walled Carbon Nanotubes, *ACS Nano* **5**, 3714 (2011).
- [30] Y.-M. Lin, D. B. Farmer, G. S. Tulevski, S. Xu, R. G. Gordon, P. Avouris, Chemical Doping of Graphene Nanoribbon Field-Effect Devices, Device Research Conference (2008).
- [31] D. B. Farmer, R. Golizadeh-Mojarad, V. Perebeinos, Y.-M. Lin, G. S. Tulevski, J. C. Tsang, P. Avouris, Chemical Doping and Electron–Hole Conduction Asymmetry in Graphene Devices, *Nano Lett.* **9**, 388 (2009).
- [32] A. C. Ferrari, J. C. Meyer, V. Scardaci, C. Casiraghi, M. Lazzeri, F. Mauri, S. Piscanec, D. Jiang, K. S. Novoselov, S. Roth, A. K. Geim, Raman Spectrum of Graphene and Graphene Layers, *Phys. Rev. Lett.* **97**, 187401 (2006).
- [33] S. Pisana, M. Lazzeri, C. Casiraghi, K. S. Novoselov, A. K. Geim, A. C. Ferrari, F. Mauri, Breakdown of the adiabatic Born–Oppenheimer approximation in graphene, *Nat. Mater.* **6**, 198 (2007).
- [34] J. Yan, Y. Zhang, P. Kim, A. Pinczuk, Electric Field Effect Tuning of Electron-Phonon Coupling in Graphene, *Phys. Rev. Lett.* **98**, 166802 (2007).
- [35] C. Casiraghi, S. Pisana, K. S. Novoselov, A. K. Geim, and A. C. Ferrari, Raman fingerprint of charged impurities in graphene, *Appl. Phys. Lett.* **91**, 233108 (2007).
- [36] C. Stampfer, F. Molitor, D. Graf, K. Ensslin, A. Jungen, C. Hierold, and L. Wirtz, Raman imaging of doping domains in graphene on SiO<sub>2</sub>, *Appl. Phys. Lett.* **91**, 241907 (2007).

- [37] A. Das, S. Pisana, B. Chakraborty, S. Piscanec, S. K. Saha, U. V. Waghmare, K. S. Novoselov, H. R. Krishnamurthy, A. K. Geim, A. C. Ferrari, A. K. Sood, Monitoring dopants by Raman scattering in an electrochemically top-gated graphene transistor, *Nat. Nanotechnol.* **3**, 210 (2008).
- [38] R.Wang, S. Wang, D. Zhang, Z. Li, Y. Fang, X. Qiu, Control of Carrier Type and Density in Exfoliated Graphene by Interface Engineering, *ACS Nano* **5**, 408 (2011).



## Chapter 5 Conclusion

### 5.1. Conclusions

To solve the global warming problem, conserving the energy and reducing the carbon emission are everyone's responsibility. On the other hand, to produce energy, we can not only combust the carbon materials but make more use of them. Incorporating carbon materials into PV system is a good way since the promising quantity and quality of solar energy. In this work, the polymer solar cells based on 0D to 2D carbon nanomaterials were demonstrated, by utilizing p-type graphene and SWNT thin films as the anodes, GO as the hole transport layer, n-type graphene as the cathode, and fullerene derivative PCBM as the electron acceptor in the photoactive layer. The photovoltaic device based on the solution processed SWNT/GO platform has exhibited a good power conversion efficiency which is comparable to the conventional device. And the new architecture of polymer solar cell based on all-graphene electrodes provides the world a potential route to develop a flexible, semitransparent photovoltaic device with the low-cost, roll-to-roll fabrication process. These two approaches have successfully demonstrated the promising possibility and capability of carbon nanomaterials applying on the PV technology, indicating that the ideal of using carbon materials to produce green energy seems going to realize in the near future.

## 5.2. Suggestions for future investigations

Although this thesis has successfully demonstrated the up-and-coming possibility and capability of carbon nanomaterials applied on the PV technology, there is still room for improvement needing more efforts to put in, especially the graphene electrode. Firstly, the flatness and the uniformity of graphene electrode are the key points affecting the device performance. How to fabricate graphene electrode without any carbonaceous residuals and wrinkles is the critical issue to solve. The followings are some strategies worth considering. Using a smooth Cu foil may directly result in a smoother graphene films, and the improvements of transferring technique, such as controlling the etching rate of Cu foils and using SAM-modified substrates, may eliminate the carbonaceous residuals and provide a better adsorbability of substrates during transferring graphene films. Secondly, the sheet resistance and workfunction of graphene electrodes also play important roles in determining the device characteristics. Finding a more effective dopant material which not only reduces the sheet resistance but also makes a large shift of workfunction of graphene is extremely essential. Because the lower series resistance and the enhanced energy barrier which prevents charge carriers from collected by the wrong electrode will lead to a better device performance. Lastly, some minor points such as reducing the residuals of tape after transfer, fabricating a more uniform, continuous GO hole transport layer and introducing an electron transport layer, are also



good ways to further improve the polymer photovoltaic device efficiency. By conquering these existing problems, graphene will become one of the most promising material to be applied to roll-to-roll manufactured, low-cost plastic organic electronics.

